Multiterawatt few-cycle pulse OPCPA for applications in high-field physics

Franz Tavella

SIGILL. UNIVERSITAT. LUDOVIC. MAXIM.

München 2007

Multiterawatt few-cycle pulse OPCPA for applications in high-field physics

Franz Tavella

Dissertation
an der Fakultät für Physik
der Ludwig–Maximilians–Universität
München

vorgelegt von
Franz Tavella
aus La Val, Dolomites

München, den Dezember 17, 2007

Erstgutachter: Ferenc Krausz
Zweitgutachter: Eberhard Riedle
Tag der mündlichen Prüfung: Februar 1, 2008

Contents

Zusammenfassung **viii**

1 Introduction **1**
- 1.1 High peak power laser amplifier development . . . 2
  - 1.1.1 Motivation for high peak power OPCPA development . . . 3
  - 1.1.2 Qualities of chirped-pulse optical parametric amplification . . . 3
- 1.2 Multiterawatt few-cycle pulses in high-field physics . . . 5
- 1.3 Thesis outline . . . 7

2 OPCPA modeling **9**
- 2.1 Phase matching . . . 9
- 2.2 Rules governing the non-collinear optical parametric process . . . 12
  - 2.2.1 Non-collinear optical parametric interaction . . . 13
  - 2.2.2 Choice of material . . . 15
  - 2.2.3 Signal-to-pump pulse duration ratio . . . 20
  - 2.2.4 Techniques for bandwidth engineering . . . 21
  - 2.2.5 Parametric interaction length, gain bandwidth . . . 21
  - 2.2.6 Angular detuning in single and multipass stages . . . 22
  - 2.2.7 Multiple beam pumping . . . 23
- 2.3 Simulation techniques for optical parametric amplification . . . 24
  - 2.3.1 Analytical description for the small gain regime . . . 24
  - 2.3.2 Numerical simulation . . . 25
  - 2.3.3 Nonlinear step . . . 26
  - 2.3.4 Linear step . . . 27
- 2.4 Signal and amplified optical parametric fluorescence . . . 27
  - 2.4.1 Simulation without saturation effects . . . 30
  - 2.4.2 Simulation with saturated amplifier . . . 32
- 2.5 Influence of the amplified spectrum on the presence of gain saturation . . . 35
- 2.6 Amplifier sensitivity to angle variation . . . 35

3 The amplifier system **39**
- 3.1 Ti:Sapphire oscillator front-end . . . 39
- 3.2 Ti:Sapphire amplifier front-end . . . 41

3.3 The pump 45
    3.3.1 Optical seeding 45
    3.3.2 Nd:YAG amplifier chain 48
3.4 Pulse stretcher-Compressor 52
    3.4.1 Simulation of a grism stretcher with reflection gratings 56
3.5 OPCPA with Ti:Sapphire oscillator front-end 60
    3.5.1 Energetics 61
    3.5.2 Amplified signal spatial beam profile 62
    3.5.3 Pulse compression 63
    3.5.4 Temporal pulse contrast 66
    3.5.5 Wavefront and focus measurements 69
3.6 OPCPA with Ti:Sapphire amplifier front-end 72
    3.6.1 Amplified signal energy and spectrum 72
    3.6.2 Pulse compression 73
    3.6.3 Temporal pulse contrast 74
    3.6.4 Summary of results 75

4 Test-ground for experiments in high-field physics 77
4.1 Electron acceleration in the "Bubble" regime 77

A Refractive index 83
A.1 Refractive index of isotropic materials and nonlinear optical crystal 83

List of publications 102

Danksagung 108

Abstract

A significant part of this work is devoted to the development of the brightest high-intensity few-cycle-pulse optical parametric chirped pulse amplifier (OPCPA) system. The completion of a 10 terawatt OPCPA is achieved, with 8.5-fs pulse duration at full-width at half maximum, which is within 6% of their Fourier transform-limited pulse duration. This was made possible by use of a combined grism and chirped mirror stretcher developed for dispersion compensation of a high throughput glass and chirped mirror compressor. The amplifier consists of a Ti:sapphire amplifier frontend and parametric amplifier stages based on type-I phase matching in BBO crystal. The OPCPA presented in this work is the first of its kind combining the few-cycle regime with relativistic intensities.

The seeding of the OPCPA is investigated first using a homebuilt broadband Ti:sapphire oscillator. For the first time, temporal contrast characterization of optical parametric amplified pulses has been performed. From these measurements we conclude that this approach is inappropriate because it does not provide the necessary seed energy to assure high temporal contrast at 10 TW. This finding has also been confirmed by 3D numerical simulations carried out to comprehend the underlying dynamics of optical parametric fluorescence (OPF) generation and amplification in a non-collinear OPCPA. The calculation allowed reduction of the amplified OPF in our system by specific pumping of the OPCPA stages.

In a second approach, designed to improve the temporal contrast, a Ti:sapphire amplifier with hollow-core fiber pulse-broadening is used as front-end of the OPCPA. The hollow-core fiber output is amplified in two OPCPA stages. The temporal contrast of these pulses is mantained during the amplification process. The output pulses show excellent temporal contrast of more than eight orders of magnitude from the pulse peak to the amplified OPF pedestal which makes this OPCPA ideal for high-field experiments.

The first successful application for this few-cycle pulse OPCPA has been the generation of mono-energetic electron bunches with several tens of MeV energy. Although electron acceleration has already been demonstrated using longer pulses from Ti:sapphire amplifiers, much improvement remains to be made in the regard of electron bunch parameters reproducibility. We have successfully performed electron acceleration experiments with the OPCPA presented in this thesis. "Quasi-monoenergetic" electron peaks were observed around few tens of MeV with substantially decreased amount of low-energetic electron compared to electron acceleration with longer laser pulses. Additionally, low radiation levels are detected during the acceleration process, which is an indication of direct access to the "bubble acceleration regime" and what makes this source saver and easy to use. The efficiency of electron acceleration is furthermore strongly increased due to the short pulse duration available from the OPCPA amplifier.

Zusammenfassung

Großteils handelt diese Arbeit über die Entwicklung des heutzutage leistungsstärksten, "few-cycle" optischer parametrischen Breitbandpulsverstärker. Im Mittelpunkt steht die Entwicklung eines 10 TW OPCPA mit 8.5-fs Pulsdauer bei Halbwertsbreite. Die Pulsdauer weicht nur 6% von der Fourier-limitierten Pulsdauer ab. Dies wurde möglich durch die Implementation eines kombinierten Grism- und dispersiven Spiegel-Pulsstrecker, dessen Dispersion komplemetär zu der eines kombinierten hochtransmittiven dispersiven Spiegel- und Glaskompressors ist. Der Verstärker besteht aus einem Ti:Saphir Vorverstärker und aus OPCPA Stufen basierend auf Typ-I Phasenanpassung in BBO Kristall. Das hier vorgestellte OPCPA System is das erste seiner Generation, der das "few-cycle" Regime mit dem relativistischen Regime vereint.

Zuerst wurde ein breitbandiges Ti:Saphir Oszillator für das "seeden" des OPCPA verwendet. Zum ersten Mal wird der zeitliche Kontrast eines OPCPAs charakterisiert. Aus diesen Messungen folgt, dass dieser Ansatz nicht genügend "seed"-Energie liefert, um einen hohen zeitlichen Kontrast für ein 10 TW OPCPA, zu gewährleisten. Dies wird auch durch numerische 3D Simulationen ersichtlich gemacht. Diese Simulationen sind ausgeführt worden, um die Dynamik der optischen parametrischen Fluoreszenzerzeugung (OPF) zu verstehen. Dies erlaubt uns Maßnahmen zu ergreifen um die OPF durch gezieltes Pumpen der OPCPA-Stufen zum Wesentlichen zu reduzieren.

In zweiter Instanz wird ein Ti:Sapphire Multipassverstärker zum "seeden" des OPCPA, verwendet dessen Pulse in einer Hohlfaser, spektral verbreitet werden. Der Hohlfaserausgang wird dann in einem zweitstufigen OPCPA verstärkt. Der zeitliche Kontrast wird während des Verstärkungsprozesses beibehalten. Die komprimierten Pulse weisen einen exzellenten zeitlichen Kontrast von mehr als acht Größenordnungen auf, ideal für den Einsatz in der Hochfeldphysik.

Den ersten erfolgreichen Einsatz fand das OPCPA in der Erzeugung von monoenergetischen Elektronenpulsen mit einigen zehn MeV an Elektronenenergie. Die Elektronenbeschleunigung ist bereits mit längeren Laserpulsedauern gezeigt worden, aber die Reproduzierbarkeit der Elektronenbündelparameter ist Verbesserungsdürftig. Uns ist Elektronenbeschleunigung mit dem hier beschriebenen Breitbandpulsverstärker gelungen, "quasimonoenergetische" Elektronenenergien mit einigen zehn MeV an Energie und stark reduziertem niederenergetischeren Elektronenhintergrund, als man bei Elektronenbeschleunigung mit längeren Laserpulsen beobachtet. Zusätzlich sind niedrige Strahlungswerte während des Beschleunigungsprozesses aufgezeichnet worden. Dies deutet auf direktem Zugang ins sogenannte "Bubble"-Regime, dies macht diese Quelle anwenderfreundlich. Dazu kommt noch eine bessere Effizienz des Beschleunigungsmechanismus wegen der Kürze der Laserpulse des, in dieser Dissertation präsentiertes Breitbandpulsverstärkers.

Chapter 1

Introduction

The field of laser physics has seen tremendous growth since the first practical realization of laser light in 1960 [1]. The first laser pulses were produced by gain switching and by Q-switching also known as giant pulse formation. In the following years lasing action was reported from a HeNe gas mixture [2], and from Nd^{3+}-doped solid state laser material [3]. Population inversion in semiconductor materials was also demonstrated in GaAs-junctions in 1962 [4]. Shorter pulses were later produced by modelocking techniques with dye lasers [5–7]. These lasers were replaced by Ti:sapphire based Kerr-lens "magic" mode-locked lasers after their discovery in the early 1990s [8]. The Ti:sapphire laser is more reliable and simple to operate allowing its use in a wider part of the scientific community. Shortly before this discovery of Kerr-lens mode-locking, in 1985, a new technique for laser pulse amplification, chirped pulse amplification (CPA), was developed to overcome stagnating progress reaching higher peak laser intensities, which had persisted since the early 1970s [9–11]. Discovery of Kerr-lens-modelocking gave a significant boost to CPA lasers by making a stable femtosecond oscillator development possible and thus simplifying the CPA laser design. The concept of CPA allowed to amplify ultrashort laser pulses avoiding self-action effects and thus damage to optical materials. The gain medium most used in CPA is a Ti:sapphire crystal which allows broadband amplification due to the vibrational lines in Ti^{3+} embedded in the sapphire continuum [12–15]. Using these techniques in combination with Nd:glass gain medium, which has lower constraints in the manufacturing size, petawatt peak powers with intensities in the focal spot exceeding $10^{21}\mathrm{W/cm^2}$ have been reached [16].

Another technique used for ultrashort pulse amplification is optical parametric amplification (OPA) [17, 18]. Parametric amplification was predicted in the early 1960s and the concept was soon applied in optical parametric oscillators (OPOs) [19–21]. Optical parametric amplification proved to be a convenient way to extend the tunability of femtosecond lasers [22–26]. During 1992, Dubietis *et al.* [27] realized the first amplifier, which merged the OPA and CPA-techniques (OPCPA). Years before in 1986, Piskarskas *et al.* [28] investigated phase phenomena in parametric amplifiers in a similar system. A substantial contribution to the success of parametric amplification was made by the discovery of new nonlinear optical crystals with nonlinear optical properties not seen before (i.e. borates like

BBO, LBO, BiBO,...) [29]. In 1997, Ross *et al.* [30] proposed the use of OPCPA-techniques to amplify laser pulses to Petawatt peak power levels with a ”table-top” amplifier. Since then, remarkable progress have been made in OPCPA-development, and OPCPA will be used in many future applications [31–35]. A good summary of progress in OPA/OPCPA development is given in references [36–38].

1.1 High peak power laser amplifier development

The highest peak power laser amplifier systems are based almost entirely on CPA (with Nd:glass and/or Ti:sapphire gain medium), which is by now the most well-known and most reliable amplification technique. Unfortunately, the limits of scalability are reached due to self-action issues and due to the available size of compressor gratings. First petawatt pulses were generated in 1996 at Lawrence Livermoore National Labs (LLNL, Nova 1.25-PW, 0.5-ps) [16, 39]. This Petawatt amplifier was dismantled later to make way for the OMEGA-laser. Laser research facilities currently equipped with ”Petawatt-light” are the Rutherford Appleton Labs (RAL, Vulcan 1-PW, 1-ps) which showed first Petawatt peak powers in 2002 [40] and Gekko VII with OPCPA preamplifier (Japan, 0.9-PW, 470-fs) [41]. There are many other facilities working to reach the Petawatt-goal. Meanwhile Petawatt scale laser amplifier systems based on Ti:sapphire gain medium are also becoming commercially available. It should be mentioned that several research facilities tend to incorporate OPCPA development to reach higher intensities. This is the case for the Vulcan-PW front-end (323-TW, 500-fs). Current plans at Rutherford Appleton Laboratories include an upgrade of the PW-amplifier to 10-PW using OPCPA-techniques. Most OPCPA systems are used in collinear geometry near degeneracy, not taking advantage of different geometries of interaction to extend the bandwidth of amplification. OPCPA development based on collinear geometry was done by Yang *et al.* (3.67-TW, 155-fs) [42], Ross *et al.* (1-TW, 300-fs) [43] and Lozkharev *et al.* (200-TW, 100-fs) [44] all using DKDP-based amplifier stages. Another area of OPCPA development has recently drawn the attention of the scientific community. This development on non-collinear OPCPA is meant to reach highest peak intensities with the shortest possible pulse duration, taking full advantage of the capability for broadband amplification in the non-collinear optical parametric interaction geometry. Attainable pulse durations are in the sub-10-fs range. These pulses comprise a spectrum exceeding 100 THz bandwidth. The first demonstration was achieved by Ishii *et al.* at TU-Vienna [33] with amplification of pulses from a broadband Ti:sapphire oscillator to 5 mJ of energy and compression to 10-fs pulse duration reaching 0.5-TW peak power, followed by Witte *et al.* [34] with 15 mJ pulses and 7.6-fs pulse duration (2-TW). The highest peak power was accomplished at the Max-Planck Institut für Quantenoptik with 80-mJ of energy compressed to 8.5-fs attaining for the first time 10-TW peak power and this is subject of this thesis [35].

1.1.1 Motivation for high peak power OPCPA development

The *sui generis* optical parametric chirped pulse amplifier presented in this thesis is a 10 terawatt amplifier system. It is the, to-date, most powerful and most reliable few-cycle pulse amplifier available for experiments in high-field physics. The signal pulses are amplified to nearly 100-mJ of energy. The energy is comprised in a 8.5-fs pulse which differs by 0.5-fs from the transform-limited pulse duration. The wavefront distortions of the beam are less than $\lambda/10$ and the best measured focus is 3 μm at FWHM. The resulting focal spot intensity with 10-TW peak power is $5.6 \cdot 10^{19}$ W/cm^2. The short pulses exhibit high (at least 10^{-8} in a ± 40 ps temporal window around the main pulse and $<10^{-8}$ outside this range) temporal contrast to perform experiments based on solid density plasma formation, where a low ps-pedestal is a necessary condition to avoid pre-plasma generation on target. These unique pulse properties makes this light source extremely interesting for a number of application in high-field physics. An overview of first experiments is given in Chapter 4.

1.1.2 Qualities of chirped-pulse optical parametric amplification

The properties of optical parametric chirped pulse amplification are listed below. The advantageous aspects of the OPCPA technique clearly overwhelm the disadvantages. Nonetheless, this listing should show that this technique has many degrees of freedom and that not all of them are beneficial.

Advantages

- **Gain bandwidth** One of the most remarkable properties of parametric amplification is the possibility of large bandwidth amplification. The supported bandwidth can exceed 100 THz depending on geometry of interaction, crystal type, crystal thickness and additionally most important parameter, the wavevector phase-matching achieved mostly through noncollinear optical parametric interaction.

- **Single-pass gain** The single pass gain achievable in an OPCPA is extremely high. It can reach up to six orders of magnitude, this can result in decreased signal contrast due to generation of background emission which is further amplified in subsequent OPCPA stages.

- **Thermal load** The thermal load in an OPCPA is negligible till highest pulse repetition rates. The energy is not stored in the amplifier material as it is in a solid state gain medium, but the energy conversion from pump to idler and to signal is an instantaneous parametric effect.

- **Efficiency** High efficiencies can be reached with OPCPA. The highest ever reached was around 20-25% conversion efficiency from pump to signal, and slightly smaller for the idler in a saturated stage.

- **Scalability to high energies** OPCPA can be scaled to reach even higher peak powers than with conventional CPA-amplifiers by reducing pulse duration of the amplified signal pulses. The signal pulse duration can be much shorter due to the large amplification bandwidth. A serious limitation is nonetheless the available pump amplifier at a given pump pulse duration. A second limitation is the size of the compressor in our setup.

- **Self- and cross-action effects** The accumulation of higher order nonlinear effects in OPCPA is much smaller than in conventional amplifiers. Nevertheless, effects like cross-phase-modulation start to play a role at high pump intensities and/or at large signal energies on the order of the pump energy (i.e. near saturation).

- **Versatility to achieve phase matching**

  There are several degrees of freedom that can be exploited to achieve broadband phase matching. Among them, and most important, the non-collinear angle between pump and signal, but also the pump beam bandwidth (chirped pump), multiple beam pumping with different non-collinear angles, or an angularly chirped signal or pump can be used. The choice is often a matter of convenience.

- **Idler wave**

  The idler wave can also be useful in some case. For example generation of a seed beam in a spectral region difficult to reach with conventional techniques, use of the idler wave to stabilize the carrier envelope offset [45]. Another possible application would be measurement of the carrier envelope offset using the idler wave [46].

Challenges

- **Pump-to-signal synchronization** The signal and pump pulse durations are matched in time in order to reach highest conversion efficiencies. Therefor, these pulses need to be precisely synchronized in time either by electronic or optical synchronization.

- **Stretching and compression** Few-cycle pulses are already difficult to stretch and compress in a NOPA based amplifier. It gets even more complicated if the stretching ratio exceeds 4 orders of magnitude to the ps-region to match the duration of a long, energetic pump pulse. A large bandwidth can be stretched using less dispersion but this dispersion needs to be carefully compensated. Adaptive dispersion compensation is usually necessary for compression.

- **Strict phase matching conditions**

  Alignment of a parametric amplifier involves several issues including geometry of interaction, pointing stability, pump energy fluctuations, beam collimation, etc. These parameters must all be considered in order to obtain reliable operation.

Disadvantages

- **Background emission, temporal contrast** Background emission of an OPCPA has an entirely different mechanism of generation compared to amplified spontaneous emission (ASE) in a solid-state laser amplifier. The background emission in an OPA is amplified optical parametric fluorescence (AOPF). It is generated during the OPA-process due to high pump intensity. The reason is spontaneous decay of a pump photon into an idler and a signal photon, which is further parametrically amplified.

- **Pump beam requirements** The requirements for the pump in an OPCPA are demanding. The pump should deliver highest than possible energy. The pump pulse duration regime depends on the application and can be several hundred fs to ns. The pump can be quasi-monochromatic, like the fundamental or the second harmonic of a Nd:YAG amplifier, or broadband like the second harmonic of a Ti:sapphire amplifier. In this case, where the pump is broadband itself, the pump can be used to enhance broadband amplification of the signal. Additionally, the quality of the amplified signal spatial beam profile is directly related to the optical properties of the pump beam. The even small imperfections in the pump beam profile will appear and be enhanced in the signal beam profile due to the high parametric gain.

- **Energy stability** Near saturation, OPCPA output can reach a stability close to the pump pulse energy stability. The energy fluctuations in the unsaturated OPCPA stage depend on the pump energy fluctuations and on the gain factor in the amplifier stages.

- **Spatial chirp**

  The non-collinear parametric amplification process is a directional process. If a poor choice of interaction geometry is made, spatial chirp and spatial dispersion of the amplified beam can occur.

1.2 Multiterawatt few-cycle pulses in high-field physics

The unique properties of the optical parametric chirped pulse amplifier outlined in the previous section are of great interest for a number of high-field experiments.

The pulse duration is much shorter than the time where typical plasma instabilities can rise, this is one of the strongest advantages using ultrashort laser pulses in laser plasma physics. A pulse duration of less than 100-fs is already short enough to avoid motion of the ions which would lead to such hydrodynamic and parametric instabilities as Stimulated Brillouin Scattering (SBS) [47]. Additionally, the laser pulse is insensitive to plasma expansion which occurs on a timescale longer than one hundred femtoseconds.

Few-cycle pulses can also be advantageous for several particle acceleration mechanisms. In some cases, more energy can be coupled to the accelerated particle. An example is "bubble"-electron acceleration from a gas-jet [48–51]. For sub-10-fs pulse duration the bubble formation is expected to occur directly without relativistic self-channeling. Moreover, the pulse energy used to form the bubble, which is effectively used for acceleration, strongly depends on driving pulse duration. Another component of the laser-electron acceleration community uses a gas-filled capillary for electron acceleration and might find shorter pulses of interest for the same reason. The capillary technique was first used to reach the GeV-level in laser-driven-electron acceleration [52].

Another important application is proton acceleration with high intensity laser amplifiers ($> 10^{21}\mathrm{W/cm^2}$) [53], which can lead to effective use of proton beams for medical applications [54]. A challenge still open, before application of these sources in proton therapy is the proton yield [55]. Similar challenges are faced by the laser-driven fusion research community. High intensity laser amplifiers have long been desired for fusion research. Fast ignition [56, 57] is a promising way to achieve fusion but requires Petawatt-scale amplifiers with repetition rates higher than those attainable from existing Nd:glass or Ti:sapphire based amplifier systems. The OPCPA amplifier presented here, makes a step further in this direction, combining high repetition rate with high peak power.

Few-cycle pulses not only offer high peak powers from compact systems but also enabled the emergence of entirely new technologies such as the generation, measurement and spectroscopic applications of isolated attosecond pulses and for steering the atomic-scale motion of electrons with controlled light fields [58–63]. Single attosecond pulses are ideal probes to resolve ultrafast dynamical processes in physics. The optical parametric amplifier concept is well suited to scale pump- and probe-beams to higher brightness and higher repetition rates.

One possible way to generate an intense single attosecond pulse is through harmonic generation from solid density plasmas with few-cycle pulses [64]. Another possibility is high harmonic generation from a noble gas target. More energetic few-cycle laser pulses can be used to extend the harmonic yield. Few-cycle pulses with longer central wavelength (amplified through OPA technique) can be used to extend the cut-off region to higher harmonic energies. For example the spectral region between ∼2.3-4.4 nm (water window) is important for biological and material imaging applications to reduce the absorbtion of harmonic light through water, whereas carbon atoms absorbs this light (K-edge). High harmonic generation with few-cycle pulses has been reported for harmonic orders far beyond the water window towards the keV range [65–68].

1.3 Thesis outline

A short survey of the thesis structure is given below.

- Simulations regarding the OPCPA concept are presented in *Chapter 2*. The choice of nonlinear crystal and geometry of interaction are discussed and supported by simulation. Special attention is given to simulation of amplified optical parametric fluorescence (AOPF) . This effect is vital to OPCPA development as the contrast dynamics can be simulated and improved. Several methods to decrease the AOPF in the amplifier are considered. Typical behavior of a parametric amplifier in the saturation regime and in the linear amplification regime are also discussed.

- The amplifier system is described in detail in *Chapter 3*. The individual parts of the amplifier are described separately. The Ti:sapphire oscillator and amplifier first (front-end), followed by pump amplifier, stretcher, compressor and finally the OPCPA amplifier. The amplifier parameters considered in the OPCPA section are energetics, beam profiles, compressed pulse duration, temporal contrast, wavefront and focusability of the compressed beam. Two separate section are devoted to seeding with a Ti:sapphire oscillator and to seeding with a Ti:sapphire amplifier.

- The subject of *Chapter 4*, is a description of the first experiment with this few-cycle pulse source: acceleration of mono-energetic electrons in the "bubble-regime".

- The *Appendix* contains calculation of the refractive index for divers isotropic materials and nonlinear optical crystals.

Chapter 2

OPCPA modeling

This section is dedicated to the theoretical description of the parametric amplification process. The standard analytical model of the OPA-process is shortly described. It is useful to understand basic relationship between OPA-parameters, as for example the relation among pump intensity and parametric gain. In addition, a thorough numerical description of the OPCPA process is given. It includes for the first time the amplification of the optical parametric fluorescence. This is a necessary step towards the development of a multiterawatt amplifier system for use in temporal-contrast-sensitive high-field experiments. Further aspects of the non-collinear optical parametric amplification process are investigated in detail.

2.1 Phase matching

Parametric amplification phenomena are considered a special case of difference frequency generation, which is one of the most important second order nonlinear effect. The only difference results in different initial input conditions [69, 70]. The material response to an optical excitation is instantaneous, without delay. A pump photon with angular frequency ω_p propagating in a nonlinear crystal, spontaneously or by stimulated parametric emission breaks down into two lower energy photons of frequencies ω_s and ω_i. The suffixes p,s and i refer pump, signal and idler waves. The specific pair of frequencies (signal and idler) that will result from the parametric process are determined by the energy conservation condition

$$\omega_s = \omega_p - \omega_i. \tag{2.1}$$

The energy condition is intrinsically fulfilled. Additionally an approximate momentum relationship (momentum conservation condition)

$$\mathbf{\Delta k} = \mathbf{k}_p - \mathbf{k}_s - \mathbf{k}_i \quad \text{with} \quad |\mathbf{k}_j| = n_j(\omega)\frac{\omega_j}{c_0} = n_j(\omega)\frac{2\pi}{\lambda_j}, \tag{2.2}$$

must be satisfied for the parametric amplification process. $\mathbf{k}_j$ are the wavevectors corresponding to parametric waves with frequency ω_j. This condition is not coercive but can be satisfied within the limits of phase matching. The best conversion efficiency of pump to signal and idler waves is achieved if the phase relationship between the waves has constant value and amounts to

$$\Theta = \phi_p - \phi_i - \phi_s = -\frac{\pi}{2}. \tag{2.3}$$

This always applies at the beginning of parametric amplification with zero initial idler wave. The idler phase automatically takes a value of

$$\phi_i(0) = \phi_p(0) - \phi_s(0) + \frac{\pi}{2}. \tag{2.4}$$

The spectral phase accumulates with increasing interaction length z and according to the wave-vector mismatch between the parametric waves Δk during propagation in the nonlinear amplifier medium. A change of phase among the parametric waves causes the energy flow to reverse back to the pump wave before the pump energy is completely depleted, which would be the case for $\Delta k = 0$. For non-vanishing wave vector mismatch Δk, the energy flow is reversed from signal and idler wave to the pump wave, after a characteristic propagation distance $z = l_c$ called *coherence length.*

$$l_c = \frac{\pi}{\Delta k}, \tag{2.5}$$

The phase terms for pump, signal and idler $\phi_{p,s,i}$ in Eq. 2.3 are marginal in the linear amplification regime but reach larger values if the pump wave reaches depletion. An expression for these phase terms can be obtained by solving the imaginary part of the coupled wave equations and using the Manley-Rowe-relation [71].

$$\frac{\mathrm{d}\phi_s}{\mathrm{d}z} = -\frac{\Delta k}{2}[1 - \frac{\gamma_s^2}{f + \gamma_s^2}], \tag{2.6}$$

$$\frac{\mathrm{d}\phi_i}{\mathrm{d}z} = -\frac{\Delta k}{2}, \tag{2.7}$$

$$\frac{\mathrm{d}\phi_p}{\mathrm{d}z} = -\frac{\Delta k}{2}\frac{f}{1 - f} \tag{2.8}$$

The integration of Eqs. 2.6-2.8 leads to

$$\phi_s = \phi_s(0) - \frac{\Delta k z}{2} + \frac{\Delta k \gamma_s^2}{2}\int \frac{\mathrm{d}z}{f + \gamma_s^2}, \tag{2.9}$$

$$\phi_i = \phi_p(0) - \phi_s(0) + \frac{\pi}{2} - \frac{\Delta k z}{2}, \tag{2.10}$$

$$\phi_p = \phi_p(0) - \frac{\Delta k}{2}\int \frac{f\mathrm{d}z}{1 - f}. \tag{2.11}$$

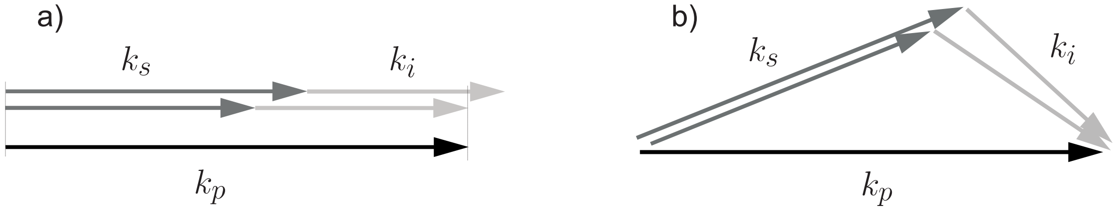

Figure 2.1: Geometry of beam interaction; (a) collinear; (b) non-collinear.

with

$$\gamma_s^2 = \frac{\omega_p}{\omega_s}\frac{I_s(0)}{I_p(0)} \quad \text{and} \quad f = 1 - \frac{I_p}{I_p(0)}. \tag{2.12}$$

γ_s^2 is the input photon intensity ratio for the signal wave and f is the fractional depletion of the pump wave.

Some interesting aspects about optical parametric amplification can be gained from these phase expression. A change of phase takes only place if $\Delta k \neq 0$. The accumulated phase is larger for pump depletion ($0 < f \leq 1$). Furthermore, a pump beam with temporal phase variation as for example a chirped pump beam can be used for amplification because the signal phase does not depend on the pump phase in Eq. 2.9. Backconversion of the signal and idler waves into the pump wave occurs if the phase Θ in Eq. 2.3, which is accumulated over a certain process period exceeds zero. Hence, the objective is to minimize Δk over a large frequency range. This is called phase matching and can be achieved in different ways.

- *Temperature-controlled phase-matching* is used to achieve phase matching along a principal axis of the nonlinear crystal by temperature tuning (non-critical phase matching).

- *Quasi-phase-matching* is obtained for parametric waves propagating in a medium with alternating sign of nonlinear optical coefficient in a periodically poled crystal. Wavelength tuning is inherent to the poling design. Commonly used nonlinear crystals for quasi-phase-matching are PPLN (periodically poled Lithium Niobate) and PPKTP (periodically poled potassium triphosphate).

- *Birefringent phase-matching*, also known as angular phase matching, is achieved in birefringent materials which exhibit a different refractive index at different polarizations. Different combination of polarizations for pump, signal and idler wave can be used. Type-I phase-matching is typically used to obtain the largest possible phase-matching bandwidth as will be described in the next section. Two types of interaction geometries are common for wave propagation, collinear and non-collinear (Fig. 2.1). The phase-matching condition for the collinear geometry is not fulfilled due to the dispersive properties of the nonlinear amplifier medium resulting in a mismatch of the group velocities [72]. Better phase-matching is achieved in non-collinear interaction geometry, where the wave-vector mismatch Δk is minimized over a large spectral range using the non-collinear angle between signal and pump wave as additional degree of freedom to achieve group velocity matching. This geometry is used for the amplifier described in this thesis.

2.2 Rules governing the non-collinear optical parametric process

The relative location of the wave vectors in the nonlinear optical crystal used for amplification in the parametric amplifier, which is described in this thesis, is non-collinear (vector phase matching). The phase matching is type-I, a phase matching scheme to achieve the largest possible phase-matched bandwidth in optical parametric amplification. The polarization for the pump wave is orthogonal to the signal and idler polarization in order to achieve the phase matching condition. In case of an uniaxial crystal it can be either ooe-type for negative crystals (Type I^-) or eeo-type for positive crystals (Type VIII^+). The signal and idler waves propagate in the ordinary direction in a negative uniaxial crystal (polarization is normal to the principal plane) and the pump in extraordinary direction (polarization is parallel to the principal plane). The principal plane is referred to as the plane containing the optical axis and the wavevector of the beam. In the case of biaxial crystals the use of the ordinary and extraordinary wave terminology makes only sense if referring to a plane (XY, XZ or YZ-plane), as principal plane. Usually the waves are named slow(s)-waves or fast(f)-waves. The type-I phase matching in biaxial crystal is of s-ff-type and depend on the crystal type.

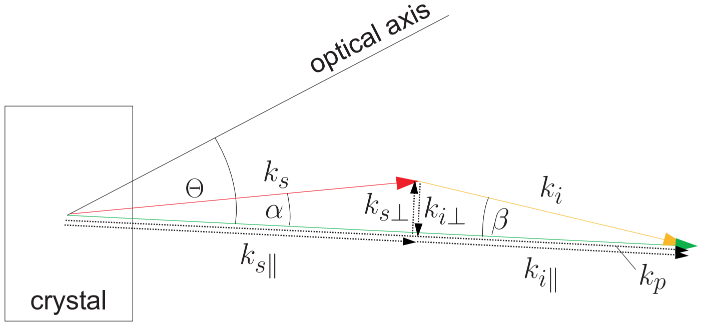

Figure 2.2: Pump, signal and idler vectors in the crystal plane in non-collinear geometry; α...non-collinear angle; Θ...phase-matching angle

The seed direction in the uniaxial crystal can be chosen in two directions on the principal plane. Tangential phase matching (TPM, see Fig. 2.2) for example, is used for the signal and pump wave direction to avoid generation of the second harmonic of the signal wave in β-BBO [73, 74]. The signal wave propagates between the optical axis and the pump beam vector with the angle $\Theta - \alpha$ relative to the optical axis. The signal wave in PVWC-scheme (Poyinting-vector walk-off compensation scheme) propagates in opposite direction with an angle of $\Theta + \alpha$ relative to the optical axis. This angle is located in the range of phase-matching for second harmonic generation of the signal wave in BBO crystal.

2.2.1 Non-collinear optical parametric interaction

The interaction geometry is depicted in figure 2.2. The wavevector diagram for pump, signal and idler waves is mismatched by a factor Δk. Δk can be expanded in a Taylor-series, in order to analyze the implication of wavevector matching for broadband pulses in non-collinear geometry,

$$\Delta k = \Delta k_0 + \frac{\partial \Delta k}{\partial \omega}\Delta\omega + \frac{1}{2}\frac{\partial^2 \Delta k}{\partial \omega^2}(\Delta\omega)^2 + \dots \quad \text{with} \quad \Delta\omega = \omega - \omega_0. \tag{2.13}$$

ω is the angular frequency of the signal wave and ω_0 its central angular frequency. The phase matching condition is fulfilled if Δk_0 and the derivatives equals zero. The same condition can be applied to the parallel and normal component of Δk (see Fig. 2.2).

$$\Delta k_{\|} = k_{\mathrm{p}} - k_{\mathrm{s}\|} - k_{\mathrm{i}_{\|}} = k_{\mathrm{p}} - k_{\mathrm{s}}\cos\alpha - k_{\mathrm{i}}\cos\beta, \tag{2.14}$$

$$\Delta k_{\perp} = k_{\mathrm{s}\perp} - k_{\mathrm{i}_{\perp}} = k_{\mathrm{s}}\sin\alpha - k_{\mathrm{i}}\sin\beta \tag{2.15}$$

with

$$k_i(\omega_i, \Theta_i, \Phi_i) = n_i(\omega_i, \Theta_i, \Phi_i)\frac{\omega_i}{c_0} \qquad i = \mathrm{p,\ s,\ i.} \tag{2.16}$$

Θ_i is the polar angle and Φ_i is the azimuthal angle in a biaxial crystal. Exact phase matching for Δk_0 at the signal center frequency and for the first derivative $\frac{\partial \Delta k}{\partial \omega_s}$ should be fulfilled at the same time, whereupon an additional control parameter is required. The control parameter used in type-I phase matching is the angle α between pump and signal, dubbed non-collinear angle. The wavelength-dependent angle $\beta = \beta(\omega)$ is the angle between pump and idler wavevector.

The pump is assumed to be quasi-monochromatic and collimated in the following derivations of Eq. 2.14 and 2.15, thus $\frac{\partial \Delta k_p}{\partial \omega} = \frac{\partial \alpha}{\partial \omega} = 0$.

$$\Delta k_{\|}^{(1)} = -\frac{\partial k_s}{\partial \omega}\cos\alpha + k_i \sin\beta\frac{\partial \beta}{\partial \omega} - \frac{\partial k_i}{\partial \omega}\cos\beta, \tag{2.17}$$

$$\Delta k_{\perp}^{(1)} = \frac{\partial k_s}{\partial \omega}\sin\alpha - k_i \cos\beta\frac{\partial \beta}{\partial \omega} - \frac{\partial k_i}{\partial \omega}\sin\beta. \tag{2.18}$$

To simplify these expressions, Eq. 2.17 is multiplied by $\cos\beta$, Eq. 2.18 by $\sin\beta$ and addition of these equations leads to

$$\frac{\partial k_s}{\partial \omega}(\cos\alpha\cos\beta - \sin\alpha\sin\beta) + \frac{\partial k_i}{\partial \omega}(\cos^2\beta + \sin^2\beta) = 0, \tag{2.19}$$

under assumption of phase-matching conditions ($\Delta k_{\|}^{(1)} = \Delta k_{\perp}^{(1)} = 0$).

Further simplification is achieved by applying the Sine rule

$$\frac{\partial k_s}{\partial \omega}\cos\Omega + \frac{\partial k_i}{\partial \omega} = 0 \quad \text{with} \quad \Omega = \alpha + \beta. \tag{2.20}$$

The group velocity is defined as $v_g = (\frac{\partial k}{\partial \omega})^{-1}$. Therefore, Eq. 2.20 can be rewritten as

$$v_{gs} = v_{gi}\cos\Omega \quad \text{with} \quad v_{gi} = -\frac{\partial k_i}{\partial \omega}. \tag{2.21}$$

This is the condition for group velocity matching, a necessary condition to eliminate the first order derivative of the wavevector mismatch in Eq. 2.13.

In addition, we can find an expression for the derivative $\frac{\partial \beta}{\partial \omega}|_{\omega_0}$ for the center frequency ω_0, assuming $\Delta k_{\parallel}^{(1)}|_{\omega_0}$ and $\Delta k_{\perp}^{(1)}|_{\omega_0}$ to be zero in Eqs. 2.17 and 2.18. After some algebraic manipulation, inserting Eq. 2.17 in Eq. 2.18, an expression for $\frac{\partial \beta}{\partial \omega}|_{\omega_0}$ is found,

$$\frac{\partial \beta}{\partial \omega}|_{\omega_0} = \frac{\tan(\Omega(\omega_0))}{v_{gi}(\omega_0)k_i(\omega_0)}. \tag{2.22}$$

The residual phase mismatch is governed by higher order terms. For more detailed analysis, the same procedure used for the first order derivative is now applied to the second order derivative.

$$\Delta k_{\parallel}^{(2)} = -\frac{\partial^2 k_s}{\partial \omega^2}\cos\alpha - \frac{\partial^2 k_i}{\partial \omega^2}\cos\beta + 2\frac{\partial k_i}{\partial \omega}\frac{\partial \beta}{\partial \omega}\sin\beta + k_i(\frac{\partial \beta}{\partial \omega})^2\cos\beta + k_i\frac{\partial^2 \beta}{\partial \omega^2}\sin\beta \tag{2.23}$$

$$\Delta k_{\perp}^{(2)} = \frac{\partial^2 k_s}{\partial \omega^2}\sin\alpha - \frac{\partial^2 k_i}{\partial \omega^2}\sin\beta - 2\frac{\partial k_i}{\partial \omega}\frac{\partial \beta}{\partial \omega}\cos\beta + k_i(\frac{\partial \beta}{\partial \omega})^2\sin\beta - k_i\frac{\partial^2 \beta}{\partial \omega^2}\cos\beta \tag{2.24}$$

From multiplication of Eq. 2.23 by $\sin\beta$, Eq. 2.24 by $\cos\beta$ and addition of the equations, follows

$$\frac{\partial^2 k_s}{\partial \omega^2}(\cos\alpha\cos\beta - \sin\alpha\sin\beta) + \frac{\partial^2 k_i}{\partial \omega^2}(\cos^2\beta + \sin^2\beta) - k_i(\frac{\partial \beta}{\partial \omega})^2(\cos^2\beta + \sin^2\beta) = 0. \tag{2.25}$$

Further simplification using Eq. 2.22 at ω_0 leads to

$$\frac{\partial^2 k_s}{\partial \omega^2}|_{\omega_0}\cos\Omega(\omega_0) + \frac{\partial^2 k_i}{\partial \omega^2}|_{\omega_0} - \frac{\tan^2(\Omega(\omega_0))}{k_i(\omega_0)v_{gi}^2(\omega_0)} = 0 \tag{2.26}$$

A broad plateau with marginal wavevector mismatch is expected around the central wavelength ω_0, for which Eq.2.26 is fulfilled. An additional degree of freedom is required to compensate the second order derivative in Eq. 2.13. For example a wavelength-dependent non-collinear angle $\alpha(\omega)$ (angular dispersion) can be used or either a broadband chirped pump beam.

2.2.2 Choice of material

A nonlinear crystal suitable for an OPCPA has to fulfill several requirements. Large effective nonlinear optical coefficient is one of the most important property of the crystal. The signal wave should support broadband phase-matching over a large bandwidth, with small non-collinear angle to minimize spatial walk-off effects caused by the different propagation direction of pump and signal waves. The crystal should have a large transparency range, including the spectral region for the idler wave to avoid idler absorbtion, which would in turn result in reduced parametric amplification. Further properties are high damage threshold, low hygroscopicity and available size of the crystal. These properties restricts our choice to mainly a few crystals belonging to the borate crystal group (BBO, BiBO and LBO). The optical and material properties are listed in table 2.1. These properties are taken from crystal manufacturers and from references [75]-[79].

The first step to evaluate the maximum phase-matching bandwidth for a given monochromatic pump wave is to determine the right phase-matching and non-collinear angle. In our case the pump wavelength is the second harmonic of Nd:YAG at 532-nm. The seed pulse spectrum from the Ti:sapphire oscillator span a range from 600 to 1030-nm.

For the calculation of the exact refractive index values we refer to Boeuf *et al.* [80] which gives a complete routine to solve Eqs. 2.14 and 2.15 for uniaxial and for biaxial crystals. The wave-vector in the case of biaxial crystals depends, not only on the polar angle Θ_i but also from the azimuthal angle Φ_i.

The phase matching angle and the non-collinear angle can be estimated, by first calculating the variation of the non-collinear angle α with a given phase-matching angle Θ and a fixed signal wavelength for exact phase-matching ($\Delta k_{\|} = 0$ and $\Delta k_{\perp} = 0$). These calculation can be performed for several signal wavelengths in increasing steps. The calculation with signal wavelength as variable parameter is shown in Fig. 2.3.a (color graphs, solid line) for BBO, LBO and BIBO crystals and is referred to as curve(s) A in the caption. The combination of the graphs show an intersection point which indicates a small wave-vector mismatch for different signal wavelength used in this calculations. This result is verified by the calculation of the optimum non-collinear angle variation, by requirement of zero phase mismatch to first order (Eq. 2.21, see curve B in 2.3(a), dotted line) [71]. The point of maximum achievable phase matching bandwidth is indicated by the intersection between the curve A and B. The values obtained for non-collinear and phase-matching angle are used to calculate the wave-vector mismatch for the frequency range of interest (Fig. 2.3(b)). This is solved at given non-collinear and phase matching angle value by Eqs. 2.14 and 2.15 for variable signal wavelength. The phase matching bandwidth can be roughly estimated by means of the phase condition in Eq. 2.5 for a given crystal thickness.

Broadband phase-matching can be achieved in different crystal-planes. Moreover, different wavelength regions can be covered on one crystal plane, in one and the same crystal. LBO for example has excellent phase-matching conditions from 700-1050 nm with phase-matching-angle Θ_{pump} ~14° in XY-plane and with Θ_{pump} ~32° in XZ-plane. In these planes, phase-matching can be achieved with the non-collinear angle α=1.5° and with non-collinear angle α=1.3°, respectively. Phase matching in the XZ-plane is shown in Fig. 2.3(b, middle section). Fig. 2.3 shows parameters for non-collinear geometry, generally used for type-I phase matching in BBO, LBO and BiBO crystals.

The largest phase matching bandwidth is expected for LBO reaching far in the infrared region. BBO has also large phase matching bandwidth [82], which favors more the shorter wavelength region. BiBO follows with the narrowest phase matching bandwidth in the infrared region but it has similar phase-matching properties in the shorter wavelength range, as BBO. The expectance for wide transparency range, low hygroscopic susceptibility, crystal size and high damage threshold is fulfilled by all three crystals. Nevertheless, BiBO and BBO have the largest nonlinear coefficients. From these two crystals, BBO has a smaller non-collinear angle and for this reason the first choice for parametric amplification crystal is BBO. However, the high nonlinear optical coefficient of the BiBO crystal is an interesting parameter to exploit. Therefore, it was tested in an OPCPA stage as a possible candidate for broadband optical parametric amplification for first time. The results are presented in the next section.

Materials	**BBO**	**LBO**	**BIBO**
NLO coefficient d_{eff} $[\frac{\text{pm}}{\text{V}}]$	2.2	0.85	3.2
damage threshold* $[\frac{\text{GW}}{\text{cm}^2}]$	> 7	> 4.5	> 4.5
hygroscopic susceptibility	low	very low	none
transparency range [nm]	190-3500	160-3200	286-2500
point group and crystal plane	uniax.-$^{(3m)}$	biax.-$^{(mm2)}$ XZ-plane	biax.+$^{(mm2)}$ YZ-plane
phase matching angle [°]	23.83	32.09	15.6
non-collinear angle [°]	2.26	1.5	3.6

Table 2.1: Optical and material properties of borate group crystals BBO, LBO and BiBO (see also Ref. [81]); *the stated values can differ substantially from the various manufacturers. The damage threshold is given at 75 ps, 532 nm for BBO, at 100 ps, 532 nm for LBO and the damage threshold for BiBO is assumed to be similar to LBO as stated in Ref. [79]. The phase matching and non-collinear angles are given for typical Type-I application conditions

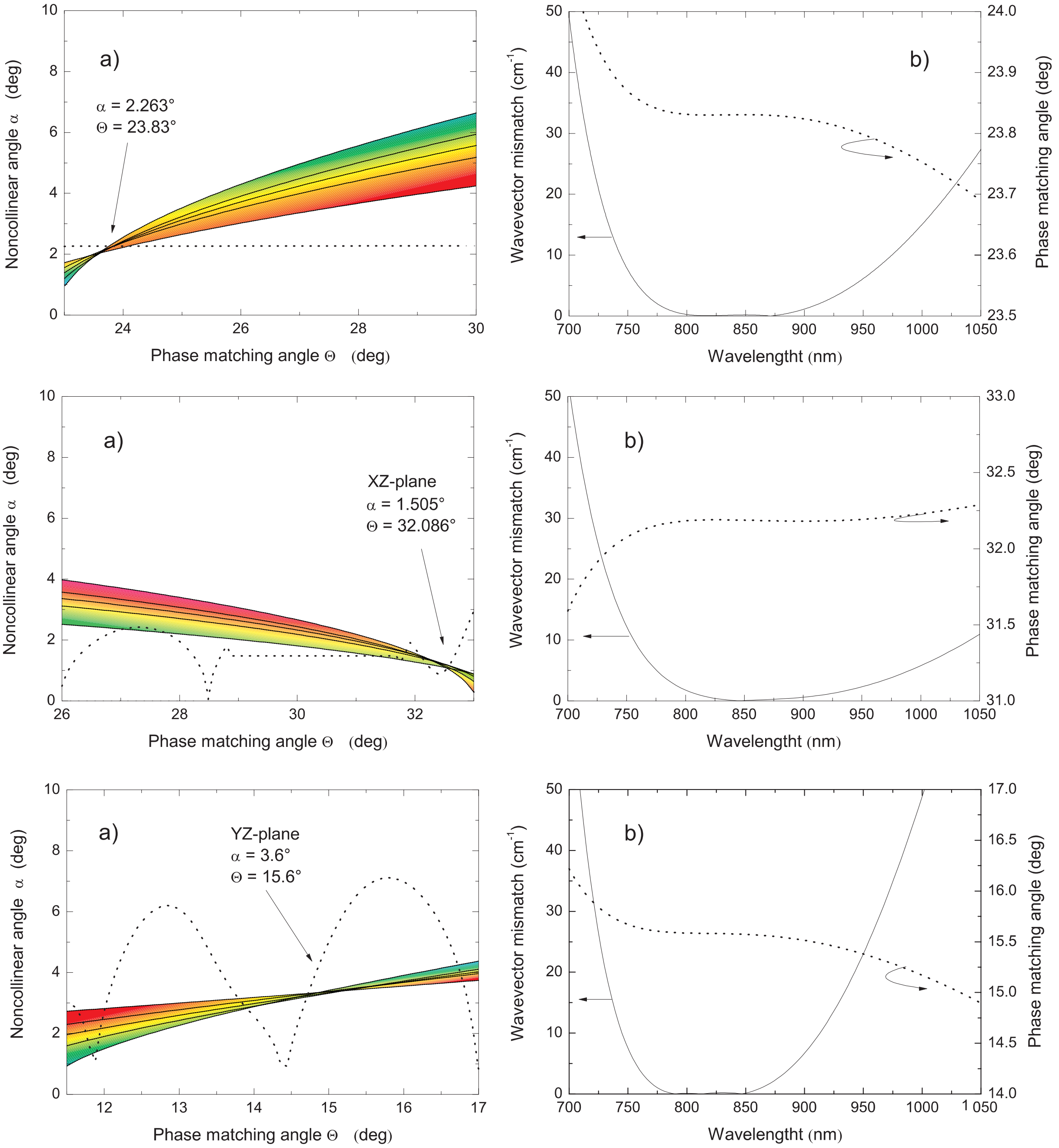

Figure 2.3: (a) A - Variation of the noncollinear angle with the phase matching angle at different signal wavelength (700-nm,800-nm,850-nm,900-nm and 1000-nm, rainbow color), B - variation of the optimum non-collinear angle with the phase matching angle (dotted line); (b) Wave-vector mismatch curve (solid line), phase matching angle versus wavelength (dotted line); The phase matching is calculated for a monochromatic pump at 532 nm; top - BBO, center - LBO, bottom - BiBO crystals.

BiBO, a nonlinear optical crystal for broadband parametric amplification

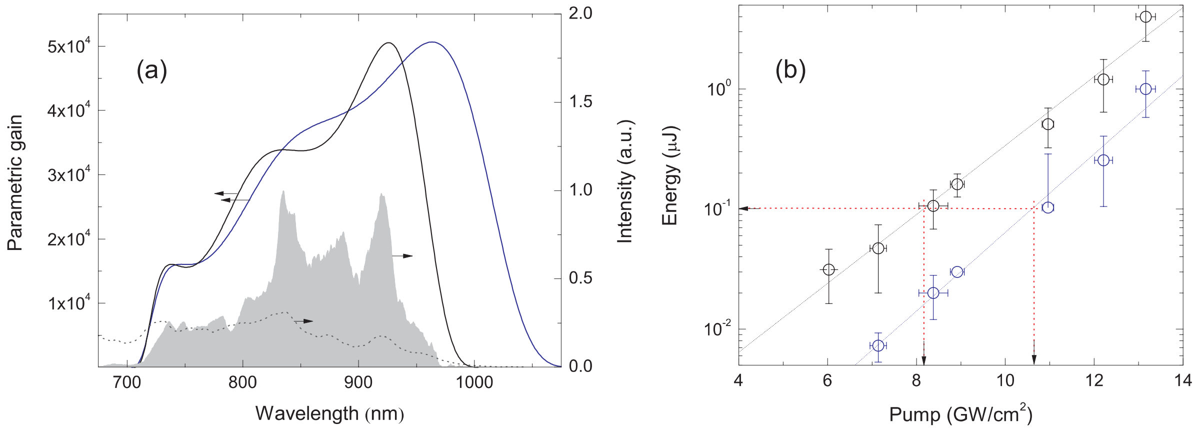

Figure 2.4: Signal amplification in a single OPCPA stage with BBO crystal (blue line) and with BiBO crystal (black line). (a) Calculated parametric gain for 5 mm long BBO and for 4 mm long BiBO OPCPA stage; spectrum of the amplified signal in a single 4 mm long BiBO OPCPA stage (shaded gray line) and seed spectrum (dotted line); (b) amplification of a 20 pJ seed in OPCPA stage on 4 mm BiBO and 5 mm long BBO by variation of the pump intensity in the crystal.

It should be kept in mind, due to the larger effective nonlinear coefficient d_{eff}, BIBO is a very a interesting alternative to BBO. Since BiBO is a positive biaxial crystal, the interaction type is of s-ff-type referring to the YZ-plane as principal plane. It can be used to amplify spectral components from 700-1000 nm in thinner crystals compared to a BBO counterpart. A thinner crystal should be used because of the large non-collinear angle in BIBO to avoid inhomogeneous spatial amplification effects. Figure 2.4(a) shows a comparison between simulation of parametric amplification of 20-pJ seed pulses in single OPCPA stage with 5-mm long BBO and a long 4-mm BiBO crystal. The spectrum of the amplified signal in 4 mm long BiBO stage is additionally shown in Fig. 2.4(a), together with the seed spectrum. Some spectral components in the infrared region are missing, due to the losses in the stretcher and in the Dazzler. The measured energetic amplification curves are shown in Fig. 2.4(b) for both cases simulated in Fig. 2.4(a).

Obviously, the gain in BiBO is substantially higher than for BBO. For the usual first stage operation with BBO crystal and 10.8 GW/cm^2 pump intensity, 100 nJ of amplified signal energy is obtained. Only 8.1 GW/cm^2 pump intensity is required to obtain the same amount of amplified signal energy in BiBO leading to a significant reduction of amplified optical parametric fluorescence in the system (Fig. 2.4(b)).

There are differences in the amplified bandwidth too. The 5-mm long BBO amplifier stage has 50 nm larger bandwidth in the infrared edge reaching 1050 nm compared to the 4-mm long BiBO in figure 2.4(a). The parametric bandwidth for BiBO, which ends at 1 μm, leads not to a drastic reduction of possible transform-limited pulse duration. From the calculated parametric gain spectra in Fig. 2.4(a), a transform-limited pulse duration of 7.8 fs can be obtained for BiBO. The transform-limited pulse duration for the amplified signal (several μJ in energy) shown in Fig. 2.4(a, shaded grey line) is 8.0 fs.

2.2.3 Signal-to-pump pulse duration ratio

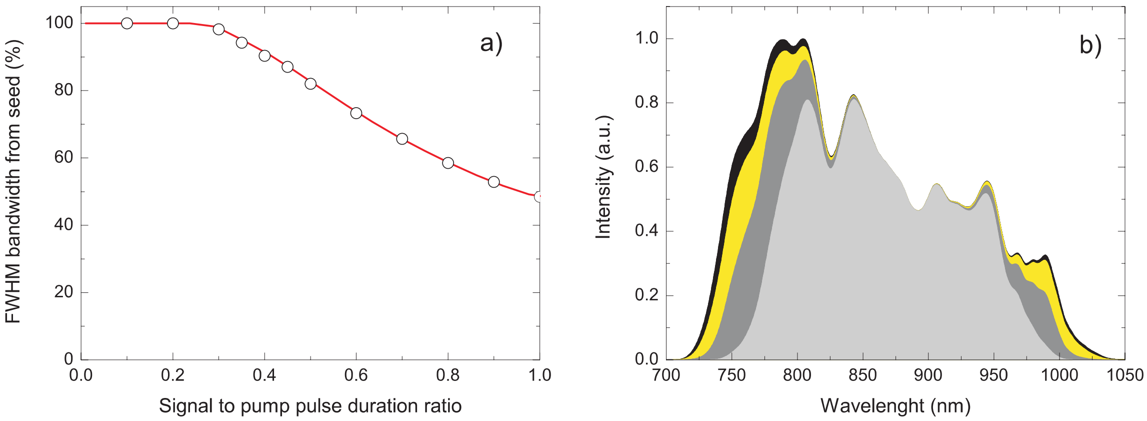

Figure 2.5: (a) Amplification of spectral components (FWHM), depending on the signal-to-pump pulse duration ratio. The red line is a fitted curve, for eye guidance; (b) amplified signal spectrum for different signal pulse duration; 30-ps black, 40-ps yellow, 60-ps grey, 80 ps light grey (the pump pulse duration is 100-ps).

Another yet very important parameter to define is the signal pulse duration at given pump pulse duration. The ideal pump pulse is temporally flat-top shaped [83] in order to have the best gain extraction from the optical parametric amplification process. The spectral components of the signal pulse are furthermore separated in time and are not competing for amplification, thus having a homogeneous gain over the entire bandwidth. The signal pulse duration can be chosen to be very close to the pump pulse duration for a temporally flat-top shaped pump pulse profile. However, simulations are performed to get an estimate for a pump with gaussian-shaped temporal profile. Figure 2.5(a) shows a simulation of a saturated optical parametric amplifier. The effect of gain-dependent spectral narrowing due to signal-to-pump pulse duration mismatch is estimated by variation of the signal pulse duration and assumption of a linear chirp for the signal pulse. As the simulation results show (Fig. 2.5(a)), the spectrum starts to narrow at a signal-to-pump pulse duration ratio of 0.35. A more figurative example is shown in Fig. 2.5(b), where a real signal spectrum is used for simulations. The fully amplified signal spectrum (black shaded curve, Fourier-limited pulse duration FL 8 fs) is amplified for a 30-ps signal pulse duration in a saturated 5 mm BBO OPCPA stage with a pump pulse duration of 100-ps. The spectrum starts slightly to narrow for 40-ps signal pulse duration (yellow shaded curve, Fourier-limited pulse duration FL 8.13 fs). The spectral narrowing effect gets more pronounced for 60-ps pulse duration but the effect is still acceptable (grey shaded curve, FL pulse duration 8.76 fs). For 80-ps the narrowing effect is already remarkable (light grey shaded curve, FL pulse duration

10.26 fs). In our OPCPA setup a pump-to-signal pulse duration ratio of 0.4 is chosen (yellow shaded curve). From simulations, we conclude that a meaningful ratio between the pump and signal pulse duration for temporal gaussian-shaped pump pulse profile should be chosen between 0.4 and 0.6, which is a compromise between energy conversion efficiency and reduction of the pulse-duration-mismatch-dependent spectral narrowing effect.

2.2.4 Techniques for bandwidth engineering

Several methods are established to enhance the parametric bandwidth, which is referred to as bandwidth what satisfies the condition in Eq. 2.5. Simple methods used, and methods that could find a possible application for the OPCPA described in this manuscript are discussed in the next subsections.

Methods not further mentioned are the boost of amplified bandwidth by controlled angular dispersion of the signal (pump) beam [85, 86]. Another way to increase the phase matching bandwidth is a broadband pump beam. The pump chirp is additional parameter to achieve exact phase matching or rather to eliminate the second derivative of phase mismatch Δk in Eq. 2.13. These methods are considered difficult for implementation and require additional care in an already complicated setup, thus not further considered for application.

2.2.5 Parametric interaction length, gain bandwidth

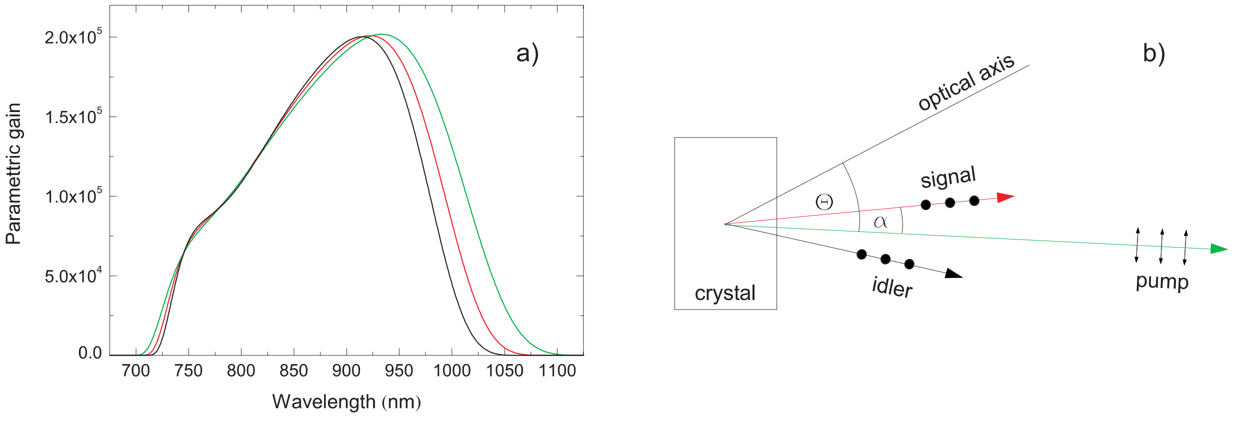

Figure 2.6: (a) Gain bandwidth for 3 mm (green line), 4 mm (red line) and 5 mm (black line) BBO crystal; (b) Type-I phase matching in tangential phase matching geometry.

The most straightforward way to extend the parametric bandwidth is to use thin crystals, to avoid phase accumulation due to the wavevector-mismatch. The parametric gain is consequently lower, but this can be compensated with an increase in pump energy. A higher pump intensity is though limited by the damage threshold of optical coatings and materials and by the generation or rather amplification of optical parametric fluorescence. Figure

2.6(a) shows the calculated parametric gain estimated with Eq. 2.28 for the parametric amplification in a 3-mm, 4-mm and 5-mm BBO long crystal with a monochromatic pump at 532-nm (I_p ~10 GW/cm^2), phase matching with 2.26° noncollinear angle and 23.83° phase matching angle. The phase matching geometry is depicted in Fig. 2.6(b) (TPM-scheme). The amplification bandwidth can be increased, mostly in the infrared spectral region, by use of thin crystals. The increase of parametric bandwidth is however, strongly sub-linear.

2.2.6 Angular detuning in single and multipass stages

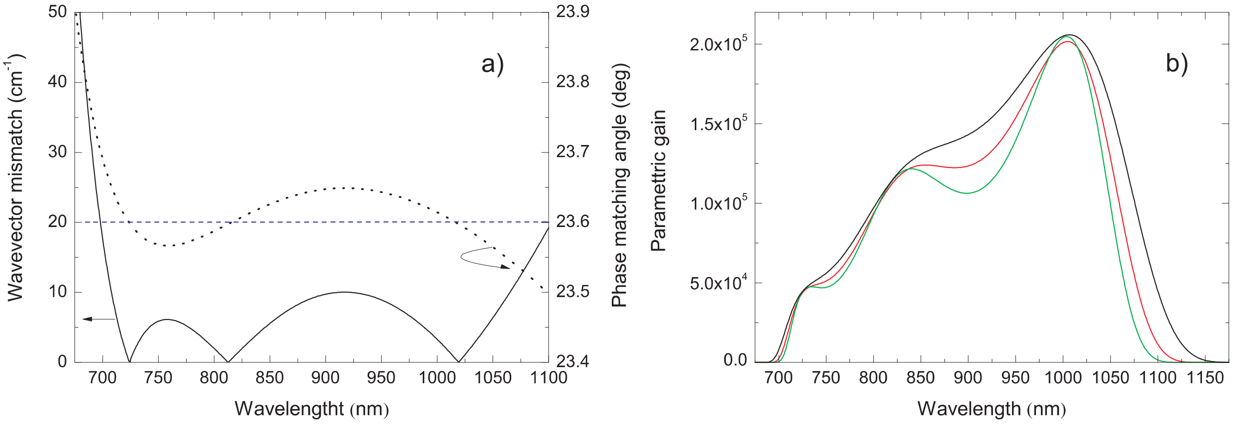

Figure 2.7: (a) Wave-vector mismatch curve (solid line), phase matching angle versus wavelength (dotted black line), fixed value of the phase matching angle used in the simulations (dotted blue line); The phase matching is calculated for a monochromatic pump at 532 nm, 2.08° noncollinear angle and 23.6° phase matching angle (detuned angles); (b) Calculated parametric gain for 3 mm (black line), 4 mm (red line) and 5 mm (green line) long BBO crystal and phase matching conditions from (a).

Another possibility to enhance the parametric bandwidth is to apply angular detuning in a single or multipass-(double)pass amplification scheme [33],[84]. In that way, signal and pump beam directions (in the case of a double-pass stage probably the returning beam) can be slightly detuned from the optimum values of non-collinear and phase-matching angles, for largest parametric gain (parameters from Fig. 2.3(b) - BBO), to favor the amplification of different spectral components. Figure 2.7(a) shows phase matching for 2.08° noncollinear angle and 23.6° phase matching angle. The calculated parametric gain for divers crystal thickness is shown in Fig. 2.7(b) and can be directly compared to the calculated parametric gain curves from Fig. 2.6(a). Moreover, the temporal delay between signal and pump pulse can be changed to obtain an additional degree of freedom to reduce or enhance the parametric gain for certain parts of the pulse spectrum. This is convenient if the pump is not temporal flat-top shaped as is usually the case. Unfortunately, this method is more complicated to reproduce compared to other methods.

2.2.7 Multiple beam pumping

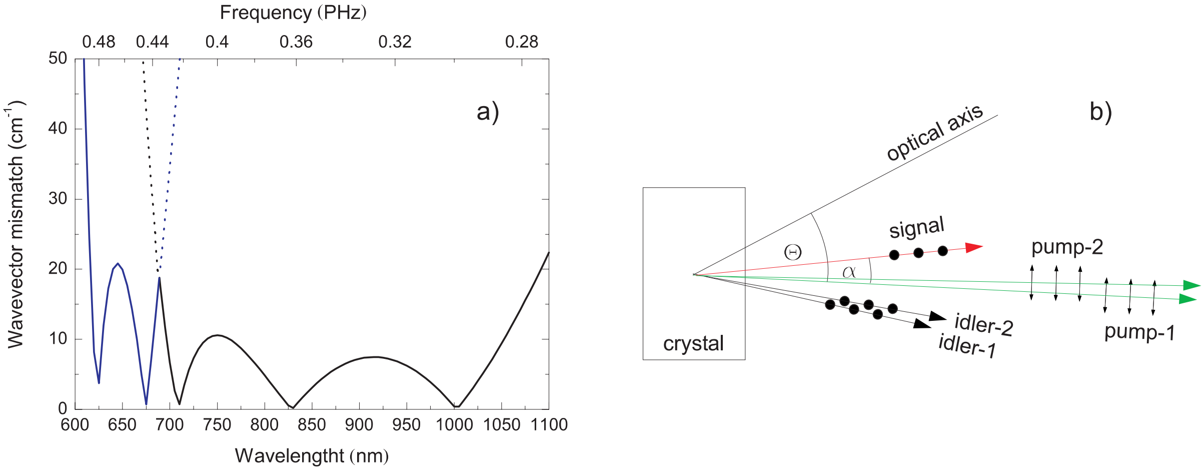

Figure 2.8: (a) Wave-vector mismatch curve for two pump beams at 532-nm (for further details, see text); (b) Type-I phase matching in tangential phase matching geometry with two pump beams.

A way to extend the parametric bandwidth, which is not too difficult to implement, but not yet used in the current OPCPA amplifier is, pumping with several beams in a single-pass geometry (Fig. 2.8(b)). The wavelength of the additional pump beams may differ from the main pump but it is easier and more straightforward to use the same pump source [87, 88]. The wave-vector mismatch for a 532-nm double-beam pumped scheme in type-I BBO is shown in Fig. 2.8(a). The curve consists of two assembled parts. One is the maximum phase matching bandwidth reached with angular detuning, with the non-collinear and the phase-matching angles at α=2.065° and Θ=23.6° (black curve). The second part intersects the first part at 690-nm. An example of phase matching is shown for the second pump beam with non-collinear and the phase-matching angles at α=0.2° and Θ=22.345° (blue curve). The first beam (black) covers a spectral range of ∼150 THz. The second pump beam (blue) ∼50 THz. The interesting part is the possibility to reach a transform-limited pulse duration around 6 fs which should be feasible using this arrangement of beams. However, the challenges for the implementation of a multiple pumping scheme are manifold. The pump pulse duration should be matched to the spectral signal region of interest for each beam respectively. Damage threshold issues has to be considered due to the simultaneous presence of multiple pump beams impinging on the crystal. Precise timing between the two pump beams is necessary, while keeping the relay imaging for the pump beam in both beam arms. Additionally, multiple beam diffraction of signal and idler on the optical pump grating is present in this scheme.

2.3 Simulation techniques for optical parametric amplification

2.3.1 Analytical description for the small gain regime

In parametric amplification we are concerned with the interaction of three harmonic waves. Optical parametric amplification is a special case of difference frequency generation and can be described by a set of coupled wave equations. A very simple analytical expression can be derived for the small gain regime solving the coupled wave equations assuming zero pump depletion.

$$\begin{aligned}\frac{d\tilde{A}_s}{dz} &= -j\kappa\tilde{A}_i^*\tilde{A}_p e^{-j\Delta kz}, \\ \frac{d\tilde{A}_i}{dz} &= -j\kappa\tilde{A}_s^*\tilde{A}_p e^{-j\Delta kz}, \\ \frac{d\tilde{A}_p}{dz} &= -j\kappa\tilde{A}_s\tilde{A}_i e^{j\Delta kz} = 0.\end{aligned} \tag{2.27}$$

κ is the coupling coefficient, $\tilde{A}_{p,s,i}$ are the complex amplitudes of the pump, signal and idler waves and Δk is the wavevector mismatch (p, s and i are the indices for the pump, signal and idler waves). The derivation of these equations is not explained in detail, it is available in several references [70, 90–93]. Nevertheless, the solution for the parametric gain is given in Eqs. 2.28 and 2.30, as it gives a concise description of the interrelationship between important parameters of amplification. The parametric intensity gain for the signal wave is obtained from the solution of a homogeneous second order differential equation

$$G = 1 + (\kappa\tilde{A}_p l)^2\frac{\sinh^2\Gamma}{\Gamma^2}. \tag{2.28}$$

with

$$\Gamma = \sqrt{(\kappa\tilde{A}_p l)^2 - (\frac{\Delta kl}{2})^2} \quad \text{and} \quad \kappa = d_{eff}\sqrt{\frac{\omega_s\omega_i\omega_p}{n_s n_i n_p}}\frac{\sqrt{2\hbar Z_0}}{c_0}. \tag{2.29}$$

l is the parametric interaction length, d_{eff} is the effective nonlinear optical coefficient, $\omega_s, \omega_i, \omega_p$ and n_S, n_i, n_p are the angular frequencies and the refractive indices of the signal, idler and pump waves in the nonlinear medium, respectively and Z_0 is the impedance of free space. This equation can be simplified for $\Delta k = 0$ to

$$G \simeq \sinh^2\kappa A_p l \quad \text{with} \quad A_p \propto \sqrt{I_p}. \tag{2.30}$$

This model is useful for first estimations of OPCPA parameters and it gives a clear picture for the small gain regime. Additional regard must also be paid to the spectral phase analysis of amplified broadband chirped pulses (see Sect. 2.1).

However, the numerical simulation of the OPCPA process is essential to describe the process dynamics in detail [121] for example pump depletion and amplification of optical parametric fluorescence [84], as well as for the description of spatial effects.

2.3.2 Numerical simulation

Two methods are commonly used for the simulation of parametric amplification processes. The Split-step method handle propagation effect in the spectral domain using Fourier transforms, whereas the differential coupled equations are solved in space-time domain. The other possibility is to decompose each wave in plane wave eigenmodes and solve coupled differential equations for the slowly varying eigenmode amplitudes (*Fourier-space* method) [94]. This method has the advantage of higher accuracy but needs more computational resources than a split-step scheme. Therefore, split-step methods are more widely used being faster but lacking highest accuracy.

The OPCPA system is modeled numerically using a symmetrized Split-Step type method [94, 95]. In this approach, we handle the parametric amplification process in the time domain (*nonlinear step*). The walk-off effect due to the noncollinearity of the Type-I parametric process is taken into account by shifting the respective field at each loop-step in the direction given by the noncollinear process by adding a first-order term to the spatial phase in Eq. 2.34. Higher-order dispersion and diffraction terms can also be accommodated by adding the corresponding spectral and spatial phase terms in the Fourier domain (Eq. 2.33) and (Eq. 2.34) (*linear step*). This becomes necessary if the pulse duration is short (dispersion effects) or in the case of very small beam sizes (diffraction effects).

It is important to note, that temporal walk-off due to group-velocity mismatch can usually be neglected in our case because of the long pulses used (40 ps), and the diffraction effects are not important owing to their weak relative impact for unfocused beams. However, for the correct description of amplified optical parametric fluorescence (AOPF), spatial effects such as the spatial walk-off for the amplification of fluorescence in three wave mixing processes are important [96].

The data matrix used in the simulation consists of an array

$$\mathrm{data}_i = [-R, R] \times [0, T] \tag{2.31}$$

for each wave (signal, AOPF in the signal direction, idler, AOPF in the idler direction and pump). The factor R is the radial limit of the beam in the spatial domain which is usually more than three times larger than the FWHM diameter of the pump beam. T is the temporal simulation window which is 3 times the pump pulse duration at FWHM. In the simulation we use a matrix with a grid size of 80x80 and 1000 split-step iteration loops. This choice of parameters represents a compromise between calculation resolution and time required for computation as we used a PC to carry out the simulation.

2.3.3 Nonlinear step

Since the phase-mismatch (Δk) for the amplified signal and AOPF differs, the only way to take into account both amplified field pairs is to simulate the amplification of both fields in interchangeable steps using the same pump intensity. Phase matching effects are included for signal and idler beams by estimating the frequency dependent Δk values in the time domain. The spectral components of the seed in the first stage range from 675 nm to 1050 nm, which is the acceptance bandwidth of the stretcher. In the simulation of the subsequent stages the spectral span of the signal and the AOPF in the signal direction are inherited from the previous stage. The Δk for the AOPF is assumed to be zero. This approximation is believed to be consistent since the rate of transition from a pump photon to a signal and an idler photon is higher in the direction of the smallest phase-mismatch and only in that case the OPF can be efficiently amplified from the quantum noise level.

The presence of the OPF is accounted by adding the quantum noise field terms into the coupled wave equations [96, 97]. Therefore, the nonlinear coupled wave equations can be written in a following form

$$\begin{aligned}
\frac{\partial A_1}{\partial z} + \alpha_{1m}\frac{\partial A_1}{\partial t} + ... + \frac{j\beta_{1n}}{r}\frac{\partial}{\partial r}(r\frac{\partial A_1}{\partial r}) + ... + \gamma_1\frac{\partial A_1}{\partial r} &= j\kappa_1 A_2^* A_1 e^{-\Delta k_1 z} + \sqrt{\varepsilon}_1\xi_1(z,t), \qquad (2.32)\\
\frac{\partial A_2}{\partial z} + \alpha_{2m}\frac{\partial A_2}{\partial t} + ... + \frac{j\beta_{2n}}{r}\frac{\partial}{\partial r}(r\frac{\partial A_2}{\partial r}) + ... + \gamma_2\frac{\partial A_2}{\partial r} &= j\kappa_2 A_1^* A_3 e^{-\Delta k_2 z} + \sqrt{\varepsilon}_2\xi_2(z,t),\\
\frac{\partial A_3}{\partial z} + \alpha_{3m}\frac{\partial A_3}{\partial t} + ... + \frac{j\beta_{3n}}{r}\frac{\partial}{\partial r}(r\frac{\partial A_3}{\partial r}) + ... + \gamma_3\frac{\partial A_3}{\partial r} &= \quad j\kappa_3 A_1 A_2 e^{\Delta k_3 z} + \sqrt{\varepsilon}_3\xi_3(z,t),
\end{aligned}$$

where κ_l are the nonlinear coupling coefficients [93] calculated for the central frequencies, A_l, with $l = 1...3$ represent the normalized complex field amplitudes for the signal (or the superfluorescence field in signal direction), idler (or the superfluorescence field in idler direction) and pump fields, respectively. For the description of the noise fields we will use the approach first introduced by Gatti *et al.* [97]. The complex stochastic variables $\xi_l(z,t)$ have a gaussian distribution with a zero mean value $\langle\xi_l(z,t)\rangle = 0$ and the correlation $\langle\xi_l(z,t)\ \xi_j^*(z',t')\rangle = \delta_{l,j}\delta(t-t')\delta(z-z')$. Here ε_i are the noise intensities of the respective fields. A similar approach was used to describe the influence of temporal and spatial walk-off during the parametric amplification of stochastic fields [96]. The intensity ε_3 is set to zero as the pump field is already initialized with the complex amplitude A_3. α_{im} are the dispersion coefficients with order m whereas β_{in} are the diffraction coefficients with order n. γ_i is the spatial walk-off coefficient due to the noncollinear geometry of interaction. This coefficient for the pump (γ_3) is in our case zero as the pump propagates normal to the crystal plane. The pump beam displacement due to Pointing vector walk-off is small compared to the beam apertures and is not taken into account in the simulation.

2.3.4 Linear step

Dispersion effects are taken into account in the frequency domain [71]. $\Delta\varphi_t(\omega)$ is the spectral phase expanded in a Taylor series.

$$A_l(r, z + \Delta z, t) = \mathcal{F}^{-1}\left\{\mathcal{F}\left\{A_l(t, z)\right\} e^{j\Delta\varphi_t(\omega)}\right\} \tag{2.33}$$

$\mathcal{F}$ is the Fourier transformation $\mathcal{F}^{-1}$ is the inverse Fourier transformation.

The effects of diffraction and the walk-off due to the noncollinearity of the type I parametric process is taken into account by adding a spatial phase term $\Delta\varphi_r(\omega)$=$\Delta\varphi_{nc}(\omega) + \Delta\varphi_{diff}(\omega)$ (the subscripts *nc* and *diff* correspond to the noncollinear and diffraction terms respectively) in Eq. 2.34 by applying the same Fourier (linear) step to the transposed $[-R, R] \times [0, T]$ data matrices $A_l^\dagger(r, z + \Delta z, t)$.

$$A_l^\dagger(r, z + \Delta z, t) = \mathcal{F}^{-1}\left\{\mathcal{F}\left\{A_l^\dagger(t, z)\right\} e^{j\Delta\varphi_r(\omega)}\right\} \tag{2.34}$$

To improve agreement between simulation results and experiments, the noise intensities ε_l have to be found empirically for the first simulation run. One possibility to estimate the noise intensities is to measure the AOPF in absence of the seed, simulate the system with the same pump intensity and tune the input noise intensities such to obtain the same AOPF output as in the experiment. This method is reliable if the ratio between energies of the amplified signal and AOPF is large and for the amplifier stage far from gain saturation.

2.4 Signal and amplified optical parametric fluorescence

The pulse contrast ratio in a multi-TW amplifier is of major concern, because many high-field experiments require a clean pulse front. The pulse front in an optical parametric chirped pulse amplifier is free of pre-pulses as showed in previous measurements [98], but consists of a large pedestal of incompressible amplified optical parametric fluorescence, which can reach considerable intensities. A typical AOPF spectrum is shown in Fig. 2.9. AOPF originates from a quantum effect known as optical parametric fluorescence. A detailed description of the theory of optical parametric fluorescence (OPF) is given in [99] by D.A. Kleinman, a considerable contribution to this theory was given by R. Glauber. He derived the transition rate equation for OPF in [100]. More about quantum noise in parametric processes is given in references [101, 103]. A more practical picture of the generation and amplification of optical parametric fluorescence is obtained by introducing a critical decay length for OPF introduced by L. Carrion *et al.* [104]. Important to mention is the theoretical and experimental work performed in connection with optical parametric oscillators and optical parametric generators [105, 106]. Theoretical and experimental investigation on generation and amplification of OPF in OPCPA has been performed in recent work on this subject [84, 107, 108].

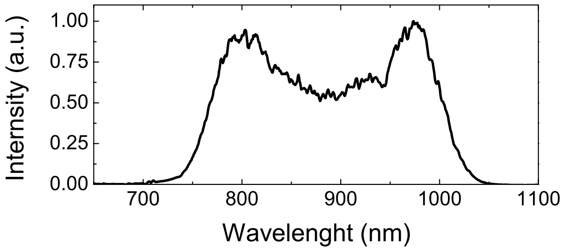

Figure 2.9: Amplified optical parametric fluorescence spectrum from a 5-mm long BBO OPCPA stage pumped with ~20 GW/cm^2, close to the damage threshold.

The spontaneous downconversion of the pump photons into idler and signal photon pairs [99, 109] can be described by the Hamiltonian of the system considering two electromagnetic field modes A_s and A_i which are coupled to a field with an oscillation frequency $\omega_p = \omega_s + \omega_i$, fulfilling the energy conservation condition for the system [97, 110]. The Hamiltonian of the system is given by

$$H = H_0 + H_{nli} \tag{2.35}$$

with H_0, the free evolution (field) Hamiltonian combined with the external driving term

$$H_0 = \sum_{j=p,s,i} \hbar\omega_j (a_j^\dagger a_j + \frac{1}{2}) \tag{2.36}$$

and

$$H_{nli} = -\hbar\kappa[a_s^\dagger a_i^\dagger a_p + a_s a_i a_p^\dagger] \quad \text{with} \quad a_p = e^{-i\omega_p t}, \tag{2.37}$$

the nonlinear interaction Hamiltonian which describes the coupling between the signal and idler waves. The symbol κ is used for the coupling strength in this section and is given by the nonlinear coupling coefficient (see Eg. 2.29) times the complex amplitude of the pump wave. a_s, $a_s^\dagger$, a_i and $a_i^\dagger$ are the time-dependent photon annihilation and creation operators for the modes A_s and A_i. The usual way to proceed to get a formal quantum mechanical description for optical parametric fluorescence is to solve the master equation of motion and initiate the OPF fields by a medium or vacuum field [97]. In this case, starting from the Heisenberg equation of motion

$$\frac{da_s(t)}{dt} = \frac{1}{i\hbar}[a_s, H] = -i\omega_s a_s + i\kappa a_i^\dagger e^{-i\omega_p t} \tag{2.38}$$

$$\frac{da_i^\dagger(t)}{dt} = \frac{1}{i\hbar}[a_i^\dagger, H] = i\omega_i a_i^\dagger - i\kappa a_s e^{+i\omega_p t}, \tag{2.39}$$

a solution can be obtained for the operators $a_s(t)$ and $a_i^\dagger(t)$ and used to derive the number operator $N_s(t)$ (and $N_i(t)$). The number operator is defined as $N = a^\dagger a$. It represents a measure for the number of photons in the state $|n_{a_s}\rangle$ (and $|n_{a_i}\rangle$). Integration of Eqs. 2.38 and 2.39, immediately yields

$$a_s(t) = e^{-i\omega_s t}[\cosh(\kappa t)a_s + i\sinh(\kappa t)a_i^\dagger] \tag{2.40}$$

$$a_i^\dagger(t) = e^{i\omega_i t}[\cosh(\kappa t)a_i^\dagger - i\sinh(\kappa t)a_s] \tag{2.41}$$

$$N_s = \cosh^2(\kappa t)a_s^\dagger a_s + [1 + a_i^\dagger a_i]\sinh^2(\kappa t) + \frac{i}{2}\sinh(2\kappa t)[a_s^\dagger a_i^\dagger - a_s a_i] \tag{2.42}$$

The initial condition for the system is

$$|\Psi(0)\rangle = |n_{a_{s0}} = 0\rangle|n_{a_{i0}} = 0\rangle|n_{a_p}\rangle. \tag{2.43}$$

with the modes A_s and A_i devoid of photons. The number of photons in the state $|a_s\rangle$ for the system is given by

$$N_s(t) = \langle a_s^\dagger(t)|a_s(t)\rangle \tag{2.44}$$

$$\begin{aligned} &= \langle n_{a_{s0}}, n_{a_{i0}}|\cosh^2(\kappa t)a_s^\dagger a_s + [1 + a_i^\dagger a_i]\sinh^2(\kappa t) + \tfrac{i}{2}\sinh(2\kappa t)[a_s^\dagger a_i^\dagger - a_s a_i]|n_{a_{s0}}, n_{a_{i0}}\rangle \\ &= n_{a_{s0}}\cosh^2(\kappa t) + (1 + n_{a_{i0}})\sinh^2(\kappa t). \end{aligned}$$

An interesting result is obtained for the vacuum state $|0,0\rangle$ at arbitrary time t.

$$\langle 0,0|N_s(t)|0,0\rangle = \sinh^2(\kappa t) \tag{2.45}$$

This result shows, that signal (and idler) photons will be created through spontaneous decay from a pump photon in a rate proportional to the nonlinear coupling strength or equivalently proportional to complex amplitude of the pump. The rate of idler and signal photon generation is identical according to the energy conservation condition. This follows also implicitly from the Manley-Rowe equation, which can be directly derived from the equations of motion 2.38 and 2.39

$$\frac{da_s^\dagger a_s}{dt} = \frac{da_i^\dagger a_i}{dt}. \tag{2.46}$$

Since $N_s = a_s^\dagger a_s$ and $N_i = a_i^\dagger a_i$ are the expectation values for the states $|n_{a_s}\rangle$ and $|n_{a_i}\rangle$ follows,

$$N_s(t) - N_s(0) = N_i(t) - N_i(0). \tag{2.47}$$

This implies an equal number of idler and signal photons creation.

So far, the quantum mechanical description of optical parametric fluorescence gives a clear picture of the process. A more convenient alternative to strict quantum-mechanical treatment of optical parametric fluorescence generation and amplification in OPCPA is

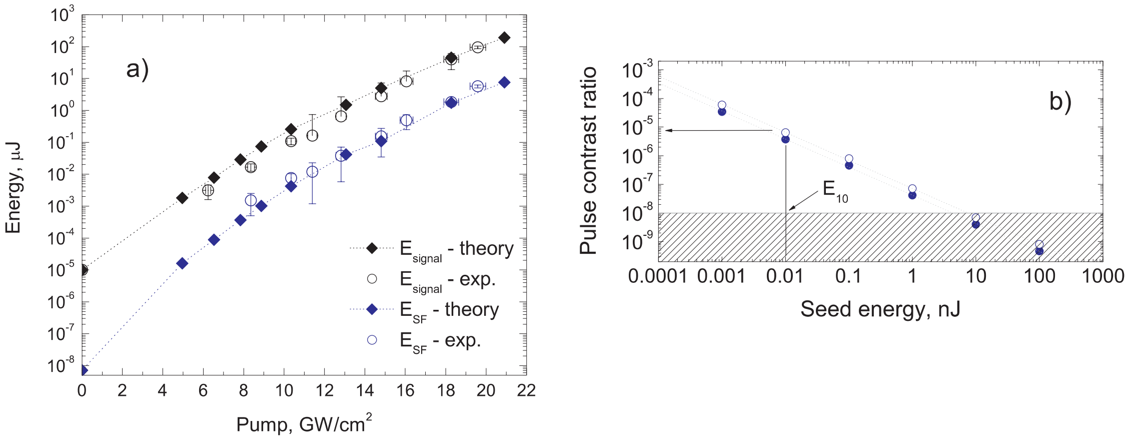

Figure 2.10: (a) Dependencies of the amplified signal and AOPF energies on the pump intensities in the first stage; (b) Pulse contrast ratio improvement when higher energy seed pulses are used; E_{10} is the seeding energy of the present OPCPA system; the simulation is performed for compression to 10 fs (empty circle) and to the transform limited pulse duration which is 7.2 fs (blue circle); SF superfluorescence or equivalently amplified optical parametric fluorescence.

numerical simulation using stochastic fields [110]. This method is explained in section 2.3.2 and used in the next subsections to describe the amplification of OPF in optical parametric chirped pulse amplifiers.

2.4.1 Simulation without saturation effects

In the first OPCPA stage, optical parametric fluorescence is generated by downconversion [111, 112], and subsequently amplified. This already amplified OPF is merely further amplified in the next stages.

The AOPF and signal energy levels are measured between pJ and mJ-level in some case for strongly fluctuating signals (in non-saturated amplifier stage). The energy measurements are not to be underestimated. The measurements are performed several times at different days for each OPCPA stage in order to obtain consistent data sets. The optical parametric fluorescence is measured by blocking the signal beam in front of the first OPCPA stage.

The energy evolution of the amplified signal and amplified optical parametric fluorescence (AOPF) versus pump intensity is depicted in Fig. 2.10(a) for the first amplification stage. It is evident that the experimental points show agreement with the calculations. Starting from the measurements and calculations for the first stage, the AOPF has much more favorable phase matching conditions than the seed due to the angular dispersion of it's frequency components and due to the fact that it has the same amount of downconverted signal and idler photons from the moment of generation (after propagation through the critical length for parametric generation in the crystal [104]). Whereas the signal needs

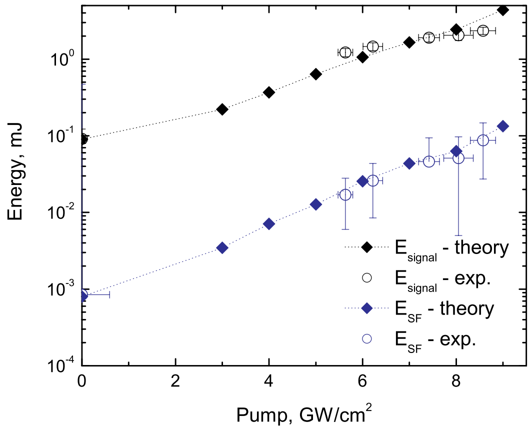

Figure 2.11: Dependence of the amplified signal and AOPF energies on the pump intensities in the second stage; SF superfluorescence.

a longer propagation distance to build-up a comparable amount of idler photons for the parametric amplification. In our case the signal after the propagation through this critical length is approximately 10^3 times stronger than the AOPF. The best pulse contrast ratio that can be obtained from this OPCPA stage is $4{\cdot}10^{-6}$, if the signal is compressed to the transform limit as shown from simulation results (Fig. 2.10(b)). To explore the connection between seed energy and temporal pulse contrast, simulation of the 1^{st} stage is carried out by varying the seed energy. This plot is not valid in the case of saturated amplification. The pulse contrast ratio is simulated numerically for an input seed energy varying from $5{\cdot}10^{-3}$ to $5{\cdot}10^4$ times the current seed energy E_{10} of 20 pJ. We conclude that AOPF deteriorates the pulse temporal contrast ratio in the first stage as a consequence of the low seed energy in combination with the high pump intensities used in this stage to obtain high gain on the order $> 10^4$. Therefore, a straightforward way to increase the pulse contrast ratio in an OPCPA would be to develop a stronger seed source or optimization of stretcher and adaptive dispersion control efficiency. However, this cannot lead to arbitrary improvement of pulse contrast because, as we can deduce from the results presented in Fig. 2.10(b), it makes not much sense to use seed energies bigger than 10 nJ. The final limitation for such seeding is the contrast of the ultrabroadband oscillators (in the ±5 ps temporal window) [113, 114] marked as a shadowed area in Fig. 2.10(b). Nonlinear pulse cleaning methods such as the cross-polarized wave generation [115] or the plasma mirror [116], which were developed for use with convention CPA systems, could be used to improve pulse contrast beyond the oscillator contrast. Unfortunately, both techniques are difficult to implement and the result is, reduced output energy with a tremendously increase of the setup complexity.

The energy evolution in the second amplification stage of the amplified signal and AOPF versus the pump intensity is depicted in Fig. 2.11. For the numerical code we used

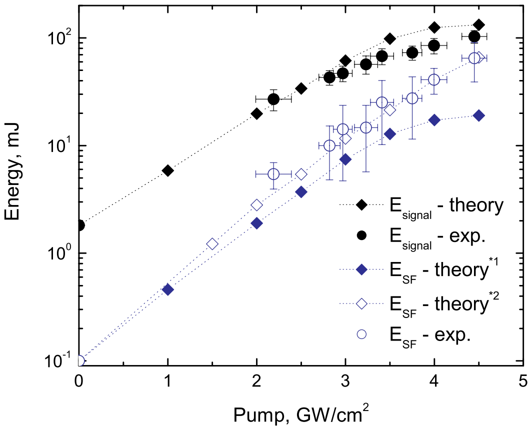

Figure 2.12: Dependencies of the amplified signal and superfluorescence energies on the pump intensities in the third stage; SF superfluorescence.

90 μJ and 850 nJ input energies for the signal and AOPF, respectively. These energies are obtained using ~18 GW/cm^2 pump intensity in the first stage. From this data we can conclude, that there are noticeable discrepancies between experimentally measured and calculated signal energies. This could be explained if we remember that the second stage in our setup is not only used to reach the mJ-level but also to favor the amplification of the spectrum edges to compensate for the smaller amplification in this region. Slight angular detuning in the second OPCPA stage allows us to reshape the gain bandwidth [117] and reduce the amplification bandwidth narrowing throughout the amplifier. This causes lower gain for the signal due to increased phase mismatch. Therefore, we attribute this discrepancy between experimental and calculated results to the difference between the Δk values used in the experiment and in the numerical code. For the calculation of the OPF amplification we kept again the assumption of perfect phase matching ($\Delta k = 0$).

Another important experimental observation is that the pulse contrast does not deteriorate much in the 2^{nd} stage. This result can be attributed to the common action of the low gain (~ 20) and angular detuning. The observed energy difference and the known compression ratio allows us to estimate the pulse contrast in the current system to be $\sim 2 \cdot 10^{-5}$ for the 2.3 mJ pulses. Previously, pulse contrast ratio for similar pulse energies in a two stage OPCPA was measured after compression to $\sim$ 10 fs pulse duration (first stage in double-pass, second stage in single-pass configuration) [98]. The best result obtained was $\sim 5 \cdot 10^{-5}$.

2.4.2 Simulation with saturated amplifier

Saturation is reached for the signal in the last amplifier stage of our system (Fig. 2.12(a)). In the simulation we used 1.8 mJ and 100 μJ input energies for the signal and AOPF,

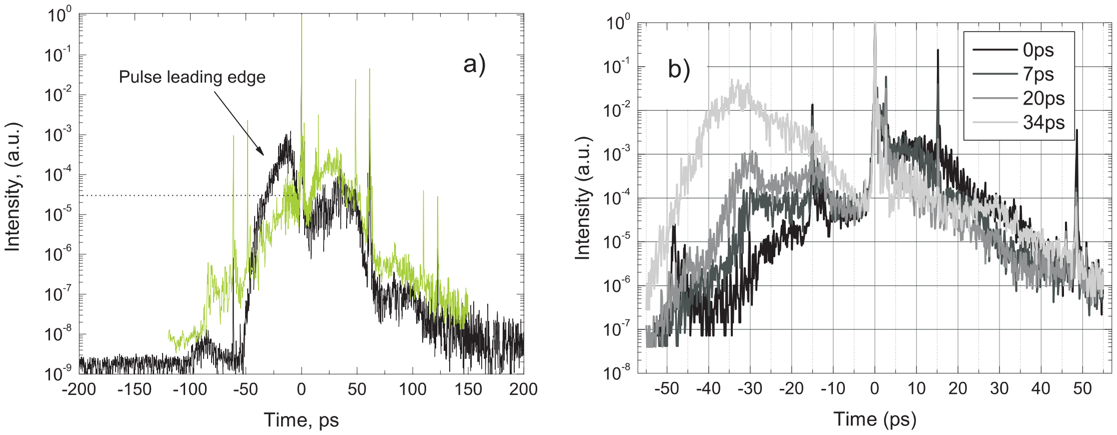

Figure 2.13: (a) Pulse contrast measurement by third order autocorrelation in the ps-range; black curve - pulse contrast for zero delay between pump and seed (zero delay corresponds to the delay when the highest pulse contrast was observed); green curve - seed pulse is 14-ps earlier compared to zero delay; (b) dependencies of the pulse contrast on the delay between pump and seed.

respectively. These energies are obtained using ~7 GW/cm^2 pump intensity in the second stage (Fig. 2.11). Gain saturation improves the amplified signal energy stability which was 5% rms obtained with a pump energy stability of less than 2%. As already mentioned in the experimental setup description, the usual procedure to measure the AOPF in an OPCPA stage is to block the seed in front of the first stage. However, in the absence of the seed, the pump energy is used only for the AOPF amplification and as a consequence the AOPF will be amplified to higher energy than in presence of the signal. In the first two stages this effect is not so pronounced as the difference between signal and pump energies is substantial but in the last amplifier stage the pump and amplified signal energies are comparable. It has to be mentioned, that no optical parametric fluorescence itself is generated in the third stage due to the moderate pump intensities, but saturation effects starts to play a role. For that reason, calculations are performed for OPF amplification with and without presence of the seed (Fig. 2.12 superscripts ^{*1} and ^{*2}, respectively), for the third stage of amplification. It is evident that the presence of the seed causes parametric gain quenching [118]. For a gain of 50 the ratio between the signal and AOPF energies is about 1:7 instead of 1:2 as shown in Fig. 2.12). From this result we conclude that due to moderate gain in this stage even gain saturation does not substantially deteriorated the pulse contrast (only ~ 4 times).

Avoid amplified optical parametric fluorescence

AOPF is produced within the time window defined by the pump pulse, as parametric amplification and optical parametric fluorescence generation depends on an instantaneous and directional interaction. The OPF is generated in the optimum phase-matching direction, and the direction depends intrinsically on the pump wave direction in the nonlinear crystal. Third-order correlation traces presented in Fig. 2.13(a) are adequate for the better understanding of the amplification dynamics of OPF. A quenching effect can be observed in presence of a signal pulse, specially in a saturated OPCPA stage. A more detailed description of the measurement is given in Sect. 3.6.3. The temporal contrast in the leading pulse front is best at around 0-ps time delay (defined as optimum pump-seed overlap), where the signal overlaps with the leading edge of the pump pulse. Whereas at ±50-ps the signal is already negligible and AOPF gains more amplification.

There are several ways to suppress AOPF in ultra-broadband OPCPA. One possibility is to decrease the parametric gain while sufficient output energy is maintained by increasing the effective beam size in the amplifier stage or by decreasing the pump energy. An alternative is to add another OPCPA stage which would in turn complicate the setup. A detailed study of the parametric gain control in multi-stage OPCPA system is presented in Ref. [84] for three OPCPA stages.

Tight spatial filtering between the amplification stages is another possibility. The AOPF has a larger divergence angle compared to the signal because of the directional dependence on optimum phase-matching in the nonlinear crystal. This quality of the signal can be used to filter part of the AOPF. However, investigation of effective AOPF suppression by spatial filtering is still missing in scientific literature [119].

A third way to decrease AOPF is to change the temporal overlap between the pump pulse and stretched seed and thus obtaining the best overlap at the pump pulse leading edge 2.13(a). In our previous work [98] we showed that shifting the relative delay between the pump and the seed by ~ 30 ps towards the pump leading edge improves the contrast by one to three orders of magnitude 2.13(b).

Pump intensity is not the only factor affecting the pulse contrast deterioration. The saturation of an OPCPA stage and angular detuning of the amplifier crystal contributes as well to the decreased contrast as already mentioned in subsection 2.4.1. If the temporal contrast is such to compromise a contrast-sensitive experiment and if the last OPCPA stage is saturated, the universal remedy is to work with unsaturated last stage. This might decrease the output energy and its stability substantially but several orders of magnitude temporal contrast can be gained. On the longer term, to be able to use the OPCPA amplifier in saturation, a contrast cleaning scheme has to be implemented or a stronger seed should be obtained either by loss-optimized stretcher design or by stronger seed source. The optimization of the stretcher is not straightforward. A stretcher design optimized for throughput efficiency can be complicated for alignment and might require in turn a lossy compressor, as is for example a grating compressor for broadband pulses.

An interesting aspect which is often omitted, is the contrast on the few-ps and fs-scale. In this range, deterioration of the compressed pulse contrast ratio is expected due to sharp features in the spectral edges of the amplified signal spectrum [120]. This is an interesting feature of amplified ultrabroadband pulses but should not constitute a problem for high-field experiments in terms of pre-plasma generation.

2.5 Influence of the amplified spectrum on the presence of gain saturation

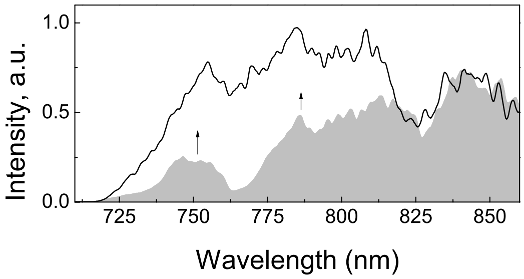

Figure 2.14: Saturation effect in OPCPA stage. Spectrum of a non-saturated OPCPA (shaded grey curve); OPCPA in saturation (black curve).

Spectral components of the signal beam are amplified according to Eq. 2.30 in the linear regime of amplification. This equation underlines the typical exponential behavior of the parametric process. In this regime the energy fluctuation of the signal depends on the energy fluctuation of the pump beam. An improvement in energy stability is reached in the saturation regime but it still depends on the energy stability of the pump [121].

The truly interesting side of saturation is the effect of pump-intensity-dependent gain saturation. Due to the gaussian temporal shape of the pump , signal spectral components which are temporally separated along the pump pulse will experience different gains. The spectral components overlapping with the central part of the pump beam will reach saturation earlier than spectral components in the wings. The wings of the signal pulse still experience the linear regime of amplification until saturation is reached. This is apparent from the measurement in Fig. 2.14. The shaded grey spectrum of an unsaturated signal beam reaches saturation (black curve) and the wings of the spectrum are amplified.

Unfortunately this effect favors the amplification of OPF. AOPF can reach as well noticeable energy during the saturation of the signal, as different spectral components of OPF compete for gain and in turn degrade the pulse temporal contrast.

2.6 Amplifier sensitivity to angle variation

The gain of the non-collinear OPA-process has high angular sensitivity. The effect of angle variation in a BBO-crystal based OPCPA is shown in Fig. 2.15 for 5-mm long BBO OPCPA stage pumped at 532-nm. The pump intensity used for the simulation is $\sim$10 GW/cm^2. The simulation shows the case of fixed non-collinear angle ($\alpha \sim 2.264°$) with variation of the phase-matching angle in (a) and the case of fixed phase matching angle ($\Theta \sim 23.8°$) with

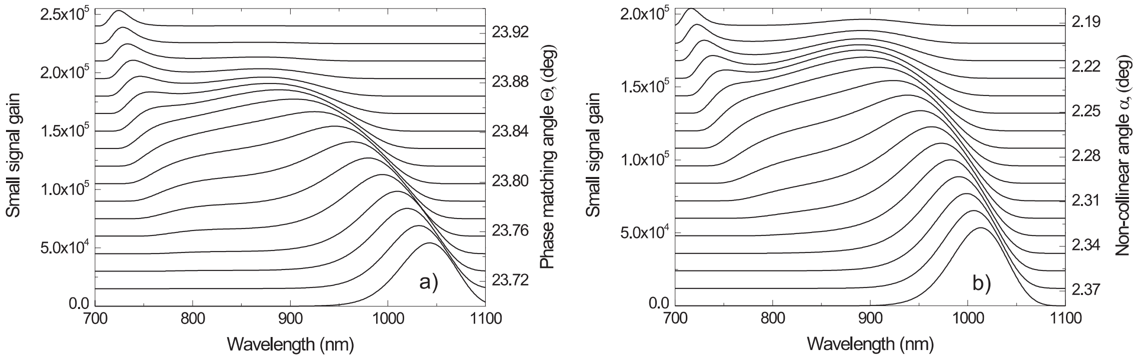

Figure 2.15: Amplified parametric bandwidth for 5-mm long BBO OPCPA stage pumped at 532-nm. (a) Fixed non-collinear angle α and variable phase matching angle Θ; (b) Fixed phase matching angle Θ and variable non-collinear angle α.

variable non-collinear angle in (b). A small phase matching angle variation or variation of the non-collinear angle is sufficient to strongly modify the amplified parametric bandwidth. Simulation has been performed to quantize the degree of sensitivity to angle variation for a BBO crystal. The simulation results are shown in figures 2.16 for a 5-mm long BBO OPCPA pumped at 532-nm. The main figure shows the dependance of the Fourier-limited pulse duration supported by the amplified parametric bandwidth. The calculations are obtained solving the coupled wave equations for a plane wave and using the slowly varying envelope approximation for variable values of phase matching and non-collinear angles. The grid step for the simulations with BBO crystal are 0.21 mrad for the phase matching angle and 0.27 mrad for the non-collinear angle. The zero value on the axis are $\Theta = 23.8°$ for the phase matching angle and $\alpha = 2.264°$ for the non-collinear angle. The white colored points on the mesh represent points of phase matching for an average amplification value larger than 78% of the maximum amplification and Fourier-limited pulse duration value smaller than 84% of the highest amplified bandwidth. The pulse duration values are given at FWHM. The point with the largest average amplification is shown in the left-side inlet of Fig. 2.16 for BBO (7.6-fs Fourier-TL-pulse duration) crystal. This is an ideal operation point for an OPCPA stage and is also used in the OPCPA described in the Thesis. Another example for phase matching is shown in the right inlet of Fig. 2.16. This amplified parametric bandwidth is obtained by large angular detuning (BBO: 7.2-fs TL-pulse duration). Angular detuning is a method for the enhancement of the parametric bandwidth. Detailed description is given in section 2.2.6.

From these simulation follows that the non-collinear angle can only be varied within $\Delta\alpha$ ~0.8 mrad and the phase matching angle even in smaller range of $\Delta\Theta$ ~0.63 mrad without exceeding the white marked area of maximum parametric gain and bandwidth in Fig. 2.16. Sensitiveness to angle variation strongly depends on the crystal in use. A crystal with higher angular acceptance must be used, to reduce the angular sensitivity of the amplifier system. One suitable candidate is LBO, which has better angular acceptance compared to BBO.

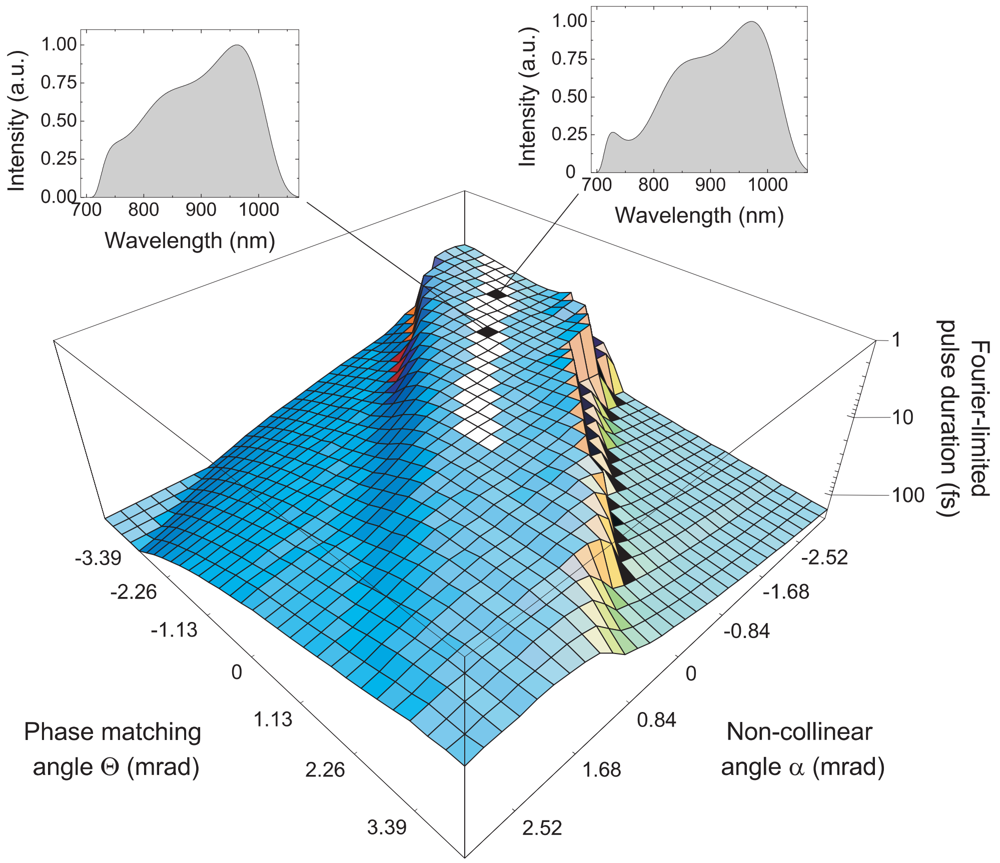

Figure 2.16: Angle sensitivity for 5-mm long BBO OPCPA. Parametric bandwidth sensitivity on angle variation (phase matching angle and non-collinear angle); inlets: (left) point of maximum average gain; (right) parametric bandwidth for large angular detuning; Θ at 0-position is 23.8 and α at 0-position is 2.264.

Chapter 3

The amplifier system

3.1 Ti:Sapphire oscillator front-end

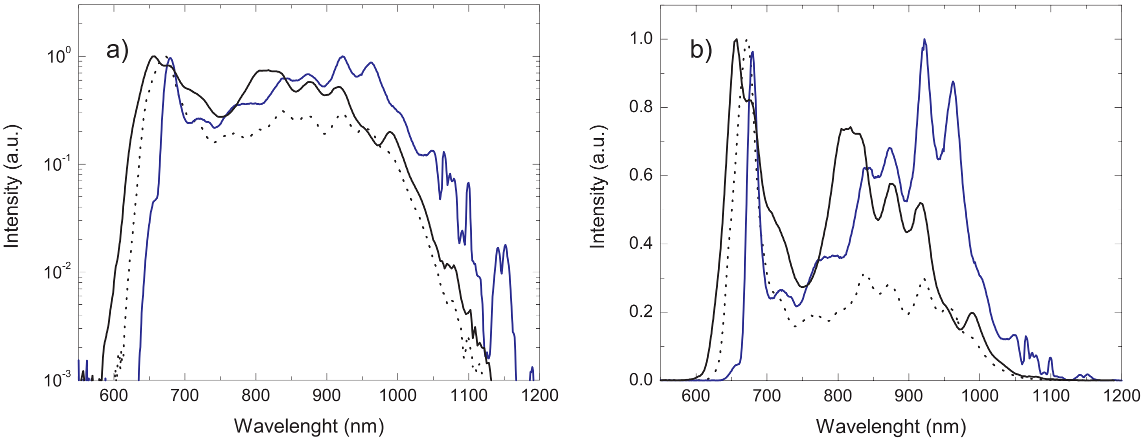

Figure 3.1: (a) Ti:Sapphire oscillator spectra with BRBOTK cavity-mirrors (black line), with CM4 and CM5 mirrors (dotted line) and with BRBOTK cavity-mirrors combined with a new output coupler (blue line); (b) Same spectra as in (a) in linear scale.

A key component of our system is the broadband Ti:Sapphire oscillator [122–125] based on Kerr-lens modelocking [126]. The central wavelength λ_c of the oscillator is ∼850 nm. Its spectrum covers a spectral range of ∼450 nm (1/e^2 bandwidth) and it has an output energy of 4 nJ at 79 MHz repetition rate. We tested several chirped mirror and output coupler sets to find an optimum in output energy and bandwidth. The oscillator spectrum which is shown in Fig. 3.1(a and b, black curves), supports a Fourier-transform-limited pulse duration of 4.5 fs at FWHM. The dotted line in Fig. 3.1(a,b) is the oscillator spectrum obtained with an older set of chirped mirrors the CM4, CM5. The spectra shown in Fig. 3.1(a,b) (black and blue curves) are obtained with BRBO-TK cavity mirrors. The blue line in Fig. 3.1(a,b) is the spectrum obtained with BRBO-TK mirrors and a new broadband output coupler with 10% outcoupling efficiency. The output coupler is coated

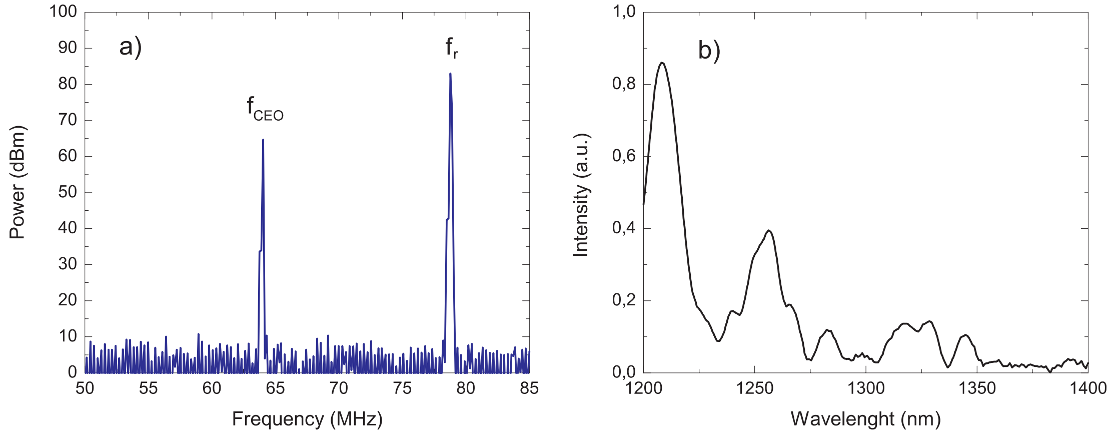

Figure 3.2: (a) Repetition rate and beat-signal between the fundamental and DFG-signal from the oscillator; (b) spectral edge extended in the infrared region through self-phase-modulation in a PP:LN crystal, used for f-to-0 CEO-stabilization.

to support spectral components in the infrared region towards 1.1 μm. The benefit would be higher energy in the spectral region of Nd:YAG for direct optical seeding [127].

There are important properties, intrinsic to Ti:Sapphire oscillators, which should be mentioned at this point, if used for seeding broadband OPCPA. The output beam has a frequency dependent divergence and mode size differing in the sagittal and in the tangential planes (see Fig. 3.3) [134]. Another property of Ti:sapphire oscillators is the multi-pulsing operation near zero-nett internal dispersion [135]. The double and triple pulsing has a separation of only a few ps from the main pulse and is difficult to detect. Such phenomenon can be observed only after the amplification of these pulses and temporal contrast measurement as small satellites in the ps-region.

We tested the possibility to stabilize the carrier-envelope-phase (CEP) offset of the oscillator [128–130]. The scheme in use was proposed by T. Fuji *et al.* [132, 133] and consists in tightly focus few-cycle pulses from a Ti:sapphire oscillator into a highly nonlinear magnesium-oxide-doped periodically poled lithium niobate (PP-MgO:LN) crystal to induce self-phase modulation (SPM) and difference frequency generation (DFG; 4-mm long PP:LN crystal). Due to the enhanced nonlinear interaction and an improved spatial overlap between the fundamental and the DFG wave (due to the absence of walk-off effects), the interferometric beat signal emerging at f_{CEO} in the region of spectral overlap is strong enough (65 dB) for reliable CEO-locking over several hours (Fig. 3.2(a)). Figure 3.2(b) shows the infrared-part of the oscillator spectrum after the PP-LN for the beat signal optimization (4 bounces on -50 fs^2 chirped mirrors). The intracavity dispersion is close to zero, in order to obtain the largest possible bandwidth from the oscillator. The 4 bounces on the negative dispersion chirped mirrors corresponds to the output coupler dispersion and to the dispersion of 2 mm of PP:LN-crystal. This way, the shortest pulses are obtained at the center of the crystal, to maximize the nonlinear effects.

The challenges for phase-stabilization in OPCPA are manifold. In principle, OPCPA

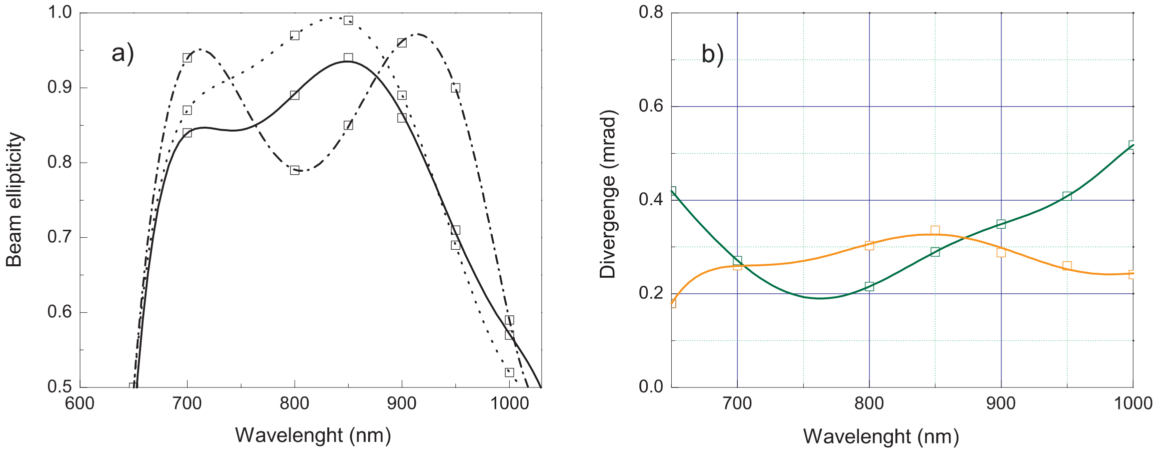

Figure 3.3: (a) Frequency-dependent beam ellipticity of the broadband Ti:sapphire oscillator. Spatial mode ellipticity after 1 m (solid) propagation, 3.8 m (dotted) and 6.7 m (dot-dashed); (b) Frequency-dependent beam divergence in the sagittal (orange) and in the tangential (green) plane.

has proven to maintain the CE-offset for a single stage OPA with μJ-level pulse energy at 1kHz repetition rate [131]. The present OPCPA consists of several amplification stages working at 10 Hz repetition rate. Even by using a f-to-2f spectral interferometer which is insensitive to pulse energy fluctuation to a certain extend, the output energy stability exceeds a level where a reliable carrier envelope phase measurement can be performed. Pulse energy fluctuation has to be minimized, in order to CEP-stabilize a multistage OPCPA. Another way is to monitor the absolute carrier-envelope-phase with a single-shot device and apply a selection procedure on the output pulses.

3.2 Ti:Sapphire amplifier front-end

A high temporal pulse contrast exceeding 7 orders of magnitude is required for many high-field physics experiments, such as high-harmonic generation from solid-density plasmas to avoid pre-plasma formation. The OPCPA version with Ti:sapphire oscillator front-end has restrictions due to the low-energy seed pulses. A Ti:sapphire multipass amplifier is used, (Femtopower from Femtolasers GmbH, Fig. 3.4(c)) to counteract this problem. The Femtopower can deliver about 1.2 mJ pulse energy at 1 kHz repetition rate with a spectral bandwidth of 55 nm at FWHM (@800 nm, see Fig. 3.4(a), blue line). The temporal contrast of the output pulses is characterized by third order autocorrelation. The measurement is shown in Fig. 3.5(b). The pulse front is clean of prepulses and have a contrast reaching almost 9 orders of magnitude from the pulse peak to the ASE pedestal. The compressed output pulses have a duration of 23.5 fs at FWHM (Fig. 3.4(b)) and these are send through a hollow-core fiber filled with Neon gas (250 μm core diameter), for spectral broadening [136]. The output energy from the hollow-core fiber is about 400 μJ.

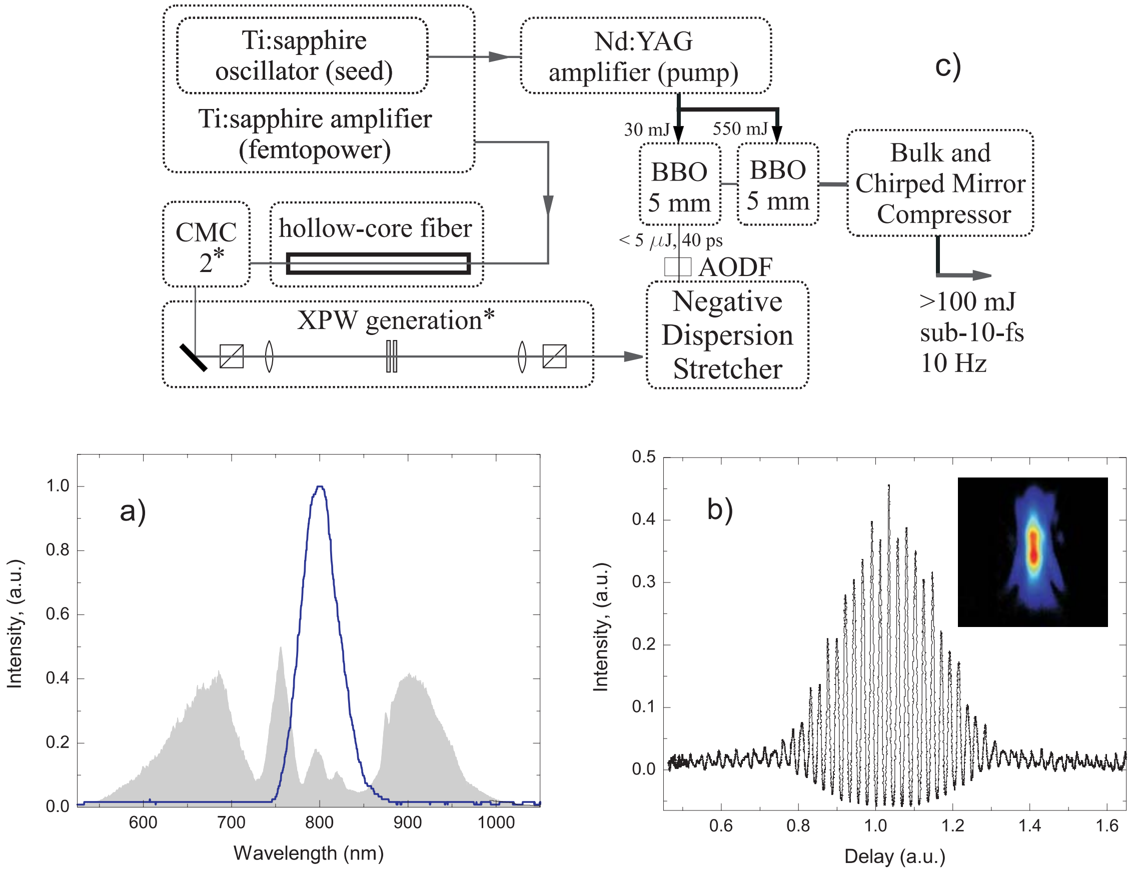
Ti:sapphire oscillator (seed)
Ti:sapphire amplifier (femtopower)
Nd:YAG amplifier (pump)
c)
30 mJ
550 mJ
BBO 5 mm
BBO 5 mm
Bulk and Chirped Mirror Compressor
CMC 2*
hollow-core fiber
< 5 μJ, 40 ps
AODF
Negative Dispersion Stretcher
XPW generation*
>100 mJ
sub-10-fs
10 Hz
a)
Intensity, (a.u.)
Wavelength (nm)
600
700
800
900
1000
0.0
0.2
0.4
0.6
0.8
1.0
b)
Intensity, (a.u.)
Delay (a.u.)
0.6
0.8
1.0
1.2
1.4
1.6
0.0
0.1
0.2
0.3
0.4
0.5

Figure 3.4: (a) Spectrum of the amplified Ti:sapphire amplifier output pulses (blue), spectrum broadened in the hollow-core fiber (shaded grey); (b) Pulse duration measurement of the Ti:sapphire amplifier output by autocorrelation and by Grenouille (23.5 fs at FWHM, inlet); (c) Optical scheme of the OPCPA amplifier with Ti:sapphire front-end (* Cross-polarized wave generation XPW - optional)

The requirements for the spectrum are uniform shape and spectral components in the gain region of BBO which lies approximately between 720 nm and 1.035 μm for a 5-mm long BBO. The spectral broadening is very effective in the blue spectral wing but difficult towards shorter wavelengths. The neutral gas (neon) is ionized very rapidly due to the high laser intensity. The index of refraction is decreased due to the rising density of free electrons [137, 138]. The plasma is generated on the timescale of the pulse duration thus causing a blue-shift of the spectrum. The spectrum can be broadened from 600 nm to 1 μm (Fig. 3.4(a), shaded grey line) with increased neon gas-pressure of about 2.5 bar in the hollow fiber. Unfortunately, the mode of operation in this case is unstable in terms of energy fluctuation and spatial mode stability. A spectrum with an energy stability better than 1% and transverse TEM_{00} mode is obtained with 1.6 bar gas-pressure and a typical spectrum is shown in Fig. 3.5(a, shaded grey line) with spectral components as far as 950 nm towards longer wavelengths.

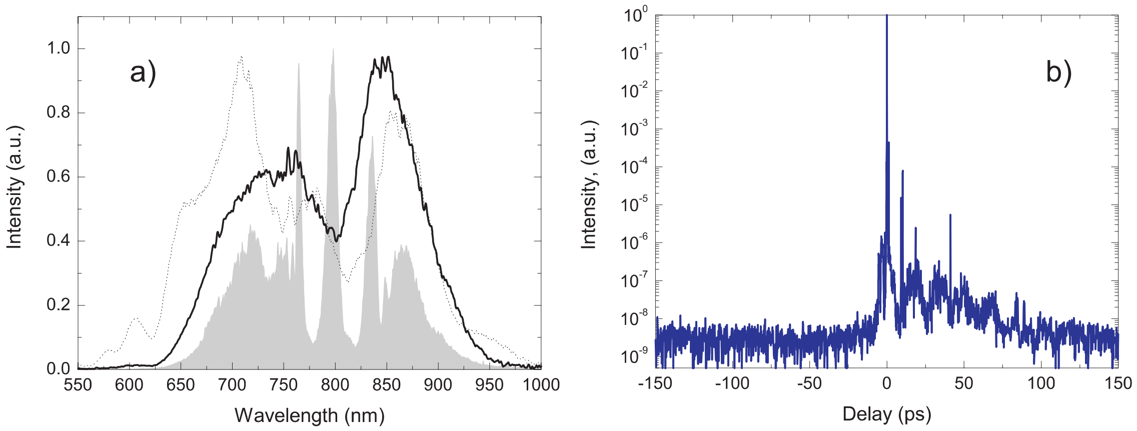

Figure 3.5: (a) Spectrum after hollow-core fiber broadening (shaded grey line), spectrum of the generated XPW-wave (black line) and XPW-wave spectrum for light intensity close to continuum generation in BaF_2 (dotted line); (b) third order autocorrelation spectrum of the Ti:sapphire amplifier output (blue line).

Cross-polarized wave (XPW) generation can be used to clean the temporal pulse contrast by several orders of magnitude, as well as to clean the spectrum from spectral modulations around the spectral region of the Ti:sapphire amplifier, caused by self-phase modulation effects in the hollow-core fiber [139–141]. The scheme is tested in order to estimate the conversion efficiency and the quality of the XPW output in terms of energy stability. We use a double crystal scheme with 1-mm BaF_2 cut at [100] orientation. The first crystal is placed in the focus, the second one is placed right after the first crystal. The beam is refocused into the second crystal due to self-focusing effect stemming from the first BaF_2 crystal. The double crystal scheme is used to optimize the conversion efficiency of the XPW-process, which can in theory reach values around 20%. Only about 10% of the 400 μJ pulses from the hollow-core fiber output are used to generate the XPW-wave because of the required optimum intensity in the focal spot which is about 2 TW/cm^2. A 1-m focal distance mirror is used to focus the beam down to a focal spot of w_0 ~100 μm. In order to reach the correct intensity in the focal region, only about 50 μJ pulses are required at given pulse duration of 7-fs. The spectrum of the hollow-core fiber output pulses is shown in Fig. 3.5(a, solid line) and the corresponding spatial beam profile is shown in Fig. 3.6(b). The beam goes through a Rochon-polarizer to enhance the linear polarization quality with an extinction ratio of 5 orders of magnitude. The fundamental and the XPW-wave are separated by a Rochon-analyzer, after the wave interaction in the BaF_2 crystal. The temporal contrast of the generated XPW-pulses can be estimated using a formula given by Jullien *et al.* [141],

$$C_{out} = C_{in}^3 \frac{1 + \frac{KR}{c_{in}^2 \eta_{eff}}}{1 + \frac{KR}{\eta_{eff}}}. \tag{3.1}$$

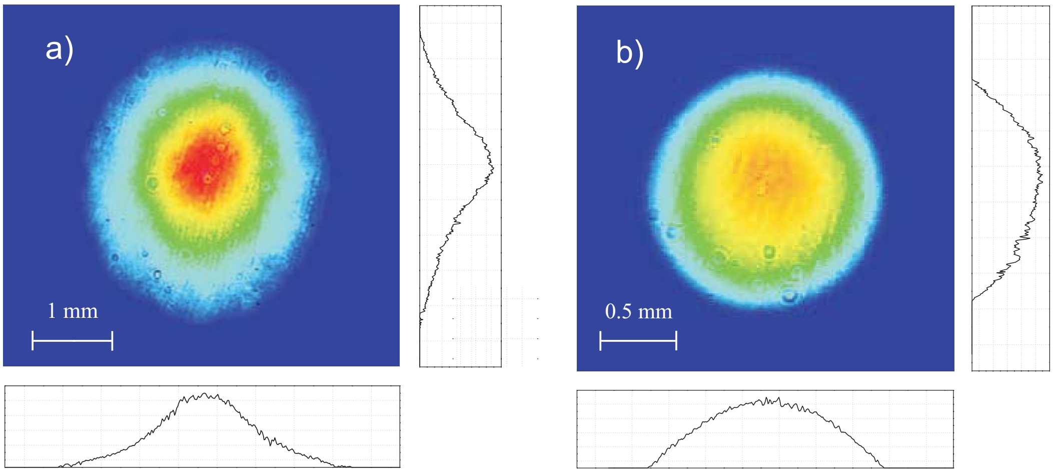

Figure 3.6: (a) Spatial beam profile after the hollow-core fiber; (b) Spatial beam profile of the generated cross-polarized wave.

C_{out} is the temporal contrast of the generated XPW-pulses and C_{in} is the contrast of the input pulses. K is the factor, where the peak efficiency starts to drop, due to the cubic proportionality of the effective conversion efficiency temporal and spatial intensity distributions of the input beam. In the case of gaussian distributions in the non-depleted regime it is around ∼0.18. $R = 10^{-5}$ is the extinction ratio of the Rochon-polarizer/analyzer and $\eta_{eff} = 16\%$ is the effective conversion efficiency. The XPW-process yields a cleaning effect of 5 order of magnitude, which is mainly set by the extinction ratio of the polarizer-analyzer pair. The XPW-signal conversion efficiency is 16% with a pulse energy of $\sim 8\mu$J. The spatial beam profile of the generated XPW-wave is shown in Fig. 3.6(b) and its spectrum is shown in Fig. 3.5(a, solid black line) for optimum intensity in the focal region and 3.5(a, dotted line) for higher intensity. The spatial and particularly the spectral cleaning effect is remarkable. The sharp features in the central part of the hollow-core fiber output spectrum are completely eliminated. The beam obtained by this contrast cleaning technique is ideal to seed an OPCPA and the implementation is simple. However, the hollow-core fiber output is used to seed the OPCPA directly for the first implementation round. The Ti:sapphire amplifier provides an excellent temporal contrast which can be used for first experiments. As already mentioned, saturation in the last OPCPA stage might moderately degrade the temporal contrast.

3.3 The pump

The pump source is one of the bottlenecks in high energy OPCPA development. Several aspects has to be considered for an OPCPA pump. A high energy pump is required with an excellent shot-to-shot energy stability, as the parametric process is very sensitive to pump energy fluctuations. The spatial beam profile should be uniform to ensure a uniform intensity distribution of the amplified signal beam profile. The pump pulse duration has to be matched to the stretched seed pulse duration, as discussed in Sect. 2.2.3, to gain a maximum pump-to-signal conversion efficiency, which can reach values <30% in OPCPA. On the other hand, in order to use higher pump fluence in the parametric amplification process, a longer pulse duration is required to avoid working near the damage threshold of optical AR-coatings and materials (~20 GW/cm^2 for AR coatings). However, the stretching ratio of the seed pulses is a restriction due to the difficult pulse compression and due to the required intensity for parametric amplification. The choice of pump pulse duration is then a trade-off between reasonable stretching ratio of the seed pulses and damage threshold of optical materials and coatings. A final requirement is the synchronization scheme between pump and seed pulses to have jitter-less temporal overlap in the OPCPA crystal. To this end we resorted to an optical seeding scheme to reach a better stability than with electronic locking schemes. The stability of electronic pulse synchronization is in the sub-ps to ps range. Soliton-based optical seeding can reach a stability, which is mainly limited by the timing jitter, induced by variation of the soliton wavelength shifts. This variation in wavelength is caused by energy fluctuation of the Ti:sapphire oscillator pulses [142]. The Ti:sapphire oscillator has an energy stability better than 0.3% and the timing jitter is estimated to be better than 30 fs.

3.3.1 Optical seeding

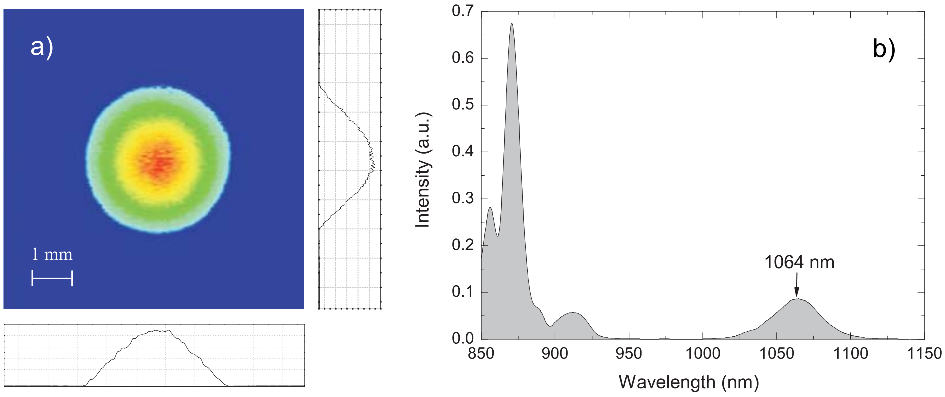

Figure 3.7: Soliton Raman-shift in the Photonic crystal fiber; (a) spatial beam profile of the Raman-shifted soliton (seed for the pump amplifier); (b) soliton spectrum

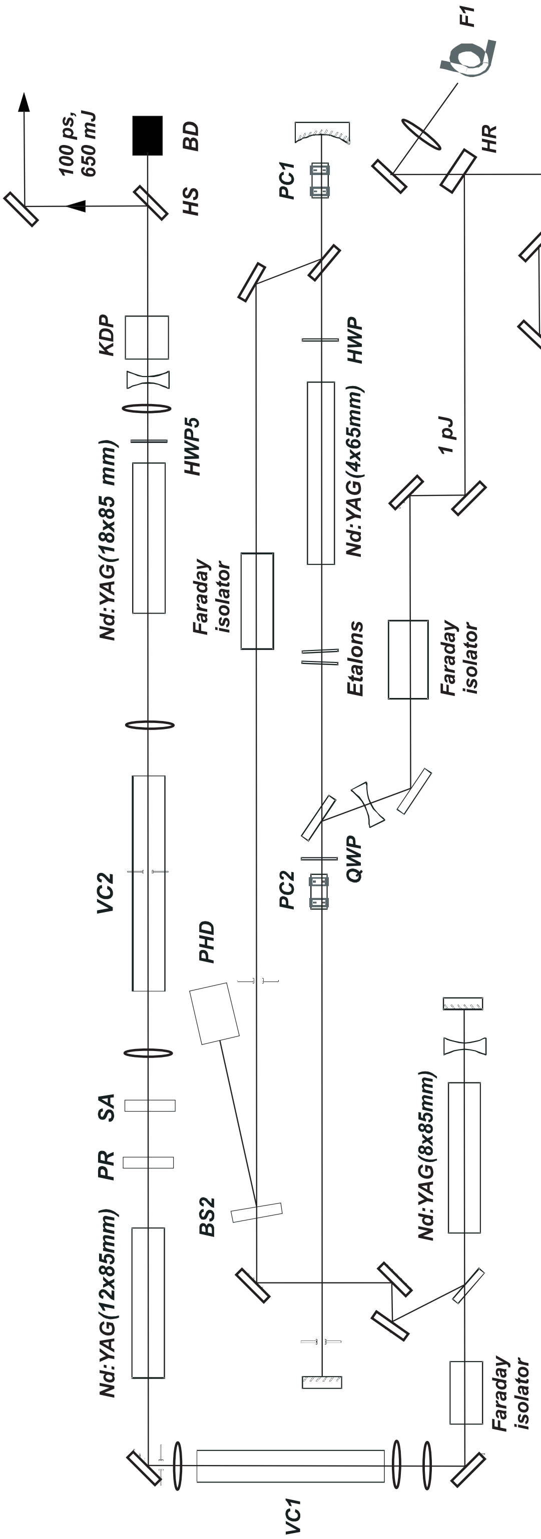
F1
HR
100 ps,
650 mJ
BD
HS
PC1
PCF
KDP
HWP
CM1
BF
BS
1 pJ
Ti:Sapphire
4.5 fs, 4.1 nJ
600-1080 nm
HWP5
Nd:YAG(18x85 mm)
Nd:YAG(4x65mm)
Faraday
isolator
Etalons
Faraday
isolator
VC2
PC2
QWP
PHD
Nd:YAG(8x85mm)
SA
PR
BS2
Nd:YAG(12x85mm)
Faraday
isolator
VC1

Figure 3.8: Optical scheme of the Nd:YAG pump amplifier. BS...beam splitter, VC...vaccum cell, PR...polarization rotator, SA...serrated aperture, PHD...photodiode, F1...optical trigger, PC...Pockels-cell, QWP...quarter-waveplate, HWP...half-waveplate, PCF...photonic crystal fiber, CM...chirped mirror, BF...bandpass filter, HR...high reflector, HS...harmonic separator, BD...beam dump, KDP...frequency doubling crystal.

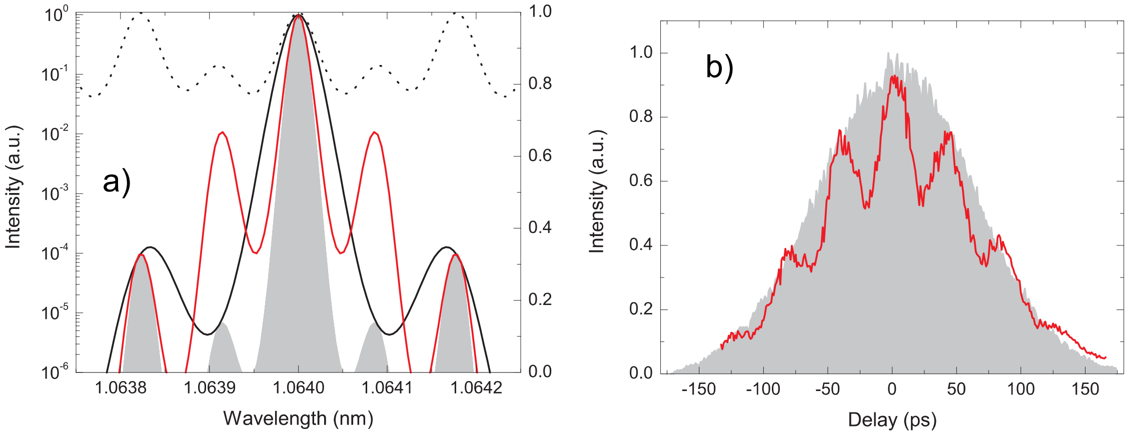

Figure 3.9: Calculated amplified spectrum for the regenerative Nd:YAG amplifier with intracavity etalon(s); (a) 2.1-mm etalon (black line); 4.1-mm etalon (red line); 2.1 and 4.1-mm etalon (shaded grey line); Etalon transmittance for the etalon combination of 2.1 and 4.1-mm (dotted line); (b) Autocorrelation trace with 2.1 and 4.1-mm intracavity etalon (black line); single 4.1-mm intracavity etalon (red line).

To simplify the overall OPCPA synchronization-scheme we investigated two possibilities of optical synchronization of the pump and seed pulses. Direct seeding from the femtosecond oscillator [127] is the simplest way but the energy content in the oscillator pulses around 1.064 μm is low. Another method is based on raman-shifted soliton synchronization from a photonic crystal fiber (PCF) [142–144]. The homemade ultrabroadband Ti:sapphire oscillator used (with 10% output coupler [122](Femtolasers GmbH)), has an energy output of 4 nJ, and 20 fJ of seeding energy in the spectral acceptance region of the Nd:YAG amplifier (∼1Å). We also used a specially designed, more broadband output coupler which has the same transmission value. With this output coupler the oscillator output energy was only 2.8 nJ but it could deliver around 145 fJ at 1.064μm. In both cases the seed energy turned out to be unsufficient for stable operation of the Nd:YAG regenerative amplifier free from excessive amplified spontaneous emission (ASE). The best result was obtained with the latter oscillator version, reaching a ratio between the main pulse and the ASE (ns-scale) of 1:10 after the last single-pass Nd:YAG amplifier stage. Therefore we resorted to the soliton-based synchronization. To this end we focused part (1.6 nJ) of the recompressed oscillator output into a end-sealed photonic crystal fiber (18-cm long, type NL-PM-750 from Crystal Fibre). Due to efficient soliton-based frequency shifting several pJ of seed energy is obtained for Nd:YAG amplifier seeding (see Fig. 3.7(b)). This energy is high enough for reliable operation of the regenerative amplifier. A high quality spatial beam profile is obtained, due to the single mode propagation, from the PCF which is shown in Fig. 3.7(a).

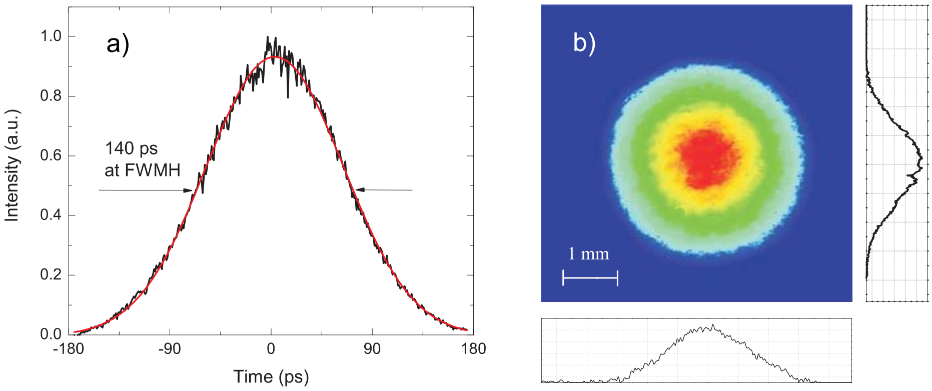

Figure 3.10: (a) Autocorrelation measurement (a) and spatial beam profile (b) of the amplified pulses from the regenerative amplifier.

3.3.2 Nd:YAG amplifier chain

The optical layout of the pump amplifier with optical seeding scheme is shown in Fig. 3.8. The seed pulses from the PCF are used to seed the regenerative amplifier, which consists of a 2 m cavity and a 4x65 mm flashlamp-pumped Nd:YAG rod as gain medium. We carefully adjusted the round-trip number (32) in the cavity and the regenerative amplifier gain, to reduce the amount of accumulated B-integral in the whole amplifier chain. The amplified pulse energy is 2 mJ, corresponding to 6 orders of magnitude gain. The duration of the amplified pulses is ~20 ps as a consequence of gain narrowing. The intracavity etalons are used for the fine tuning of the amplified pulse duration. A 2.1 mm and a 4.1 mm thick glass etalons inside the regenerative amplifier cavity reduce the seed bandwidth to obtain a pump pulse duration sufficiently long, to avoid excessive self-phase-modulation in the amplifiers chain. The etalons generate a narrow cumulative frequency transmission around the center frequency. The measured pump pulse duration set by this etalon pair is 100 ps. For the simulation of the intracavity etalon effect and its implications for the amplified pulse spectrum it is useful to start from the single-pass power gain formula [145]. The single-pass gain is given by

$$G(\omega) = exp(\frac{\omega L_g}{c}\chi''(\omega)). \tag{3.2}$$

The length of the Nd:YAG rod L_g is 65-mm and c is the light velocity in the gain medium (refractive index of Nd:YAG is given in Appendix A). $\chi''(\omega)$ is the nonlinear part of the susceptibility that has a Lorentian lineshape for Nd:YAG.

$$\chi''(\omega) = \frac{\chi_0''(\omega)}{1 + (\frac{2(\omega-\omega_a)}{\Delta\omega_a})^2}, \tag{3.3}$$

with center wavelength $\lambda_a = \frac{2\pi c_0}{\omega_a}$ =1.064 μm and a bandwidth $\Delta\omega_a$ of 150 GHz. The frequency dependent term $\chi''(\omega)$ appears in the exponent of Eq. 3.2. The exponential gain

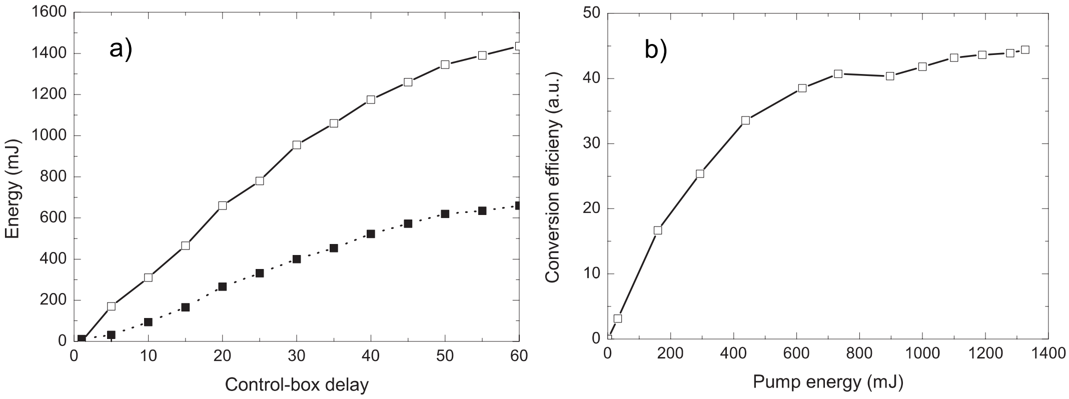

Figure 3.11: (a) Amplifier output energy (solid) and its second harmonic energy (dotted) dependance on the timing between flashlamp discharge and pulse arrival; (b) Conversion efficiency curve of the second harmonic generation.

causes a larger amplification for frequencies around ω_a and reduced amplification far from ω_a. This effect is known as gain narrowing.

The etalon transmission is calculated the same way as for a Fabry-Perot interferometer (a Fabry-Perot interferometer used as frequency-selective element in a cavity is referred to as etalon) [93].

$$I_t = I_0 \frac{1}{1 + (\frac{2F}{\pi})^2 \sin^2 (\frac{\pi\omega}{\Delta\omega_r})}, \tag{3.4}$$

with the Finesse parameter

$$F = \pi \frac{\sqrt{R}}{1 - R} \tag{3.5}$$

and the frequency gap between neighbouring resonant peaks

$$\Delta\omega_r = \frac{c_0 \pi}{nd \cos\Theta_{inc}}. \tag{3.6}$$

R is the reflectivity, n is the refractive index of the etalon material and Θ_{inc} is the inclination angle of the etalon which is set to 5°. This is necessary to avoid amplification of reflected pulses from the etalon surface. The thickness of the etalon d used for calculations is 2.1-mm and 4.1-mm. The etalon transmission for the etalon pair used in the regenerative amplifier is calculated by multiplying the transmission of the single etalon transmissions from Eq. 3.4, for 2.1-mm and for 4.1-mm (Fig. 3.9(a), dotted line). The simulation for the amplification and for the transmission through the etalons is performed times the number of round-trips in the regenerative amplifier. Results are shown in Fig. 3.9(a). The red curve shows the amplified spectrum with the 4.1-mm etalon in the cavity, the black curve represents the amplified spectrum with a 2.1-mm etalon in the cavity. The

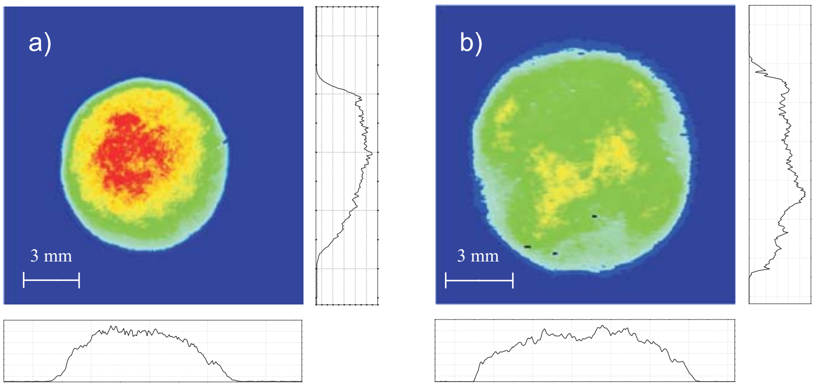

Figure 3.12: Spatial beam profiles of the generated second harmonic, unsaturated (a) and saturated (b).

periodic transmission of the single etalon causes a periodic modulation in the amplified spectrum which is equivalent to modulations in the time-domain. This can be observed from the measurements shown in Fig. 3.9(b). The red curve is an autocorrelation of the amplified pulse with a 4.1-mm intracavity etalon. The modulations in time are clearly visible, as well as the pulse broadening effect. The pulse duration which would rise only from gain narrowing is estimated to be around 20-ps. A combination of a thin and a thicker etalon is used to suppress the spectral modulations around the main peak, caused by each etalon separately. As can be seen from Fig. 3.9(a)-(shaded grey line), the FWHM of the peak at 1.064-μm is set by the thicker etalon. The thinner etalon is used to suppress the modulations around the 1.064-μm line. An autocorrelation trace of the amplified pulses for two intracavity etalons is shown in Fig. 3.9(b)-(shaded grey line). This autocorrelation trace is the same as in 3.10(a) and is shown again for comparison.

It is important to mention, that the pump pulse duration is easily tunable by changing the etalons thickness. The spatial beam profile of the regenerative amplifier output is shown in Fig. 3.10(b). The pump pulses from the regenerative amplifier are then amplified up to ~1.4 J in three flashlamp-pumped Nd:YAG amplifier rods of increasing diameter at 10 Hz repetition rate. The first amplifier is a double-pass 8x85 mm Nd:YAG amplifier which amplifies the regenerative amplifier output to 120 mJ with a total gain of 60. After spatial filtering and expansion, the beam is fed to a 12x85 mm single-pass Nd:YAG amplifier, which increases the pulse energy to 535 mJ (gain ~4.5). This power amplifier rod is overfilled by the seed beam to ensure high gain. Consequently, the amplified beam intensity distribution exhibits diffraction rings. For this reason, the beam is send through a serrated aperture to introduce higher frequencies in the outer part of the beam which is spatially cleaned in the subsequent spatial filter. After filtering and expansion, the beam is fed into the final amplifier based on a 18x85 mm single-pass Nd:YAG amplifier. The energy reached in this power amplifier is up to 1.42 J at 10 Hz repetition rate. The final amplifier rod is underfilled with seed, to preserve uniform intensity distribution, at the expense of lower single pass gain of 2.65.

The timing curve of the amplifier chain is shown in Fig. 3.11(a) (solid line). The OPCPA requires the second harmonic of the Nd:YAG wavelength for pumping. The output from the 18 mm amplifier is frequency-doubled in a 12-mm long Type-II D*KDP crystal reaching a maximal conversion efficiency of 45% (Fig. 3.11(b)), with 650 mJ pulses at 532 nm (Fig. 3.11(a), dotted line). The spatial beam profile can be fitted with an 8^{th} order supergaussian distribution and the pulses have a nearly Gaussian temporal profile. The amplified beam profiles are shown in Fig. 3.12, for the unsaturated (a) and for the saturated SH-generation (b). The ASE background is 5 orders of magnitude less intense than the ps pulse at 532 nm. The energy stability is 1.5% rms.

3.4 Pulse stretcher-Compressor

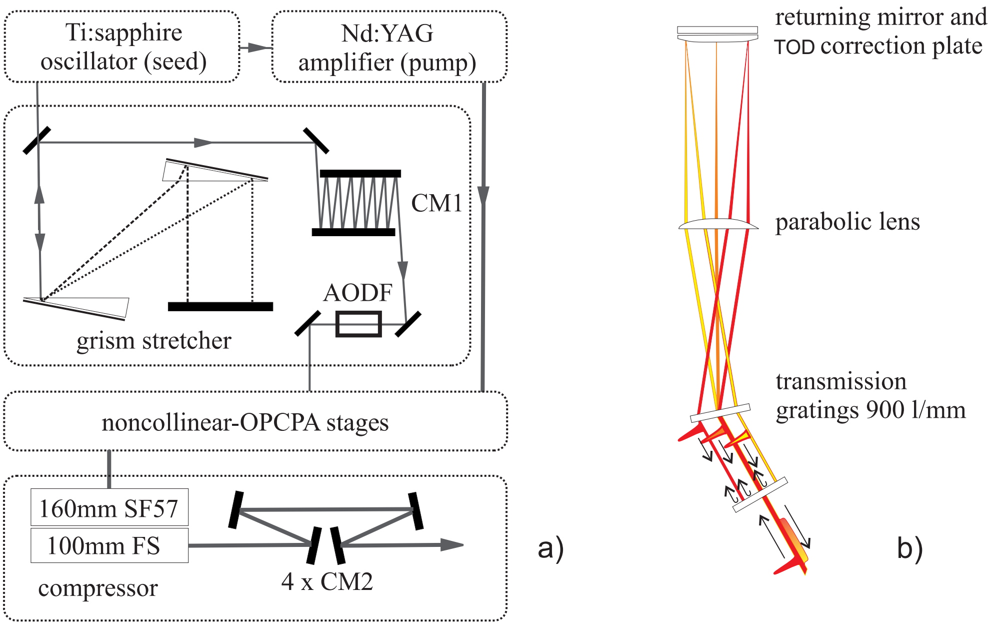
Ti:sapphire oscillator (seed)
Nd:YAG amplifier (pump)
CM1
AODF
grism stretcher
noncollinear-OPCPA stages
160mm SF57
100mm FS
compressor
4 x CM2
a)
returning mirror and TOD correction plate
parabolic lens
transmission gratings 900 l/mm
b)

Figure 3.13: Presently used pulse negative dispersion grism-stretcher with positive dispersion glass compressor (a). CM1...negative third order dispersion chirped mirrors; CM2...positive second order dispersion chirped mirrors; AODF...acoustooptical dispersive filter; (b) Previously used negative dispersion pulse stretcher.

Pulse stretcher and compressor are one of the most crucial components in chirped pulse amplifiers, especially for few-cycle pulse amplifiers. The physical dimensions of the stretcher turns out to be smaller, the larger the bandwidth. Additional higher dispersion orders has to be compensated for compression close to the Fourier-transform-limit due to the broad bandwidth.

The seed pulses are stretched to match the amplification window of the pump pulses. In our case we stretch pulses from a broadband Ti:Sapphire oscillator (TL-4.5 fs, Fig. 3.14(a), shaded grey line) to 50 ps. The effective pulse duration in front of the first OPCPA stage is approximately 40 ps due to partial pulse compression in the Dazzler material (45 mm long TeO_2). We use a compressor based on glass blocks (160 mm of SF57 and 100 mm of fused silica) and four bounces on positive dispersion chirped mirrors (100 fs^2 per bounce) for the final compression (Fig. 3.13(a)). The choice for a down-chirping stretcher-compressor was made to avoid losses in the compressor, which can be substantial ($\sim$50%) in a grating-based compressor for broadband pulses [34]. The glass compressor has high transmittance (>95%) and is additionally easy to align.

There exists several types of negative dispersion stretchers which are in principle suitable for dispersion compensation of a glass compressor. A combination of prisms and separate grating compressor [146] is one possibility, but difficult for bandwidths that sup-

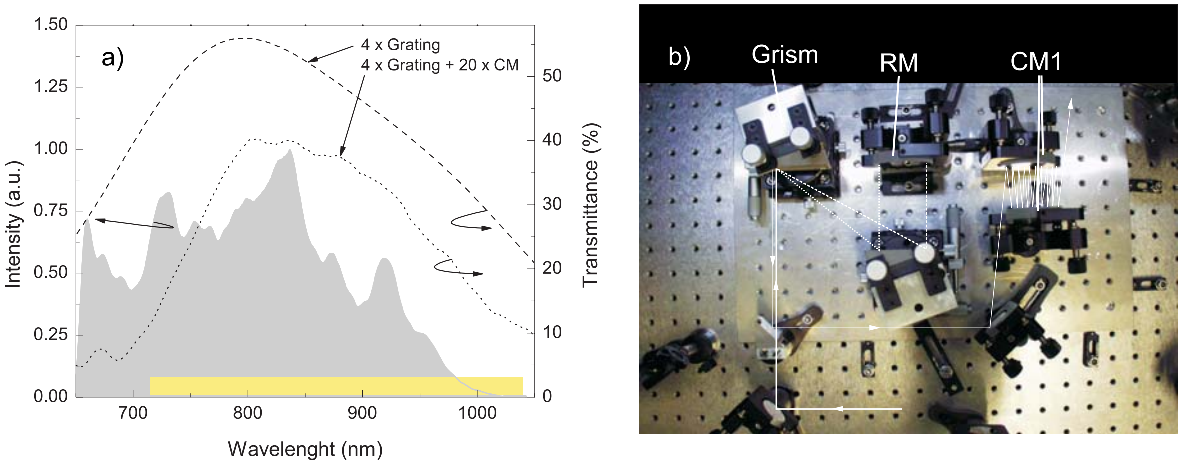

Figure 3.14: (a) Grism-stretcher transmission properties; transmitted spectrum (after stretcher, shaded grey line); transmittance of 4 x gratings (dashed line); transmittance of 4 x gratings and 20 bounces on chirped mirrors (dotted line); yellow bar: interesting bandwidth region for optical parametric amplification with 5-mm long BBO pumped at 532 nm. (b) Photograph of the grism stretcher; RM...returning mirror; CM...TOD-dispersion chirped mirrors

ports few-cycle pulses. Another possibility is a 4-f based stretcher with higher order correction plates in the Fourier-plane (Fig. 3.13(b)). We used this stretcher previously, but the stretcher is complicated in the alignment and the microfabricated correction plates introduce spectral modulation due to the frequency-dependent mode size of the broadband oscillator. In this four-pass, transmission grating-based stretcher the seed beam is dispersed by a 900 groves/mm transmission grating (Wasatch Photonics) and then collimated by a parabolic lens (f = 800 mm). A microfabricated fused silica plate is placed in Fourier plane, in front of the returning mirror . This plate is used for the higher-order spectral phase correction (mainly for 3^{rd}-order dispersion caused by the bulk compressor). All optical components of the stretcher are antireflection coated. The stretcher throughput is ~30% due to the limited acceptance bandwidth (675-1050 nm) and optical losses.

A more promising alternative is the grism-based stretcher [147] recently presented in a higher throughput version [148]. The grism stretcher is the most promising stretcher type to match the dispersion of glass for relatively large bandwidth as the second and third dispersion order can be controlled by the grism parameters, but higher order dispersion terms can be significantly tricky to compensate for bandwidths, supporting Fourier-limited pulse durations below ten femtoseconds. The grism stretcher is easy to align, it is versatile and compact (the separation of the grisms in our setup is 72 mm). Negligible residual spatial chirp could be detected by measuring the spectrum at different beam positions after the stretcher. The problem to solve was to adapt the grism stretcher for a bandwidth ranging from 700 nm to 1050 nm and to compensate dispersion of the glass compressor described before, plus 15 mm of BBO and the 45 mm TeO_2 of the acoustoptical dispersive

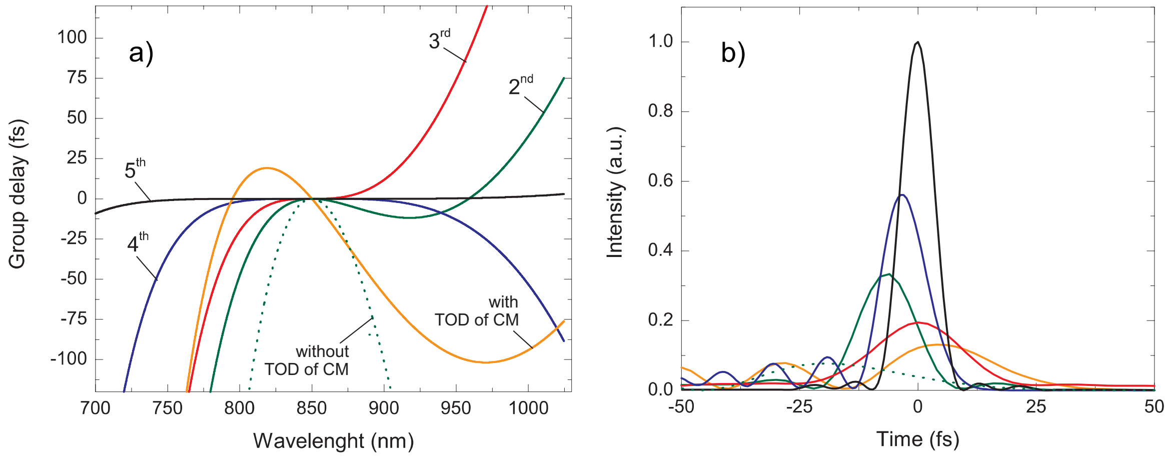

Figure 3.15: (a) Spectral dependance of the residual higher order dispersion (b) and its influence on pulse fidelity deterioration; TOD of CM...third order dispersion of the chirped mirrors

filter (Dazzler). The dispersion orders to be compensated for are 5.47E4 fs^2 GDD, 3.76E4 fs^3 TOD and 1.0E4 fs^4 FOD. Calculations show best results for low groove number gratings. We use 300 grooves per mm gratings ruled at 7.4° (Littrow angle for 860 nm) on a gold substrate (Richardson gratings, Spectra Physics). The SF11 prisms used in the setup have an apex angle of 18°. Both prisms are antireflection coated for 700-1100 nm. The amount of dispersion required to compensate over a 400 nm bandwidth do not allow to work at Littrow angle for highest throughput. The stretcher is operated near Littrow at ∼20°. The absolute efficiency of the grism stretcher with chirped mirrors is 21% for the entire bandwidth from 650 nm to 1050 nm. The stretcher design compensates for the largest part of second order dispersion (residual GDD is 400 fs^2). Residual fourth and fifth order dispersion are low, well in the correction range of the Dazzler, in the spectral range between 700 nm and 1100 nm. The residual third order dispersion is still too high to be compensated by the Dazzler only and is partially compensated by third order dispersion chirped mirrors. This can be observed in Fig. 3.15 for the pulse group delay without compensation of the second and third order dispersion, once with (solid green line) and without (dotted green line) third order dispersion chirped mirrors. The black line shows compensation till the fifth dispersion order for the entire stretcher and compressor. The residual dispersion has to be compensated by an acousto-optical dispersive filter (Dazzler, Fastlite) [149]. The stretching ratio is approximately four orders of magnitude high. Pulse stretching is tunable from 5 ps to 60 ps. 5 ps is the lower limit due to geometrical limitations, 60 ps is the upper limit due to the maximum of the residual higher orders that can be compensated by the Dazzler.

The spectral components of the transmitted spectrum above 1 μm are missing, compared to the transmitted spectrum of the old stretcher (4-f type). The losses are introduced by the Dazzler diffraction efficiency and by the grating diffraction efficiency in this spectral region.

The stretcher output beam is sent into the Dazzler for fine tuning of the spectral phase, as already mentioned before. The diffraction efficiency, with phase correction loaded, is ~10% resulting in output pulses with 10-20 pJ energy (oscillator front-end), which depends on the amount of dispersion to be compensated. The output of the Dazzler send to the OPCPA. The seed pulse duration of ~40 ps is chosen such that the pump intensity variation is negligible across the entire chirped seed pulse, which facilitates amplification of the whole seed bandwidth. A larger ratio between durations of the pump and seed pulses can be used to ease the synchronization. Consequently this will decrease signal amplification efficiency and will strongly enhance amplification of parametric superfluorescence, particularly if at least one OPCPA stage is operated close to the amplification saturation. The beam is expanded to a FWHM diameter of ~100 mm after the amplification and is sent through a compressor consisting of 160 mm long SF57 glass (Schott) and 100 mm long fused silica (FS, Heraeus). The aperture of the SF57 bulks is 120x120 mm and 150x150 mm for fused silica blocks. The optical quality of the fused silica blacks is $\lambda/10$ and in average better than λ for the SF57 glass blocks. The lack in optical surface quality is inherent to SF57 due to low Mosh hardness, thus complicating the polishing process.

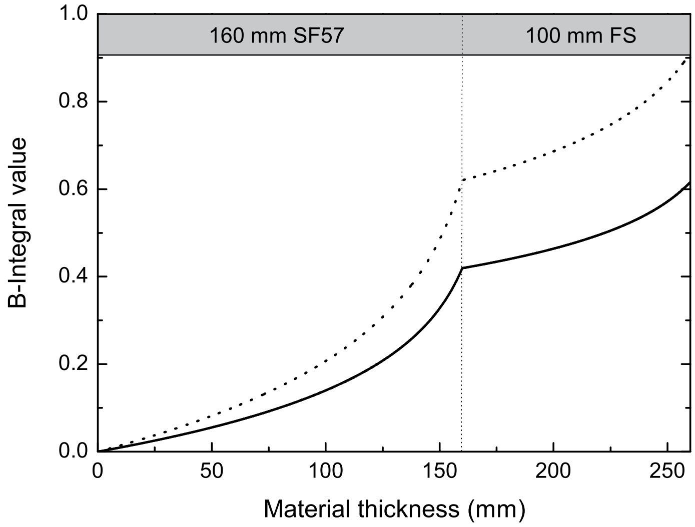

Figure 3.16: B-integral accumulation in the compressor material, for a 100 mJ pulses and 100 mm beam diameter (solid line), for a 250 mJ (after pump upgrade) pulses and 130 mm beam diameter (dotted line).

The beam is downcollimated to ~50 mm diameter after the bulk compressor. Pulse compression is finished using a set of four positive-dispersion chirped mirrors (~100 fs^2/bounce). Beam expansion and stepwise compression is used to reduce pulse self-action inside the bulk material. The B-integral value is estimated to be below 0.65 for the fully compressed pulse and 100 mJ pulse energy (Fig. 3.16, solid line). The B-integral is a mathematic integral (Eq. 3.7) to estimate the exponential growth of the least stable spatial frequency of the laser beam. The B-integral is numerically equal to the nonlinear phase shift along the optical axis of the laser system.

$$\mathrm{B} = \frac{2\pi}{\lambda} \int n_2 I(z) dz \tag{3.7}$$

A pump upgrade is planned for amplification to 250 mJ (30 TW, 8.5-fs). The compressor can be used with a beam diameter of 130 mm reaching a B-intergral value still below 1 (Fig. 3.16, dotted line). The spatial beam quality is important to mention at this point, because intense spots on the spatial beam profile can experience a value of B-Integral higher than the one given by calculations. Therefor, a homogeneous beam profile is essential. The total throughput of the pulse compressor is close to 95% which makes the concept of downchirped pulse amplification a promising alternative to grating-based compression (~50% efficiency with more than 300 nm bandwidth at 850 nm center wavelength).

3.4.1 Simulation of a grism stretcher with reflection gratings

The spectral phase for a grism stretcher is derived from raytracing calculations

$$\varphi(\omega, \Theta_{in}, \alpha_w) = 2[(l_3 + l_6)\frac{\omega}{c_0} + (l_1 + l_2 + l_4 + l_5) n_w \frac{\omega}{c_0} + R(\omega)]. \tag{3.8}$$

The ray path length in the grism stretcher is given by the distances $l_1 - l_6$, which are calculated by raytracing. Θ_{in} is the input incidence angle on the first prism, α_w is the apex angle of the prism-wedge. $R(\omega)$ is a correction term which takes into account the phase-shift stemming from different phase-matching along two points on the grating surface [150, 151]. It is given by

$$R(\omega) = -\frac{2\pi}{\mathrm{d}} x(\omega) = -\frac{2\pi}{\mathrm{d}} [((l_2 + l_4) \sin \xi_3 + l_3 \sin (\xi_5 - \alpha_w)] \tag{3.9}$$

d is the groove density of the grating. $x(\omega)$ is the distance between the perpendicular on the 2^{nd} grating (drawn from the point of incidence of the beam on the first grating) and the point of incidence of the wavelength-dependent beam on the 2^{nd} grating. The dispersion orders (GDD, TOD,...) are derived from the derivatives of the phase at the central angular frequency ω_0

$$\mathrm{D}_i \mid_{\omega_0} = \left. \frac{\partial^i \varphi(\omega, \Theta_{in}, \alpha_w)}{\partial \omega^i} \right|_{\omega_0}. \tag{3.10}$$

Estimation of the individual dispersion orders is a more convenient way to compare the dispersion of the grism stretcher with the dispersion of the combined glass and chirped mirror compressor.

The frequency dependent raytracing distances l_1-l_6 and angles of incidence ξ_1-ξ_5 are shown in Fig. 3.17. The angles ξ_1-ξ_5 between the light rays and the different grism boundaries can be calculated separately from the raytracing distances. From the rule of Snellius follows

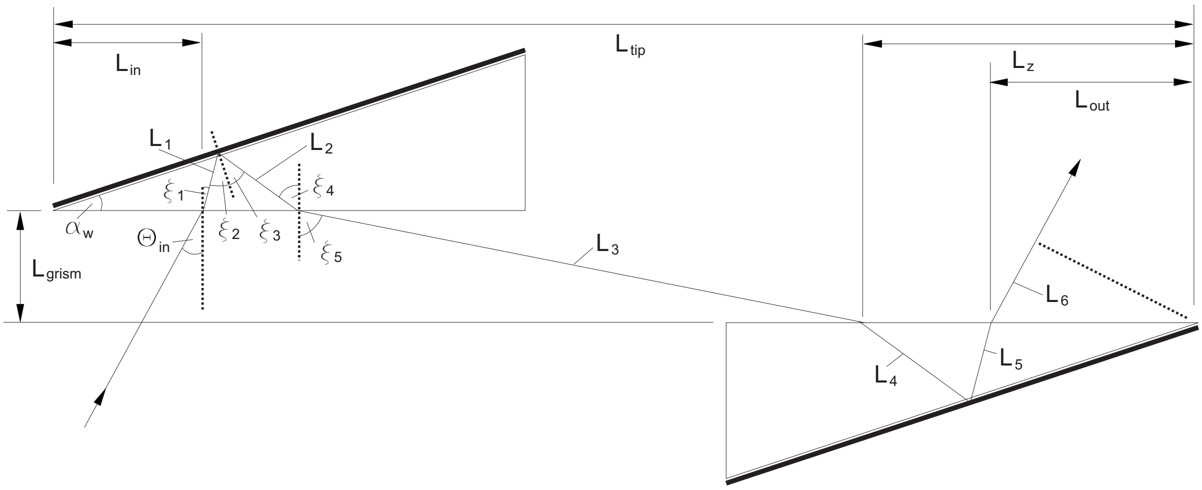

Figure 3.17: Raytracing of the grism stretcher with distances l and angles ξ. α_w...apex angle of the prism (wedge); l_{grism}...distance between the grisms.

$$\xi_1 = \arcsin \frac{\sin \Theta_{in}}{n_w}. \tag{3.11}$$

From the relationship between the angles in a triangle we obtain

$$\xi_2 = \alpha_w + \xi_1. \tag{3.12}$$

A simple expression for the angle ξ_3 can be found after a short derivation. The ray-path is depicted in Fig. 3.18.
Starting from

$$n_w \sin \xi_3 = \sin \xi_3' \tag{3.13}$$

and inserting the grating equation

$$\frac{m\lambda}{d} = \sin \alpha - \sin \beta, \tag{3.14}$$

we obtain

$$n_w \sin \xi_3 = -\frac{\lambda}{\mathrm{d}} + \sin \xi_2' = -\frac{\lambda}{\mathrm{d}} + n_w \sin \xi_2, \tag{3.15}$$

for first order diffraction. A simple relation between input angle ξ_2 and output angle ξ_3 follows in form of

$$\sin \xi_3 = \arcsin \left[-\frac{\lambda}{n_w \mathrm{d}} + \sin \xi_2\right]. \tag{3.16}$$

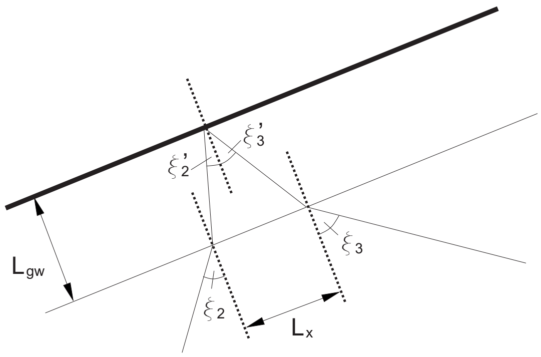

Figure 3.18: Raytracing at the boundary between prism and grating; l_{gw}...distance between prism (wedge) and the grating.

Furthermore, if $l_{gw} \ll l_{in}$ then l_x, shown in Fig. 3.18 can be assumed to be close to zero. ξ_4 is given by

$$90^\circ - \xi_1 + \xi_2 + \xi_3 + 90^\circ - \xi_4 = 180^\circ \quad \Rightarrow \quad \xi_4 = \xi_2 + \xi_3 - \xi_1 \tag{3.17}$$

and by applying Snell's law

$$\xi_5 = \arcsin{(n_w \sin \xi_4)}. \tag{3.18}$$

The derivation of the optical path of the rays l_1-l_6, follows from simple geometrical relations.

$$l_1 = l_{in} \frac{\sin \alpha_w}{\cos{(\alpha_w + \xi_1)}} \tag{3.19}$$

$$l_2 = l_1 \frac{\cos \xi_1}{\cos \xi_4} \tag{3.20}$$

$$l_3 = \frac{l_{grism}}{\cos \xi_5} \tag{3.21}$$

$$l_z = l_{tip} - l_1 \sin \xi_1 - l_2 \sin \xi_4 - l_3 \sin \xi_5 - l_{in} \tag{3.22}$$

$$l_4 = l_z \frac{\sin \alpha_w}{\cos \xi_3} \tag{3.23}$$

$$l_5 = l_4 \frac{\cos \xi_4}{\cos \xi_1} \tag{3.24}$$

$$l_{out} = l_5 \frac{\cos \xi_2}{\sin \alpha_w} \tag{3.25}$$

$$l_6 = l_{out} \sin \Theta_{in} \tag{3.26}$$

Usually the incident angle Θ_{in} is set to zero and the derived expressions are substantially simpler. As should be pointed out, the most important degrees of freedom for the dispersion modelling are the wedge angle α_w, the material of the wedge, the distance between the grisms l_{grism}, the tip-to-tip distance between the grisms l_{tip} and the groove number of the gratings. Clearly, the number of possible combinations is enormous and this is the main challenge calculating this type of stretcher.

3.5 OPCPA with Ti:Sapphire oscillator front-end

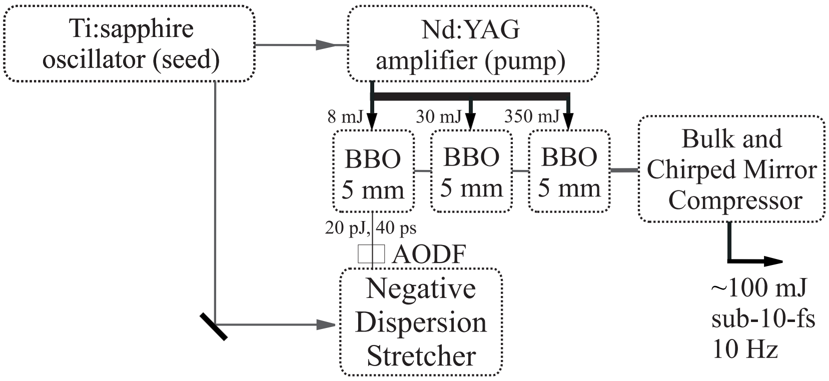
Ti:sapphire oscillator (seed)
Nd:YAG amplifier (pump)
8 mJ
30 mJ
350 mJ
BBO 5 mm
BBO 5 mm
BBO 5 mm
Bulk and Chirped Mirror Compressor
20 pJ, 40 ps
AODF
Negative Dispersion Stretcher
~100 mJ
sub-10-fs
10 Hz

Figure 3.19: Layout of the three stage optical parametric chirped pulse amplifier; AODF...acousto-optical dispersive filter.

The optical scheme for the amplifier is shown in Fig. 3.19. The pump, the second harmonic of a Nd:YAG amplifier (Sect. 3.3), is split into three beams, one for each OPCPA stage. The beam is relay-imaged from the SHG-crystal onto each BBO-crystal, in order the preserve a uniform beam profile, which is essential for parametric amplification. The beam size is adapted to reach the intensity required for the parametric amplification in steps, at the same time avoiding damage to optical coatings and materials. The beam profile outside the relay-image plane has hot-spots with higher intensity than the average beam intensity. This is an intrinsic feature of multi-mode pump beam propagation. This is the most frequent reason for optical damage to occur, in the present setup.

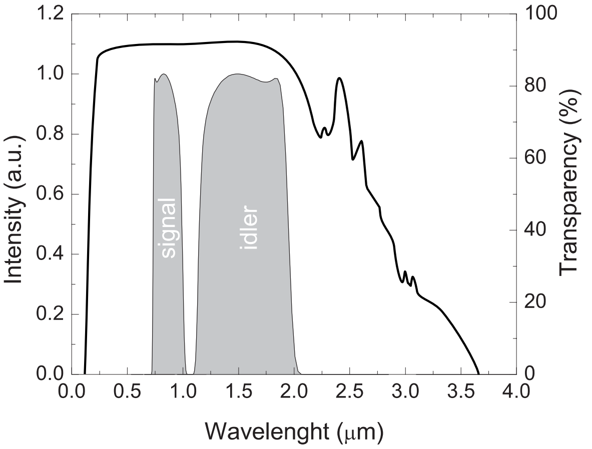

Figure 3.20: Comparison of the spectral ranges of signal and idler waves produced in the present OPCPA stage (shaded grey area) and transparency range of β-BBO (black line).

The pump energy for each OPCPA stage can be controlled independently using a $\lambda/2$ waveplate and a polarization-analyzer. The maximum available pump energy is 20 mJ in the first stage, 60 mJ in the second stage and 350 mJ in the third stage. The amplification in the OPCPA-chain begins with a 20 pJ seed pulse with 40 ps pulse duration.

Amplification takes place in three OPCPA stages with 5-mm-thick antireflection-coated BBO-crystals ($\theta = 24°$, $\phi = 90°$, type I phase matching) with a noncollinear angle of 2.3° in single-pass geometry. The gain bandwidth for the signal in a 5 mm BBO stage exceeds 300 nm bandwidth from 720 nm to 1.03 μm (Fig. 2.3). The corresponding amplified idler spectrum starts above degeneracy point from 1.1 μm and expands till 2.04 μm. The spectral region of signal and idler is shown in Fig. 3.20, together with the transmission curve of BBO.

The amplification efficiency of spectral components in the OPA-process is limited not only by phase matching for given crystal thickness and angular interaction geometry. The transmission of spectral components above 2 μm wavelength starts to degrade in BBO-crystal. The spectral band of the idler ends, were severe absorption range starts (3.20) and thus not used in this OPA scheme.

3.5.1 Energetics

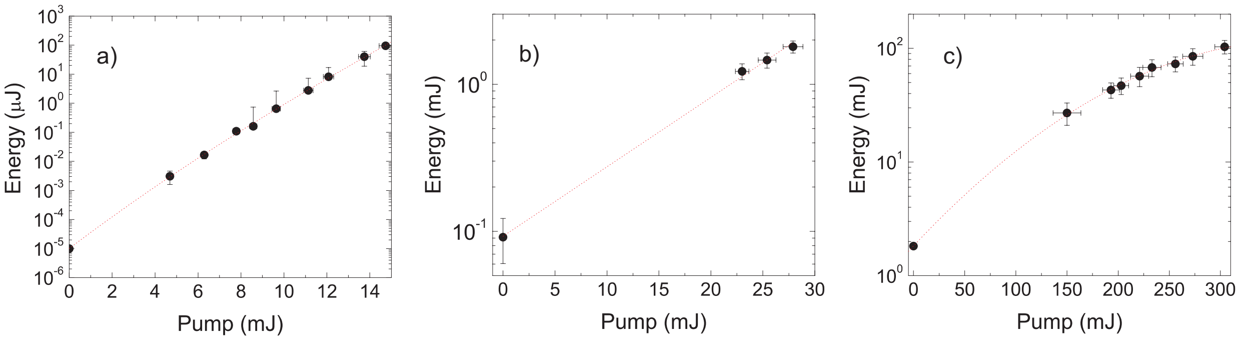

Figure 3.21: Dependencies of the amplified signal energy on the pump pulse energy in (a) the first; (b) second; (c) third stages. Measurement results are presented as black points with error bars and fitted curves as an eye guide (red dotted line).

The signal pulses are typically amplified to an energy level of ~100 μJ in the first stage (18.4 GW/cm^2 pump intensity), where an amplification efficiency of 0.6% relative to the pump energy is reached. The amplification efficiency in second stage is 6.4%. The signal pulses are amplified to ~2 mJ (7.4 GW/cm^2 pump intensity). The signal is further amplified to ~110 mJ in the third stage at 4.5 GW/cm^2 pump intensity and an amplification efficiency of 24% is reached. It has to be mentioned that 30 mJ of the 110 mJ signal is amplified optical parametric fluorescence which rises from the low seed energy and from the high pump intensities used in the first stage to achieve highest possible gain. Additional energy is transferred to the doubly internally reflected pulse which is also amplified in the last OPCPA stage. This lowers the pump-to-signal conversion efficiency to ~20%. A detailed theoretical investigation on this phenomenological amplification process is given in Sect. 2.4.2. The energetics of all three OPCPA stages are presented in Fig. 3.21. The first and second stage are operated in the linear amplification regime. The third stage starts to saturate at pump energy levels larger than 150 mJ. The point of signal back-conversion to the pump is still not reached at 300 mJ pump energy (Fig. 3.21(c)) but the saturation effect is clearly more pronounced. The energy of the amplified signal without detectable AOPF is 10 mJ. Total gain exceeding 10 orders of magnitude is obtained from three OPCPA stages.

3.5.2 Amplified signal spatial beam profile

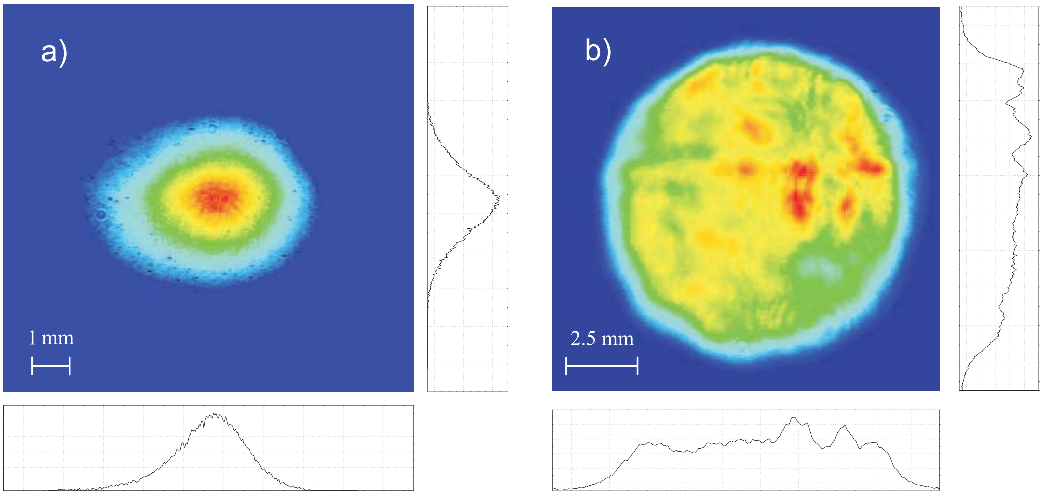

Figure 3.22: Spatial beam profiles of the seed beam in front of stage 2 (a) and amplified signal after third stage (with saturation, ~100 mJ)(b).

The spatial beam profile of the signal strongly depends on the intensity distribution of the pump amplifier. A typical intensity distribution of the pump beam is shown in Fig. 3.12. The seed beam has a smooth gaussian spatial profile with a wavelength dependent beam diameter (Fig. 3.22(a)). The spatial profile of the amplified signal after the first amplifier stage is still gaussian. This changes drastically after more than ten orders of magnitude gain in three OPCPA stages with the last stage in saturation (Fig. 3.22(b)). The spatial intensity distribution of the pump beam is then transferred to the amplified signal. Thermal-birefringence-induced depolarization in the amplifier chain [152–154] causes a nonuniform intensity distribution, which is minimized in the present setup. A slight different thermal lens in ordinary and extraordinary propagation direction combined with a polarizer in the beam-path causes typical conoscopic interference patterns in highly pumped laser amplifiers [155, 156]. Another effect which is more pronounced is onset of self-focusing in the regenerative amplifier, which can be identified in the center part of the amplified signal beam profile as an accumulation of more intense spots. A good spatial beam profile of the amplified signal can still be obtained, despite the sensitivity to pump beam imperfections

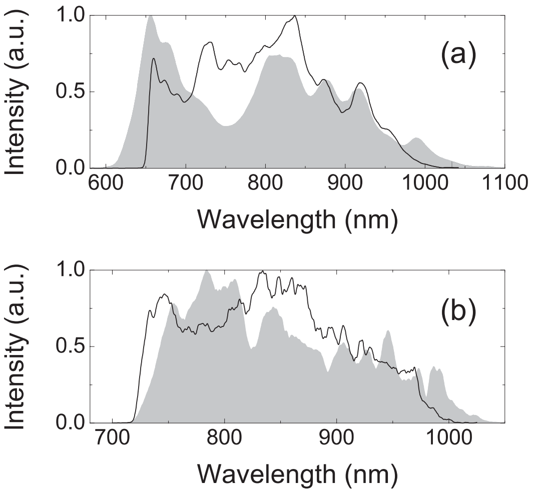

Figure 3.23: (a) Spectrum after the grism-stretcher (solid line), oscillator spectrum (shaded grey contour); (b) amplified spectrum of the grism stretched pulses (solid line, transform-limit 8 fs at FWHM), amplified spectrum of the stretched pulses from the 4-f based stretcher with correction lens (shaded grey contour, transform-limit 7.6 fs at FWHM).

which are small but present in our pump amplifier. The peak to average signal modulation which is obtained from the line-outs in Fig. 3.22(b) does not exceed 20%. Furthermore, negligible spatial chirp can be detected on the amplified signal beam only after the first stage of amplification which could eventually arise from the geometry of amplification. No spatial chirp is present on the saturated amplified beam after third stage.

3.5.3 Pulse compression

The pulse compression turned out to be difficult for several reasons. We could reach only partial compression with the previously used negative dispersion stretcher, due to the modulated spectrum (Fig. 3.23(b) shaded grey line) which made pulse measurements with SPIDER (spectral interferometer for direct electric field reconstruction) extremely difficult [157]. The fringes in the SPIDER trace on modulated parts of the spectrum are difficult to resolve. This causes often errors, for example spectral phase jumps, during the spectral phase retrieval. The SPIDER was constructed carefully to support the whole bandwidth of the OPCPA-system and was cross-checked with other temporal characterization devices. The cross-check was performed with autocorrelation and FROG measurements. At a later date, also with a single-shot GRENOUILLE.

Single shot SPIDER [161, 162] still remains the main diagnostic tool for the pulse duration measurement of the amplified signal (Fig. 3.24). A SPIDER offers the advantage to be rather insensitive to the spatial mode profile of the amplified signal compared to a FROG or a single shot GRENOUILLE device.

The optical pulse to be measured is first split into two parts (Fig. 3.24, BS1). One beam is send in a 10-cm long SF15 slab for frequency chirping, the other part is send

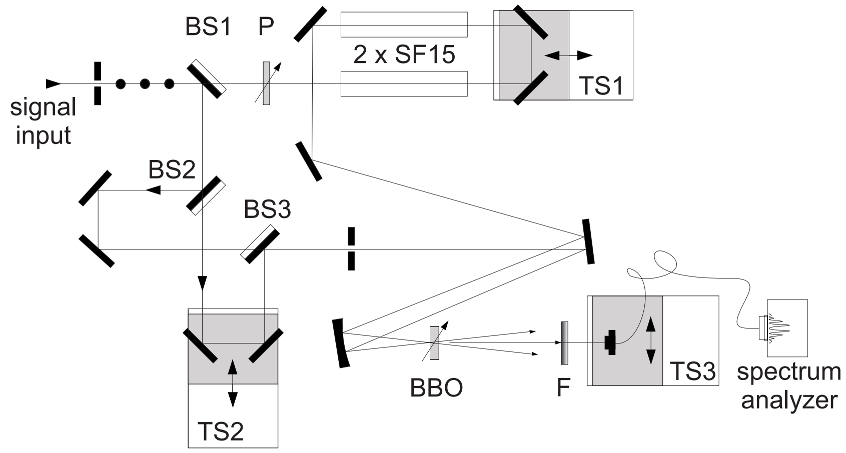

Figure 3.24: Optical layout of the SPIDER apparatus (courtesy of Y. Nomura). BS1...beamsplitter 50:50; BS2,BS3...thin beamsplitter for the Michelson-interferometer arm (d = 500 μm); P...polarizer (set at 120°); 2xSF15...2x50 mm of SF15 glass; TS1-TS3...translation stages; BBO...30 μm thick BBO crystal (orientation: SPIDER signal - 30°, SHG signal - 345°); F...Bandpass-filter for the SPIDER and SHG signal (~350-500 nm).

into a Michelson interferometer. The Michelson interferometer is used to generate two pulse replicas, which are time delayed in respect to each other. The time separation between the replica-pulses can be changed by tuning one interferometer arm. The two replicas from the interferometer are set to interfere in a spectrometer. The chirped pulse interacts with the replica-pulses in a nonlinear medium (Type-II BBO-crystal). Those replica-pulses are sheared by a monochromatic frequency of the chirped pulse during the nonlinear interaction, depending on the delay between the short pulses and the chirped pulse. The frequency shifted (Ω) fields will have a spectral shear between them. The electric fields of the temporally (with a delay τ) shifted replicas are $E_1(\omega)$ and $E_2(\omega)e^{-i\omega\tau}$ with $E_2(\omega) = E_1(\omega + \Omega)$. The spectrum obtained from the nonlinear interaction with the chirped pulse is given by $S(\omega) = |E_1(\omega) + E_2(\omega)e^{-i\omega\tau}|^2$. This term can be evaluated as

$$S(\omega) = |E_1(\omega)|^2+|E_2(\omega)|^2+|E_1(\omega)||E_2(\omega)|e^{i[\varphi_1(\omega)-\varphi_2(\omega)+\omega\tau]}+|E_1(\omega)||E_2(\omega)|e^{-i[\varphi_1(\omega)-\varphi_2(\omega)+\omega\tau]}, \tag{3.27}$$

with τ as the average period of modulation in the interferogram. The inverse Fourier-transform of the interferogram has components at $-\tau$, 0 and $+\tau$. Filtering of the components at $+\tau$, shifting to 0 and Fourier-transformation yields a signal

$$|E_1(\omega)||E_2(\omega)|e^{-i[\varphi_1(\omega)-\varphi_2(\omega)+\omega\tau]}. \tag{3.28}$$

The spectral phase difference $\phi(\omega) = \varphi_1(\omega) - \varphi_2(\omega)$ between the two interfering replica-pulses can be retrieved from this expression using reconstruction by integration or concatenation techniques [158–160].

The SPIDER apparatus was upgraded to single-shot mode [161, 162]. The single-shot option is introduced to facilitate the compression since the OPCPA operates at 10 Hz repetition rate [163–165]. The dispersion for the signal pulse can be changed online with the Dazzler making the pulse compression fast and reliable.

A grism-type-stretcher was developed at the same time to avoid spectral modulation and thus facilitate the SPIDER measurement. The grism-stretcher now in use does not introduce spectral modulations. This makes pulse duration measurements and thus compression easier and more reliable. The spectrum transmitted by the grism-stretcher is shown in Fig. 3.23(a, solid line). The pulse spectrum in front of the stretcher is shown as a shaded grey contour. It is evident that the grism stretcher cuts out the spectral components longer than 1 μm, mainly due to the much lower diffraction efficiency of the gratings in this spectral region. Therefor, these components are missing in the amplified spectrum (Fig. 3.23(b) solid line). The Fourier-transform-limited pulse duration of this spectrum is 8 fs. The fine structure of the spectrum is attributed to the high level of superfluorescence (approximately 30 mJ out of the amplified 110 mJ).

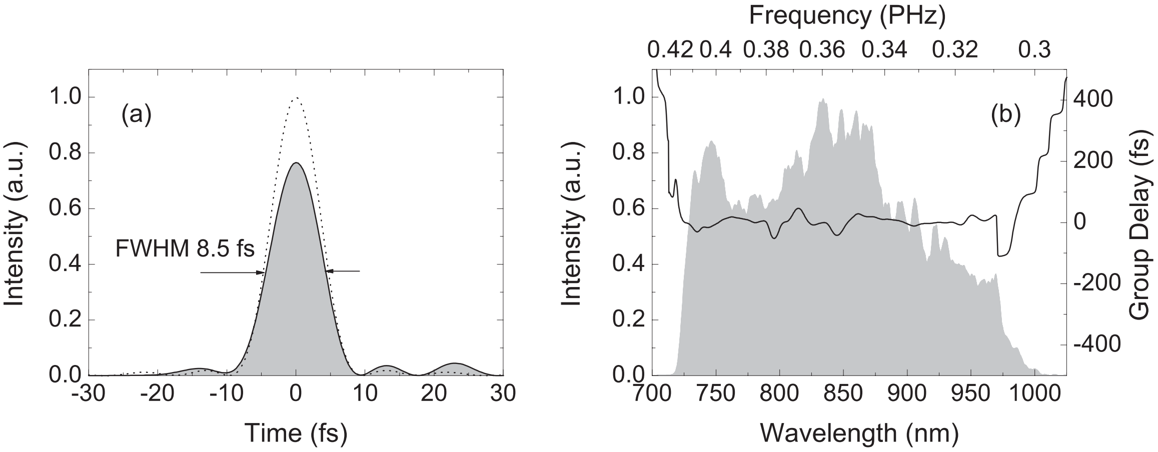

Figure 3.25: Compressed amplified signal pulse: (a) recompressed 80 mJ pulse. The dotted curve corresponds to the intensity profile of the transform-limited pulse (FWHM= 8 fs) calculated from the amplified spectrum. Retrieved amplified pulse spectrum (shaded contour) and group delay (solid line, b).

Figure 3.25(b) shows the retrieved spectrum and spectral phase, Fig. 3.25(a) shows the reconstructed intensity envelope in time. The compressed pulse has a flat phase over the entire amplified bandwidth, resulting in a pulse duration of 8.5 fs which is within 6% of the Fourier-limit. The maximum measured deviation from the shortest pulse duration is 0.6-fs. This can mainly be attributed to the amplified signal energy stability (4.5%) and to the measurement error caused by the pointing instability of the system. The amplified pulse compression was reproducible and the shot-to-shot pulse duration fluctuation was measured for the first time for OPCPA with a single-shot SPIDER apparatus [163] (standard deviation ~0.3-fs). The single-shot SPIDER remains a key component for fast and reliable compression due to the low-repetition-rate (10 Hz) of the OPCPA amplifier.

3.5.4 Temporal pulse contrast

A good temporal pulse contrast in OPCPA is necessary but difficult to obtain. We have investigated the contrast implication in OPCPA [98] and performed optimization measurements with a specially developed, long scanning range, high-dynamic-range third-order autocorrelator.

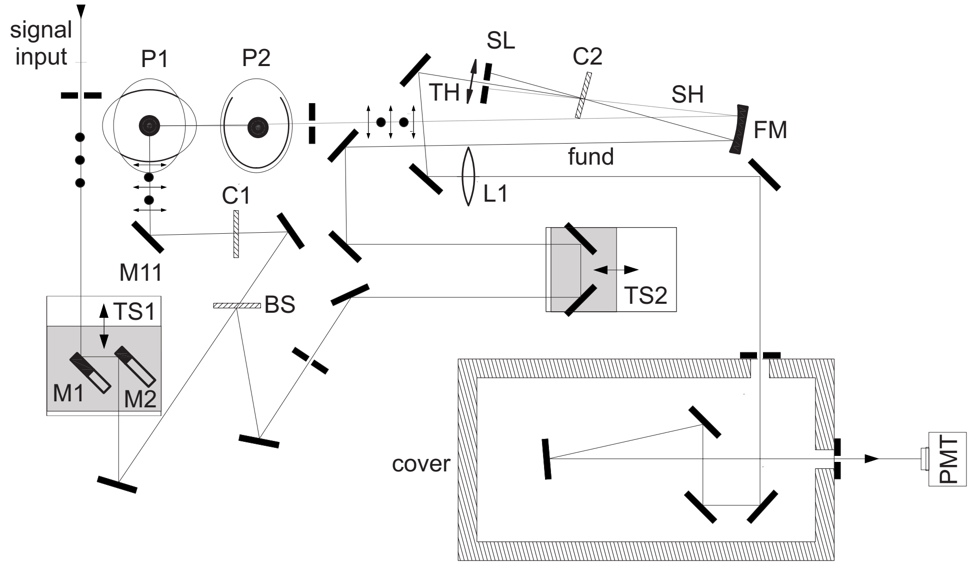

Figure 3.26: Optical layout of the third-order correlator (courtesy of K. Schmid). TS1...translation stage; M1, M2...Mirrors which are only partially coated (to avoid saturation); BS...pellicle beam splitter; C1...SHG crystal BBO-100 μm; M-Ag...Ag-broadband mirrors; P1...Periscope; P2... height-change. P1 and P2 equipped with dichroic mirrors for SH; FM...focussing mirror, f = 100 mm; C2...THG crystal BBO-100 μm; SL...slit; L1...lens, f = 100 mm; TS2...translation stage for time delay; PMT...solar-blind photomultiplier tube Hamamatsu R2078-2.

In a third-order correlation, every pre-pulse or post-pulse will generate a peak at positive (after the main pulse) or negative (before the main pulse) delays as well, but this artifact will be of smaller amplitude than the peak at the real position of the pulse satellite. In a correlation-trace, which is normalized to one, the contrast ratio between the main pulse and the ghost pulse is given approximately by the square of the true contrast of the satellite.

A third-order correlator was developed for pulse contrast measurements with a scanning range of more than 600 ps and a dynamic range larger than 9 orders of magnitude. The optical layout of the third-order correlator is sketched in Fig. 3.26. The correlator is based on type-I phase-matched second harmonic generation, followed by type-II third harmonic generation (SHG and THG, respectively) in BBO crystals. Careful suppression of the background allows to reach a dynamic range exceeding 9 orders of magnitude. A detailed description of the correlator is given in [98].

One of the main conclusions from our measurements has been, that the delay between

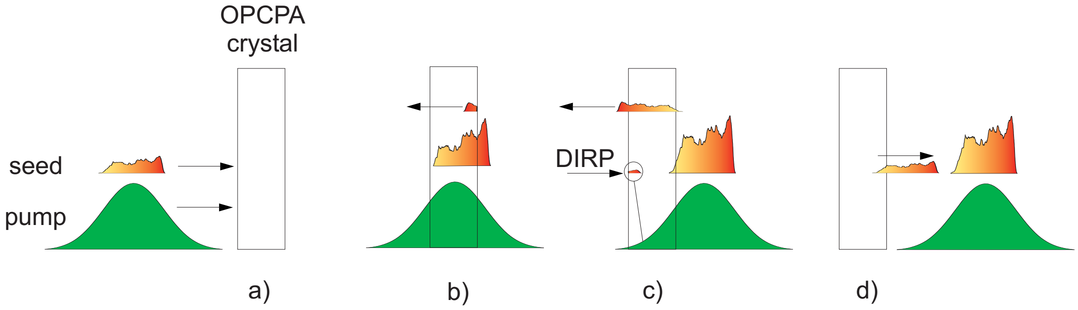

Figure 3.27: Double internally reflected pulse amplification process in an OPCPA.

the seed- and the pump-pulse strongly influences the compressed pulse contrast-ratio. To investigate the contrast near the main pulse in more detail, we limited the scanning range of the correlator to ±55 ps. For this measurement only two OPCPA stages has been used, yielding an amplified pulse energy of 1.5mJ, less than one tenth (130 μJ) of which was used for the correlation measurements. The results are summarized in Fig. 3.28(a), which depicts four autocorrelation traces recorded at different delays between seed and pump pulse. The zero delay between the pump and the seed pulse corresponds to a delay setting where the contrast between the main pulse and superfluorescence background was highest. For this delay on the leading edge of the pulse, contrast is equal to $\sim 10^{-4}$.

We attribute the post-pulse appearing at +48.5 ps to the DIR (doubly internally reflected, see Fig. 3.27) pulse in the 4.4 mm BBO-crystal of the first stage which was further amplified as well in the second stage. The post-pulse appearing at +15.3 ps was identified as resulting from parasitic reflection inside the pulse stretcher. This measurement allows us to conclude that delaying of the seed pulse with respect to the pump pulse facilitates more efficient amplification of optical parametric fluorescence in the pulse front and causing deterioration of the main pulse contrast (Fig. 3.28(a)). Furthermore, with the increasing seed delay the pedestal energy redistribution from the trailing-edge to the leading-edge of the pulse is clearly evident. Together with the correlation measurements we measured amplified pulse spectra for different seed delays. The spectrum of the amplified pulses becomes narrower for the seed delayed in respect to the pump. The spectrum is shifted towards shorter wavelengths, whereas for the opposite direction we observed stronger amplification in the near-infrared. This indicates that the amplified pulse spectrum is also sensitive to the pump-seed temporal overlap, particularly for the long seed delays, and that the sharp edge near 700 nm or spectral components appearing around 1 μm in the amplified spectrum indicates presence of the stronger superfluorescence background. However, due to the high sensitivity of the amplified spectrum on the system alignment it is impossible to assess the amplified pulse contrast-ratio from the spectral measurements.

We have also performed measurements over an increased scanning range by using the maximum output of the system from two OPCPA stages. These measurements, reveal a second post-pulse at +61.5 ps, which stems from the 5.5 mm BBO crystal in the second stage (Fig. 3.28(b)). The same post-pulses cause another series of two DIR pulses in the

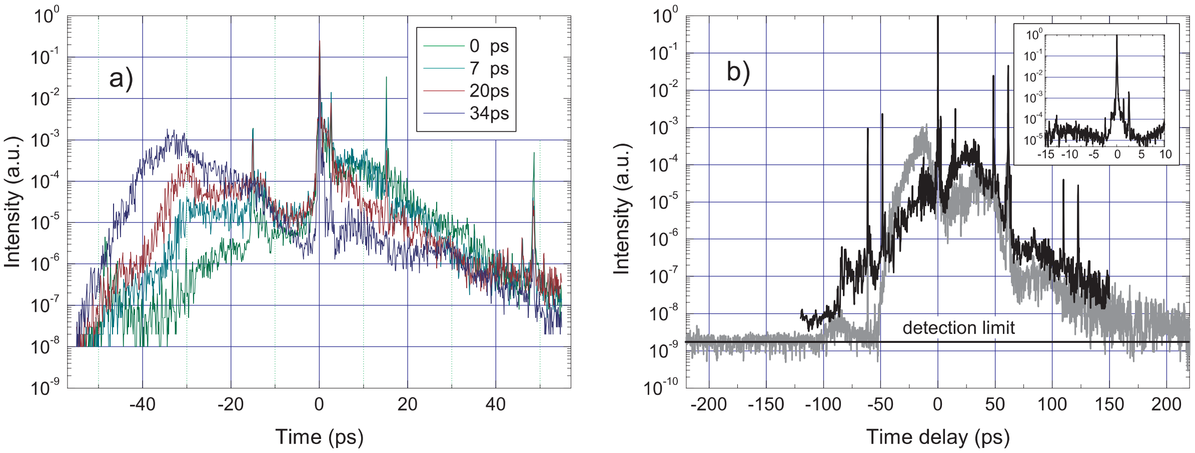

Figure 3.28: (a) Autocorrelations recorded using only approximately 130 μJ pulse energy with different delays between seed and pump. Beginning at an optimal setting (zero delay), autocorrelations have been recorded for the seed being delayed 7, 20 and 34 ps, respectively. The signal energy during the measurements was $\sim$ 1.5 mJ; (b) Autocorrelations recorded using approximately 700 μJ pulse energy out of 3 mJ using 2 OPCPA stages. Grey line: not optimized pulse contrast, black line: pump-seed delay in first and second stage optimized for maximum contrast.

second stage which appears in the correlation trace at 110 ps and 123 ps. The broad pedestal from -55 ps to +55 ps in the third order correlations depicted in Figs. 3.28(a) and 3.28(b) originates from parametric fluorescence generated and amplified in the OPCPA stages. The background between 65 ps and 150 ps with approximately 10^{-6} pulse contrast is attributed to the double reflection in the second BBO crystal of the pedestal produced in the first stage. The measurement was performed with 700 μJ of the 3 mJ pulses coupled into the correlator. At this energy, the dynamic range of the correlator is 9 orders of magnitude, allowing the conclusion that OPCPA contrast at large delays is equal to or better than that. It can also be seen that the best pulse-contrast obtained in these measurements is larger than four orders of magnitude at ±25 ps. By integrating the respective parts of the correlations, it is possible to estimate the energy content of the pedestal and of the main pulse. The energy content of the main pulse for the 0 ps pump-seed delay in Fig. 3.28(a) is $> 75\%$, with the leading part of the pedestal from -100 ps to -0.1 ps carrying less than 1.4%. In the non-optimized case, 5% of the energy is in the leading part of the pedestal and the main pulse contains 93%. At this delay between seed and pump pulses the amplification of the DIR pulses is thus much less pronounced. So at least in our current OPCPA system, there seems to exist a trade off between the energy in the main pulse and the contrast between main pulse and pedestal, because for high contrast it is necessary to shift the seed more to the leading part of the pump pulse, which will result then in stronger post-pulses. One possibility to suppress amplification of the DIR pulses is development of the lower reflectivity broadband antireflection coatings for the BBO crystals.

Contrast measurements are performed with three OPCPA stages. The measurements

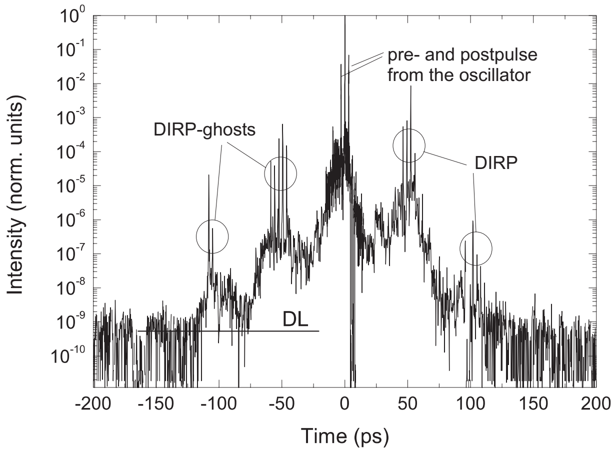

Figure 3.29: Third order autocorrelation trace third stage near saturation with an output energy of ∼40 mJ; DL...detection limit.

shown in Fig. 3.29 are taken with OPCPA stage near saturation. The amplified signal energy is ∼40 mJ and as is shown in this figure, the pedestal starts from 7 and ends up with 4 orders of magnitude less intensity compared to the main pulse in the ps-region from -50 ps to zero delay. The post- and prepulse in Fig. 3.29 stems from intrinsic multi-pulse operation in a broadband oscillator near zero net-internal dispersion (see oscillator section). In the case of saturated amplifier the superfluorescence pedestal rise to between 3 and 4 orders of magnitude pedestal. This contrast ratio is unsuitable for most experiments which involve plasma formation already at low intensities. Simulation has been performed to estimate the exact amount of superfluorescence in case of saturated last amplifier stage, since a precise and direct measurement of superfluorescence in a saturated parametric amplifier is impossible due to quencing effects of the signal. The results are shown in the previous simulation chapter.

3.5.5 Wavefront and focus measurements

Another important characteristic parameter for an amplifier used in high-field experiments is the wavefront of the amplified and compressed signal. The wavefront determines the quality of the focus that can be achieved using a short focal distance parabolic mirror to obtain highest intensities in the smallest possible focal spot.

The wavefront in the present setup shows wavefront distortions caused mainly by the SF57 compressor glass blocks. The two glass blocks introduce a peak to valley distortion of 0.7 μm and 1 μm respectively. Additional beam astigmatism is introduced by the compressor telescopes. This astigmatism can be compensated by the alignment of the parabolic mirror. The wavefront of the signal after the compressor is shown in Fig. 3.30(a), the focus that can be obtained is calculated by means of the point spread function Fig. 3.30(b) and a measured focus using a f = 150 mm ($f^{\#}3$) gold coated Janos parabola is shown in Fig. 3.30(c). The measured focus has a FWHM waist of >3 μm. For a gaussian beam,

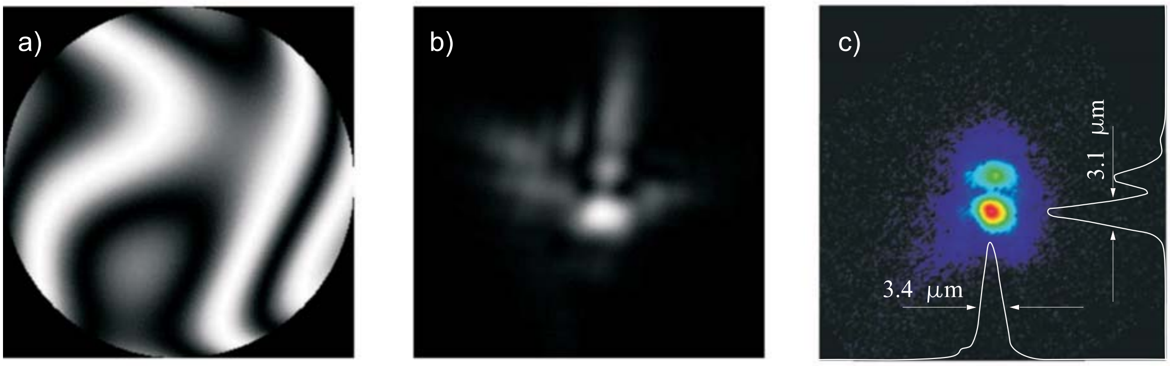

Figure 3.30: Shack-Hartman wavefront interferogram (a); (b) calculated focus from the wavefront measurement; (c) focal intensity distribution obtained with a short focal distance parabola (f = 150mm) for 80 mJ amplified signal energy.

$$w_0 \simeq \frac{\lambda}{\pi\Theta} \quad \text{with} \quad \Theta = \arctan\frac{D}{2f}. \tag{3.29}$$

w_0 is the waist radius, Θ is the divergence angle in rad, D is the beam aperture on the parabolic mirror, f is the focal distance of the parabolic mirror and λ is the central wavelength of 850 nm. The value for w_0 is given at 1/e^2. The minimum beam diameter at FWHM for a gaussian beam can be evaluated as $d_{FWHM} = w_0\sqrt{2\ln 2} \simeq 2\mu$m. The amplified spatial beam profile from the OPCPA has a multimode spatial distribution. The pulse quality is described by the pulse propagation factor M^2. The M^2 for a gaussian pulse distribution is 1. The pulse quality loss will increase (M^2 >1), for a pulse shape different than Gaussian. The focal spot size w_{m0} obtainable for a multimode beam differs from the gaussian by w_{m0}=w_0M^2. The quality factor M^2 for a supergaussian beam is defined as

$$(\mathrm{M}^2)^2 = \frac{2n}{3}\frac{\Gamma(2-1/2n)\Gamma(1+3/2n)}{[\Gamma(1+1/2n)]^2}. \tag{3.30}$$

$\Gamma(x)$ is the Gamma function and n is the order of the gaussian mode. M^2 is 1.39 for a 4th order gaussian beam and the smallest focal spot at FWHM is d_{FWHM}=2.78μm.

The wavefront distortions could slightly be further reduced by exchange and by 90° rotation of the SF57 glass blocks in order to eliminate higher order wavefront distortions. Using this simple trick, the wavefront of the combined SF57 glass blocks could be reduced to an average of 0.35 μm peak to valley distortion. Nevertheless a newly acquired adaptive optics system with a DM30 deformable mirror from Imagine Optics and Cilas is used to

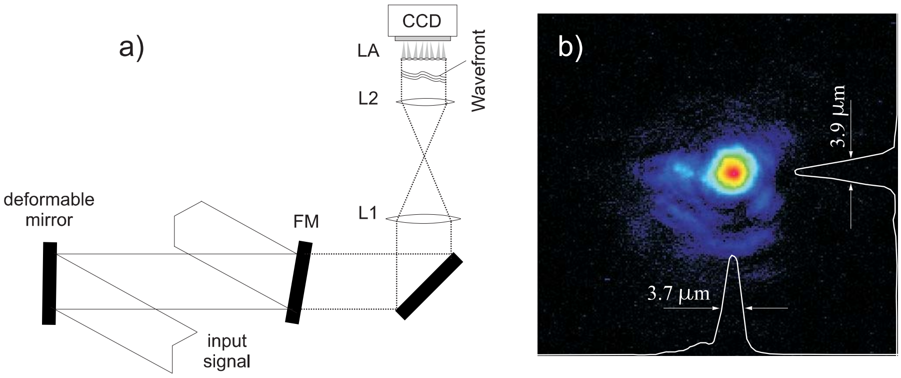

Figure 3.31: (a) Optical scheme of the Shack-Hartmann wavefront sensor. FM...beamsplitting mirror with 10^{-4} transmission; L1, L2...telescope to image the wavefront onto the lenslet array; LA...lenslet array; CCD...charged coupled device; (b) typical focus obtained with adaptive optics.

correct for wavefront distortions more easily on daily basis. The wavefront of the amplified signal is measured by Shack-Hartmann technique [166, 167]. The beam is imaged onto a lenslet array which focuses portions of the beam on a CCD as shown in Fig. 3.31(a). The position of the foci is given by a deviation from the optical axis of the single lenslet which is proportional to the local gradient of the wavefront. The entire beam wavefront can be reconstructed from the information of all foci. The wavefront aberrations are represented by a linear combination of Zernike-polynomials, which are used to describe classical aberrations like astigmatism, coma, spherical abberations, etc. The wavefront information gained from the Shack-Hartmann measurement is used to steer the deformable mirror in a closed loop configuration, in order to correct for wavefront aberrations. A typical focus obtained during experiment using a f=150mm silver coated Sorl parabola ($f^{\#}3$) is shown in Fig. 3.31(b). The FWHM diameter for a gaussian beam at the focus is 3.7 μm. The RMS value for the wavefront distortion measured by the Shack-Hartmann sensor is below $\lambda/10$.

3.6 OPCPA with Ti:Sapphire amplifier front-end

3.6.1 Amplified signal energy and spectrum

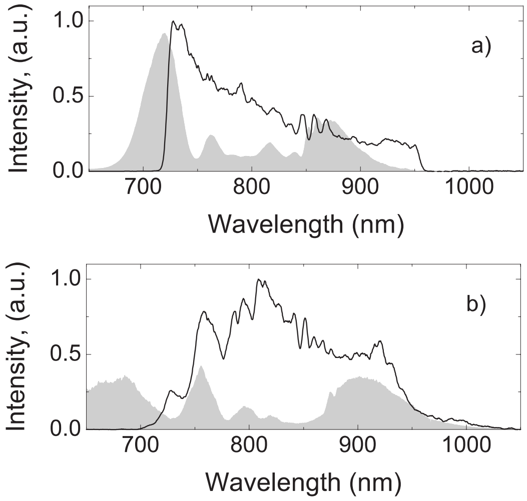

Figure 3.32: (a) Spectrum of the seed (shaded grey line) and spectrum of the amplified pulses (black line) for usual hollow-core fiber operation at 1.6 bar; (b) Spectrum of the seed (shaded grey line) and spectrum of the amplified pulses (black line) for unstable hollow-core fiber operation at 2.5 bar.

The OPCPA with Ti:sapphire amplifier front-end differs marginally from the scheme with Ti:sapphire oscillator seed. The amplifier layout is shown in Fig. 3.4(c). Two OPCPA stages are used for amplification, as the seed pulse energy is already in the μJ-level, which was previously reached only after the first OPCPA. A seed with several hundreds μJ energy (spectrum shown in Fig. 3.32(a) and (b), shaded grey line), is amplified in the first OPCPA stage (I_p=8 GW/cm^2) to 2 mJ energy and in the second stage (I_p=4.5 GW/cm^2) to 90 mJ. This is the highest amplified energy ever reached for few-cycle sub-10-fs pulses. Previously, the highest energy with saturation in the last OPCPA stage was 80 mJ, by seeding with a Ti:sapphire oscillator, and 30 mJ energy was amplified OPF. The amplified spectra are shown in Fig. 3.32(a and b, solid line). The difference between the spectra in Fig. 3.32(a and b) are different modes of operation of the hollow-core fiber broadening process. The spectrum broadened in the hollow-core fiber shown in Fig. 3.32(b) is broader compared to the spectrum in Fig. 3.32(a) but the operation is less stable in terms of energy stability (>1.5% RMS). Therefor, the operation with the spectrum from Fig. 3.32(a) is usually used to assure sufficient amplified pulse energy stability (<1% RMS). The measurements of the amplified pulse spectrum for hollow-core fiber operation under less stable conditions (spectrum, Fig. 3.32(b)) shows the possibility to gain the infrared wing which is otherwise lost.

3.6.2 Pulse compression

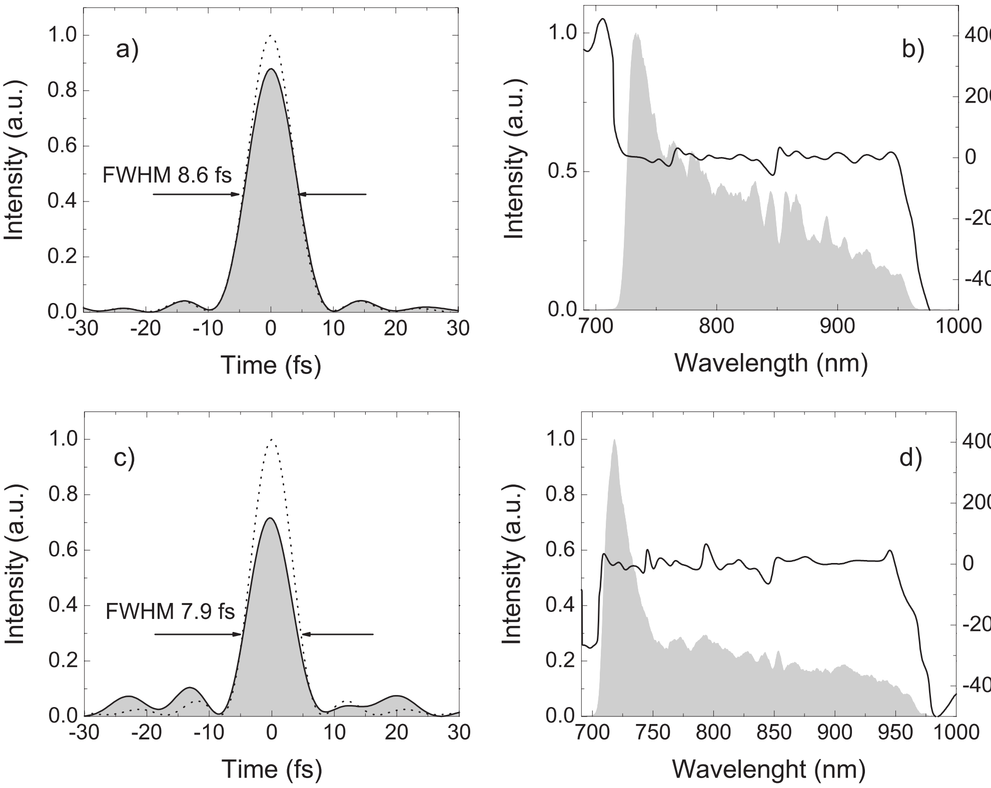

Figure 3.33: Compressed amplified signal pulse: (a) recompressed 90 mJ pulse (8.6 fs at FWHM). The dotted curve corresponds to the intensity profile of the transform-limited pulse (FWHM= 8.1 fs) calculated from the amplified spectrum; (b) retrieved amplified pulse spectrum (shaded contour) and group delay (solid curve); (c) recompressed 40 mJ pulse (7.9 fs at FWHM). The dotted curve corresponds to the intensity profile of the transform-limited pulse (FWHM= 7.6 fs) calculated from the amplified spectrum; (d) retrieved amplified pulse spectrum (shaded contour) and group delay (solid curve).

Compression of 90 mJ pulse energy is achieved to a pulse duration of 8.6 fs at FWHM (Fig. 3.33(a)). The Fourier-limited pulse duration of the pulse spectrum (Fig. 3.33(b)) is 8.1 fs. The retrieved group delay curve from the SPIDER measurement is shown in Fig. 3.33(b) also. The average deviation of consecutive shots is $<3\%$, compared to the best compressed pulse duration obtained.

Another pulse duration measurement was performed after amplification of a broader spectrum by large angular detuning of both OPCPA stages, obtaining additional spectral components at both edges of the amplified pulse spectrum (Fig. 3.33(d)). The Fourier-transform-limited pulse duration of this spectrum is 7.6 fs at FWHM. The best SPIDER phase-retrieval shows a compressed pulse duration of 7.9 fs at FWHM (Fig. 3.33(c)). This is to our knowledge, among the shortest pulse duration obtained for a multi-mJ OPCPA system. Unfortunately, the amplified pulse energy is only about 40 mJ due to the angular detuning.

Most of the output beam parameters as energy stability or spatial beam profile are same as already described in previous sections and are not further mentioned here. However, a very important parameter which is expected to change is the temporal contrast.

3.6.3 Temporal pulse contrast

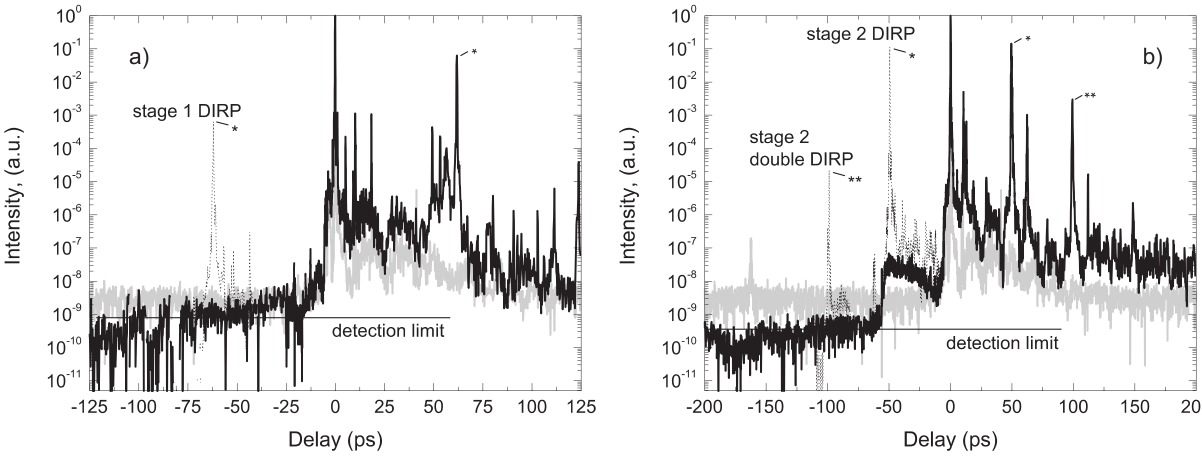

Figure 3.34: (a) Temporal pulse contrast measurement after the first OPCPA stage (black line); (b) temporal pulse contrast measurement of the amplified signal pulses for saturated second OPCPA stage (black line). For (a) and (b), temporal contrast measurement of the Ti:sapphire front-end pulses for comparison (gray line).

Previously demonstrated OPCPA system suffered from poor pulse contrast due to the low seed energy available at the first stage of amplification. For the stronger seed source seeding, the temporal contrast is characterized for first and second OPCPA stage separately. During the third order autocorrelation measurement in the first stage, the OPCPA stage output is tuned from 2 mJ to 5 mJ to increase the dynamic range of the autocorrelator for contrast characterization. The measurement is shown in Fig. 3.34(a, black line). The temporal contrast of the seed is shown in the same figure (grey curve) for comparison. The contrast after the first stage is improved in the pulse front (<-50 ps) by minimum one order of magnitude. Additionally, in order to obtain a more realistic estimate of the contrast in the pulse-front, the ghost of the DIRP in the correlation trace is removed from the autocorrelation trace (DIRP-ghost is depicted as dotted grey line in Fig. 3.34(a)) and replaced by a corresponding trace frame from the contrast measurement of previous amplification stage.

The second stage is measured with full saturation and with 1.3 mJ from the first stage. The pulse contrast, far from 0-ps delay, is better than 9 orders of magnitude in the pulse front (Fig. 3.34(b)), which is the detection limit of the third order correlator. Between -50

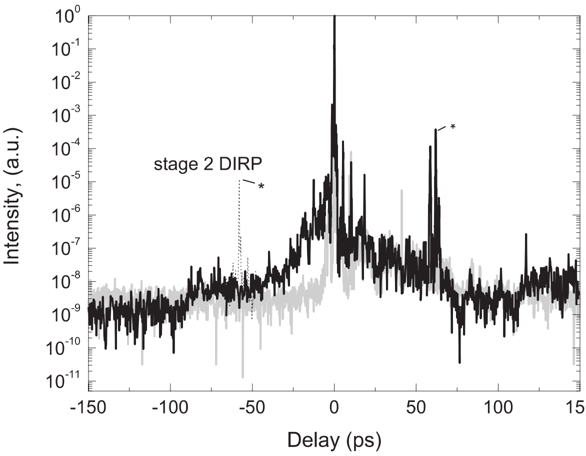

Figure 3.35: Temporal pulse contrast measurement of the amplified signal pulses for saturated second OPCPA stage with DIR-pulse suppression (black line); temporal contrast measurement of the Ti:sapphire front-end pulses for comparison (gray line).

ps and the main pulse a noise pedestal is amplified in the gain region of the pump to 8 orders of magnitude contrast. This is to our knowledge the highest contrast ever measured for few cycle pulse OPCPA with energy levels towards 100 mJ. An undesired feature present in all contrast measurements is the double internally reflected pulse (DIR-pulse), which is amplified along with the main pulse. The gain window of the pump pulses is larger than the propagation time of the DIR-pulse in the crystal and thus, it can still reach remarkable energy levels. The reflection of the DIR-pulse in the second stage without amplification in stage 2 is estimated to be less than 10^{-2} by contrast measurement with inactive stage 2. The DIR-pulses are further amplified and are able to reach energy levels of even 10% of the main pulse energy as is shown from the measurement in Fig. 3.34(b). It is possible to suppress DIR-pulse amplification by extreme careful handling of the pump-to-signal overlap, as shown in Fig. 3.35. The price is a reduced amplification of spectral components in the infrared spectral wing and is not considered as a final solution.

A possible solution to eliminate the DIR-pulses is the implementation of wedged crystals. This measure should permit the retro-reflected pulse from an OPCPA stage not to reach the next stage of amplification. The wedge-angle should be kept small to avoid non-uniform amplification of the beam along the wedged axis (axis of the principal plane, normal to the pump beam propagation in BBO). Another possibility is to use thicker crystals, thus having a larger separation between the main pulse and the DIR-pulses.

3.6.4 Summary of results

The previous OPCPA setup with Ti:sapphire oscillator front-end was able to deliver 110 mJ of energy. 80 mJ out of this energy content was amplified signal energy (30 mJ AOPF), allowing the temporal contrast to be only around 3 to 4 orders of magnitude from the main pulse to the onset of AOPF-pedestal in the pulse front with pulses compressed to 8.5 fs.

The pulse duration is within 6% of their Fourier-transform-limited pulse duration which is 8 fs. A peak power of 9.5 TW is reached with this pulse parameters. The signal beam can be focused to a spot size of 3 μm in the FWHM diameter. The energy content for the focus is estimated to be 80% in $1/e^2$. This results in a focal intensity exceeding $1{\cdot}10^{19}$W/cm^2.

It is important to mention that many high-field experiments require a contrast, more than 7 orders of magnitude. In this low seed energy version of the amplifier, the maximum reachable contrast was low for saturation in the last OPCPA stage. Therefor, a new Ti:sapphire front-end is used for seeding the OPCPA. This allows to reduce the number of OPCPA amplifier stages in our setup by one.

Few-cycle pulses with durations of 8.6 fs can be amplified to 90 mJ with highest contrast reaching peak powers exceeding 10 TW. The amplified pulses could be compressed even to shorter pulse duration, 7.9 fs, for amplified pulse spectra with broader bandwidth, obtained by angular detuning of both OPCPA stages, but unfortunately on the expense of the amplified output energy (40 mJ). The temporal contrast is minimum 9 orders of magnitude in the pulse front on the ps-scale. The amplifier is furthermore scalable to higher amplification levels. The only limitation in the present setup are self-action effects in the compressor glass blocks limiting the achievable peak power to approximately 30 TW. The pump amplifier has upgrade potential and is not a limitation.

Chapter 4

Test-ground for experiments in high-field physics

The content of this chapter is dedicated to first experiment performed with the few-cycle pulse amplifier system, which is subject of this thesis.

4.1 Electron acceleration in the "Bubble" regime

Laser-driven electron acceleration in plasmas has been subject of interest for the past decades. Huge static electric fields can be attained in laser plasmas, compared to electric fields in conventional RF-accelerators ($E_{plasma} \sim 10^3 - 10^4 E_{RF}$). Moreover, shortest electron bunches with durations well below the laser pulse duration can be obtained, thus reaching highest electron densities with peak currents in the kA range.

An intense electromagnetic wavepacket drives a plasma wake through the action of the nonlinear ponderomotive force. The condition for laser-light propagation in plasma is satisfied in an underdense plasma, where the plasma frequency $\omega_p = (\frac{e_0^2 n_e}{\varepsilon_0 m_e})^{\frac{1}{2}}$ is smaller than the frequency of light. Electrons, trapped in the wake, can be accelerated to highest temperatures. This was shown first, in 1979, by Tajima and Dawson through theory and simulation [168].

The phenomenon of laser-driven electron acceleration has been extensively studied during the last years and two main mechanism of electron acceleration has been discovered. The process of direct laser acceleration (DLA) was subject of intense investigations, because it was accessible with long-pulse lasers, not necessarily based on Ti:Sapphire gain medium [169]. The dominant process in DLA is the acceleration of electrons by the transverse electric field $\mathrm{E}_{\perp}$ of the laser light. The driving process in laser-wakefield acceleration (LWFA) is a plasma wave, driven by the ponderomotive force induced by the electric field of the laser light $\mathrm{E}_{\|}$ and magnetic field in the plasma [170, 171]. The long laser pulse gets self-modulated with the plasma period, and only then, effective wakefield excitation is obtained if the modulation and the plasma period are in resonance. Electron spectra from these two acceleration mechanisms have Maxwellian spectral distributions. An excellent overview of research on this type of acceleration is given in Ref. [172].

A new mechanism of electron acceleration is expected in the strongly nonlinear LWFA regime, for the envelope of the driving laser pulse enclosing only few cycles of electric field oscillations and the pulse duration shorter than the plasma period ($\sim \frac{1}{\omega_p}$). The regime of acceleration is reached directly, in laser wakefields driven above the wavebreaking threshold. The acceleration takes place in the first wave-packet at relativistic intensities (10^{18} Wcm^{-2}), reached with a few-cycle laser-pulse, where a solitary plasma cavity is formed, which continuously traps and accelerates electrons [51, 173]. The plasma wave trails the laser pulse with a phase velocity set by the group velocity of the laser pulse

$$v_{ph}^{wake} = v_g = c_0(1 - \frac{\omega_p^2}{\omega_0^2})^{\frac{1}{2}} \tag{4.1}$$

with $\omega_0 = \frac{2\pi c_0}{\lambda_0}$ the center frequency of the laser pulse. The phase velocity is determined by the electron density in the plasma, which is usually set in a range between 0.1% and 10% of the critical density [51]

$$\frac{n_{crit}}{n_0} = \frac{\omega_0^2}{\omega_p^2} = 100. \tag{4.2}$$

This special case of electron acceleration is referred to as "bubble" electron acceleration. This is the only known mechanism for acceleration of quasi-monoenergetic electrons. The laser pulse can exert a more efficient excitation when the laser pulse is shorter than ω_p and fits in the first half of the exited plasmon.

Nonetheless, the "bubble"-electron acceleration regime can also be reached using longer driver-pulses (Ti:sapphire, 35-50 fs in duration). An intense laser pulse drives a wake, forms a relativistic channel and gets self-modulated with the plasma period. Instabilities grow during the electron acceleration process due to this mechanisms. Only the leading part of the pulse contributes to the "bubble" formation, this leads in this case to less efficient energy transfer between light wave and electrons. Acceleration of "quasi-monoenergetic" electrons has been reported for the first time by three different research groups, fulfilling successfully theoretical predictions [48–50]. These groups reached independently acceleration of quasi-monoenergetic electron peaks to highly relativistic energies.

The growing interest for this hot topic in the scientific community, incited many research groups to repeat and optimize the experiment [174–176]. Electron energies on the order of 100-300 MeV and even beyond, up to the GeV-level, could be reached during experiments using a gas-filled capillary discharge waveguide to prolong the plasma channel over several centimeter in length [52], at the expense of electron bunch charge. Unfortunately, one of the most important parameter, the shot-to-shot energy stability remains to be improved. A strong effort to reach a stable operation regime has been endeavored. The result is still not satisfying, more complicated setups are the result and laser pulse-parameter discrimination is used as last resort [177, 178]. The reproducibility of electron bunch parameters still suffer from lack on reproducibility.

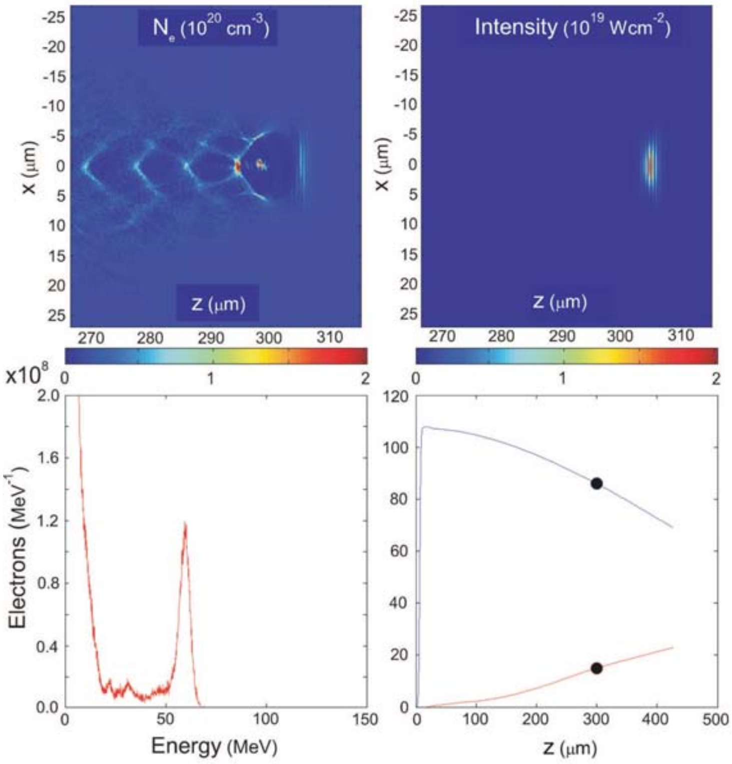

Figure 4.1: Electron acceleration. 3D-PIC simulation of plasma "bubble" formation with an intense few-cycle pulse (courtesy of M. Geissler).

3D-PIC simulation showed that there is a good chance to obtain reproducible bunch parameters while keeping the experimental setup simple by reaching the "bubble" regime directly using a few-cycle laser pulses from an amplifier capable to deliver relativistic intensities in the focal region. Using sub-10-fs laser pulses to drive the plasma bubble should overcome the lack of reproducibility by direct access to the "bubble" acceleration regime. A consequence are strongly reduced parametric instabilities in the plasma [51]. The current OPCPA amplifier we use for electron acceleration fulfills the necessary requirements so far.

The short pulses from the OPCPA used in the experiment, reach a pulse peak power of P_{laser}=10 TW, with a pulse duration of τ_p=8.5 fs (center wavelength λ_0=850 nm). A first approximation of electron energy and charge yield in the electron bunch can be estimated by the scaling laws of A. Pukhov *et al.* [179], which are valid for $a_0 \gg 1$. The electron energy of the quasi-monoenergetic peak estimated with the scaling law is

$$E_{mono} = 0.65 m_e c_0^2 \sqrt{\frac{P_{laser}}{P_{rel}}} \frac{c_0 \tau_p}{\lambda_0} \approx 40\text{MeV} \tag{4.3}$$

and the electron-bunch charge

$$N_{mono} = \frac{1.8\lambda_0}{2\pi r_e}\sqrt{\frac{P_{laser}}{P_{rel}}} \approx 300\text{pC}. \tag{4.4}$$

$P_{rel} = \frac{m_e^2 c_0^5}{e_0^2} \sim 8.5$ GW is the natural relativistic power unit and $r_e = \frac{e_0^2}{m_e c_0^2}$ is the classical electron radius. This scaling law is a rough guide and seem to give a quantitative good result, which coincides also with the estimation obtained by 3D-PIC calculation of M. Geissler [51] in terms of electron energy, but differ in effective bunch charge. These simulations are more precise and are tailored for ultrashort pulses with laser parameters we use for electron acceleration. The simulation is performed for 100 mJ pulse energy, a pulse duration of 10 fs at FWHM and a beam waist of 10 μm. The result are electron energies around 50 MeV and an electron bunch charge of around 150 pC in the quasi-monoenergetic peak (Fig. 4.1).

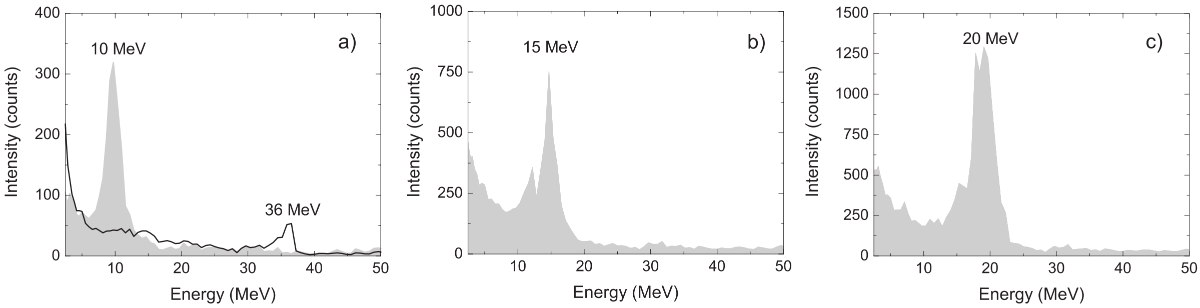

Figure 4.2: Typical spectrum of electrons accelerated with sub-10-fs pulses with monoenergetic peak at 10 MeV (a), 15 MeV (b), 20 MeV (c) and Highest reached electron energy in the monoenergetic peak at 36 MeV, solid curve (a).

During the first experimental campaign, we successfully demonstrated laser-driven "bubble"-electron acceleration. The highest mono-energetic energy reached is 36 MeV (see Fig. 4.2(a, solid curve)). Typical electron energies obtained are in the range between 10-30 MeV depending on laser-amplifier specific parameters and several experimental conditions (pulse duration, focal intensity, pulse contrast ratio, density gradient of plasma, plasma density, nozzle type in use, etc.). The best energy spread at FWHM in the quasi-monoenergetic peak $\frac{\delta E}{E}$ is ∼5%, obtained for the spectrum in Fig.4.2(b). We could find a highly stable regime of acceleration of Maxwellian distributed electrons in terms of energy distribution and intensity counts. The position of the quasi-monoenergetic peak in the electron spectrum was of rather sporadic nature, even though with periodical appearance. Many of the electron spectra show a evanescent small amount of low-energetic Maxwellian distributed electrons as can be observed in Fig. 4.2(a,b and c), which is an indication for direct "bubble" formation. The average electron charge in the quasi monoenergetic peak is estimated to be several tens of pC. This was measured by an on-line Rogowsky coil, which was cross calibrated by an image-plate detector. The laser pulse energy used in experiments is about only 65 mJ which shows the extreme increase in acceleration efficiency compared to acceleration with long-pulse laser amplifiers. Amplifiers capable to provide Joule-level pulse energy. The amount of laser energy necessary to reach the solitary cavity regime strongly increases with the pulse duration. Another mentionable fact is the low radiation level of less than 1 μSv per hour, during the observation time of Maxwellian distributed electrons and quasi-monoenergetic features in the electron spectra. This is very convenient for practical applications as it allows a higher repetition rates.

Appendix A

Refractive index

A.1 Refractive index of isotropic materials and nonlinear optical crystal

The refractive index of isotropic optical materials SF11 [181], SF57 [181], fused silica (FS) [182] and of the birefringent crystal TeO_2 [183] which is used for the Dazzler (acousto-optical dispersive filter) can be derived from the well-known Sellmeier dispersion formula in form of

$$n(\lambda) = \sqrt{1 + \frac{B_1\lambda^2}{\lambda^2 - C_1} + \frac{B_2\lambda^2}{\lambda^2 - C_2} + \frac{B_3\lambda^2}{\lambda^2 - C_3}}. \tag{A.1}$$

The coefficients B_i and C_i are listed in table A.1.

The refractive index for the nonlinear optical crystals BBO [184], LBO [185] and BIBO [79] and for the laser material Nd:YAG [186] are derived from the Sellmeier dispersion formula in form of

$$n(\lambda) = \sqrt{A + \frac{B}{\lambda^2 - C} + D\lambda^2 + E\lambda^{-4}}. \tag{A.2}$$

The coefficients A-E are listed in table A.2. The refractive index of air is given in eq. A.3 by the formula derived from Edlen [187]. It is used to estimate the pulse broadening during propagation of femtosecond optical pulses over long distances.

$$(n(\lambda) - 1)10^8 = 6431.8 + \frac{2949330}{146 - k_0^2} + \frac{25536}{41 - k_0^2}. \tag{A.3}$$

k_0 is the vacuum wavenumber given in μm^{-1}.

Materials	B_1	B_2	B_3	C_1	C_2	C_3
SF11	1.73848403	0.311168974	1.17490871	0.0136038604	0.0615960463	121.922711
SF57	1.81651371	0.428893641	1.07186278	0.0143704198	0.0592801172	121.419942
FS	0.6961663	0.0046791	0.4079426	0.0135121	0.8974794	97.934003
TeO_2 ^{o}	2.584	1.574	–	0.01800964	0.06959044	–
TeO_2 ^{e}	2.823	1.542	–	0.01800964	0.06922161	–

Table A.1: Coefficients for the Sellmeier dispersion formula Eq. A.1 (SF11, SF57, FS, TeO_2); λ in μm.

Materials	A	B	C	D	E
BBO ^{o}	2.7359	0.01878	0.01822	−0.01354	–
BBO ^{e}	2.3753	0.01224	0.01667	−0.01516	–
LBO ^{x}	2.454140	0.011249	0.011350	−0.014591	$-6.6 \cdot 10^{-4}$
LBO ^{y}	2.539070	0.012711	0.012523	−0.018540	$2.0 \cdot 10^{-4}$
LBO ^{z}	2.586179	0.013099	0.011893	−0.017968	$-2.26 \cdot 10^{-4}$
BIBO ^{x}	3.6545	0.0511	0.0371	−0.02260	–
BIBO ^{y}	3.0740	0.0323	0.0316	−0.01337	–
BIBO ^{z}	3.1685	0.0373	0.0346	−0.01750	–
Nd:YAG ^{o}	3.77834	0.069736	0.04724	−0.010813	–
Nd:YAG ^{e}	4.59905	0.110534	0.04813	−0.012268	–

Table A.2: Coefficients for the Sellmeier dispersion formula Eq. A.2 (BBO, LBO, BIBO and Nd:YAG); λ in μm.

Bibliography

[1] T.H. Maiman, "Stimulated Optical Radiation in Ruby", Nature **187**, 493494 (1960).

[2] A. Javan, W.R. Bennett, and D.R. Herriott, "Population inversion and continuous opticalmaser oscillation in a gas discharge containing a He-Nemixture", Phys. Rev. Lett. **6**, 106-114 (1961).

[3] E. Snitzer, "Optical maser action of Nd^{3+} in a Barium crown glass", Phys. Rev. Lett. **7**, 444-450 (1961).

[4] R.N. Hall, G.E. Fenner, J.D. Kingsley, T.J. Soltys, and R.O. Carlson, "Coherent light emission from GaAs junctions", Phys. Rev. Lett. **9**, 366 (1962).

[5] P.P. Sorokin, J.R. Lankard, E.C. Hammond, and V.L. Moruzzi, "Laser-pumped stimulated emission from organic dyes: experimental studies and analytical comparisons", IBM J. Res. Devel. **11**, 130-148 (1967).

[6] P.P. Sorokin, J.R. Lankard, V.L. Moruzzi, and E.C. Hammond, "Flashlamppumped organic-dye lasers", J. Chem. Phys. **48**, 4726-4742 (1968).

[7] J.A. Myer, C.L. Johnson, E. Kierstead, R.D. Sharma, and I. Itzkan, "Dye laser stimulation with a pulsed N_2 laser line at $3371\mathring{A}$, Appl. Phys. Lett. **16**, 3-6 (1970).

[8] D.E. Spence, P.N. Kean and W. Sibbett, "60-fsec pulse generation from a self-mode-locked Ti:sapphire laser", Opt. Lett. **16**, 4244 (1991).

[9] D. Strickland and G. Mourou, "Compression of amplified chirped optical pulses", Opt. Commun. **56**, 219-222 (1985).

[10] P. Maine, D. Strickland, P. Bado, M. Pessot, and G. Mourou, "Generation of Ultrahigh Peak Power Pulses by Chirped Pulse Amplification", IEEE J. Quantum Electron. **24**, 398403 (1988).

[11] S. Backus, C.G. Durfee III, M.M. Murnane, and H. Kapteyn, "High power ultrafast lasers", Rev. Sci. Instrum. **69**, 12071223 (1998).

[12] P.F. Moulton, "Spectroscopic and laser characteristics of Ti:Al_2O_3", J. Opt. Soc. Am. B **3**, 125-134 (1986).

[13] A. Sanchez, A.J. Strauss, R.L. Aggarwal, and R.E. Fahey, "Crystal growth, spectroscopy, and laser characteristics of Ti:Al2O3", IEEE J. Quantum Electron. **24**, 995-1002 (1988).

[14] B.F. Gächter and J.A. Koningstein, "Zero phonon transitions and interacting Jahn-Teller phonon energies from the fluorescence spectrum of of a-Al_2O_3:Ti^{3+}", J. Chem. Phys., vol. **60**, 20032006 (1974).

[15] G. F. Albrecht, J.M. Eggleston, and J.J. Ewing, "Measurements of Ti^{3+}:Al_2O_3 as a lasing material", Opt. Commun. **52**, 401404 (1985).

[16] M. Perry, "Crossing the Petawatt Threshold", Sci. Tech. Rev. **12**, 4-11 (1996).

[17] S.A. Akhmanov and R.V. Khokhlov, "Concerning one possibility of amplification of light waves", Sov. Phys. JETP **16**, 252 (1963).

[18] S.A. Akhmanov, V.V. Fadeev, R.V. Khokhlov, A.I. Kovrigin and A.S. Piskarskas, "Observation of parametric amplification in the optical range", JETP Lett. **2**, 191-193 (1965).

[19] C.C. Wang and G.W. Racette, "Measurement of parametric gain accompanying optical difference frequency generation", Appl. Phys. Lett. **6**, 169-171 (1965).

[20] R. H. Kingston, "Parametric amplification and oscillation at optical frequencies", Proc. IRE **50**, 472 (1962).

[21] N. M. Kroll, "Parametric amplification in spatially extended media and application to the design of tuneable oscillators at optical frequencies", Phys. Rev. **127**, 1207-1211 (1962).

[22] T.Wilhelm, J. Piel, and E. Riedle, "Sub-20-fs pulses tunable across the visible from a blue-pumped single-pass noncollinear parametric converter", Opt. Lett. **22**, 1494-1496 (1997).

[23] A. Shirakawa, I. Sakane, and T. Kobayashi, "Pulse-front-matched optical parametric amplification for sub-10-fs pulse generation tunable in the visible and near infrared", Opt. Lett. 23, 1292-1294 (1998).

[24] E. Riedle, M. Beutter, S. Lochbrunner, J. Piel, S. Schenkl, S. Spörlein, and W.Zinth, "Generation of 10 to 50 fs pulses tunable through all of the visible and the NIR", Appl. Phys. B **71**, 457-465 (2000).

[25] A. Baltuska, T. Fuji, and T. Kobayashi, "Visible pulse compression to 4 fs by optical parametric amplification and programmable dispersion control", Opt. Lett. **27**, 306-308 (2002).

[26] J. Piel, M. Beutter, and E. Riedle, "20-50-fs pulses tunable across the near infrared from a blue-pumped noncollinear parametric amplifier", Opt. Lett. **25**, 180182 (2000).

[27] A. Dubietis, G. Jonusauskas, and A. Piskarskas, "Powerful femtosecond pulse generation by chirped and stretched pulse parametric amplification in BBO crystal", Opt. Commun. **88**, 437440 (1992).

[28] A. Piskarskas, A. Stabinis, and A. Yankauskas, "Phase phenomena in parametric amplifiers and generators of ultrashort light pulses", Sov. Phys. Usp. **29**, 869879 (1986).

[29] D. Xue, K. Betzler, H. Hesse and D. Lammers, "Nonlinear optical properties of borate crystals", Sol. State Commun. **114**, 2125 (2000).

[30] I. N. Ross, P. Matousek, M. Towrie, A. J. Langley, and J. L. Collier, "The prospects for ultrashort pulse duration and ultrahigh intensity using optical parametric chirped pulse amplifiers", Opt. Commun. **144**, 125133, (1997).

[31] I. Jovanovic, C.A. Ebbers, and C.P.J. Barty, "Hybrid chirped-pulse amplification", Opt. Lett. **27**, 1622-1624 (2002).

[32] L.J.Waxer, V. Bagnoud, I.A. Begishev, M.J.Guardalben, J.Puth, and J.D. Zuegel, "High-conversion-efficiency optical parametric chirped-pulse amplification system using spatiotemporally shaped pump pulses", Opt. Lett. **28**, 1245-1247 (2003).

[33] N. Ishii, L. Turi, V. S. Yakovlev, T. Fuji, F. Krausz, A. Baltuska, R. Butkus, G. Veitas, V. Smilgevicius, R. Danielius and A. Piskarskas, "Multimillijoule chirped parametric amplification of few-cycle pulses," Opt. Lett. **30**, 567-569, (2005).

[34] S. Witte, R.Th. Zinkstok, A.L. Wolf, W. Hogervorst, W. Ubachs and K.S.E. Eikema, "A source of 2 terawatt, 2.7 cycle laser pulses based on noncollinear optical parametric chirped pulse amplification", Opt. Express **14**, 8168-8177 (2006).

[35] F. Tavella, Y. Nomura, L. Veisz, V. Pervak, A. Marcinkevicius and F. Krausz, "Dispersion management for a sub-10-fs, 10-TW optical parametric chirped-pulse amplifier", Opt. Lett. **32**, 2227-2229 (2007).

[36] R. Butkus, R. Danielius, A. Dubietis, A. Piskarskas and A. Stabinis, "Progress in chirped pulse optical parametric amplifiers", Appl. Phys. B **79**, 693700 (2004).

[37] A. Dubietis, R. Butkus, A.P. Piskarskas, "Trends in chirped pulse optical parametric amplification", IEEE Journ. of Sel. Top. Quantum Electron. **12**, 163172 (2006).

[38] G. Cerullo and S. de Silvestri, "Ultrafast optical parametric amplifiers", Rev. Sci. Instrum. **74**, 1-18 (2003).

[39] M.D. Perry, D. Pennington, B.C. Stuart, G. Tietbohl, J.A. Britten, C. Brown, S. Herman, B. Golick, M. Kartz, J. Miller, H.T. Powell, M. Vergino, and V. Yanovsky, "Petawatt laser pulses", Opt. Lett. **24**, 160-162 (1999).

[40] C.N. Danson *et al.*, "Vulcan Petawatt - an ultra-high-intensity interaction facility", Nucl. Fusion **44**, 239-246 (2004).

[41] Y. Kitagawa, H. Fujita, R. Kodama, H. Yoshida, S. Matsuo, T. Jitsuno, T. Kawasaki, H. Kitamura, T. Kanabe, S. Sakabe, K. Shigemori, N. Miyanaga, and Y. Izawa, "Prepulse-free petawatt laser for a fast ignitor", IEEE J. Quantum Electron. **40**, 281-293 (2004).

[42] X. Yang, Z. Xu, Y. Leng, H. Lu, L. Lin, Z. Zhang, R. Li, W. Zhang, D. Yin, and B. Tang, "Multiterawatt laser system based on optical parametric chirped pulse amplification", Opt. Lett. **27**, 1135-1137 (2007).

[43] I. N. Ross, J. L. Collier, P. Matousek, C. N. Danson, D. Neely, R. M. Allott, D. A. Pepler, C. Hernandez- Gomez, and K. Osvay, "Generation of terawatt pulses by use of optical parametric chirped pulse amplification", Appl. Opt. **39**, 2242-2427 (2000).

[44] V.V. Lozhkarev, G.I. Freidman, V.N. Ginzburg, E.V. Katin, E.A. Khazanov, A.V. Kirsanov, G.A. Luchinin, A.N. Mal'shakov, M.A. Martyanov, O.V. Palashov, A.K. Poteomkin, A.M. Sergeev, A.A. Shaykin, S.G. Garanin, S. Sukharev, N.N. Rukavishnikov, V. Charukhchev, R.R. Gerke, V.E. Yashin and I.V. Yakovlev "200 TW 45 fs laser based on optical parametric chirped pulse amplification", Opt. Express **14**, 446-454 (2006).

[45] C. Manzoni, D. Polli, G. Cirmi, D. Brida, S. De Silvestri, and G. Cerullo, "Tunable few-optical-cycle pulses with passive carrier-envelope phase stabilization from an optical parametric amplifier", Appl. Phys. Lett. **90**, 171111 1-3 (2007).

[46] A. Baltuska, T. Fuji and T. Kobayashi, "Self-referencing of the carrier-envelope slip in a 6-fs visible parametric amplifier", Opt. Lett. **27**, 1241-1243 (2002).

[47] P. Gibbon, "Short pulse laser interactions with matter", Imperial College Press, (2005)

[48] J. Faure, Y. Glinec, A. Pukhov, S. Kiselev, S. Gordienko, E. Lefebvre, J.P. Rousseau, F. Burgy and V.A. Malka, "Laser-plasma accelerator producing monoenergetic electron beams", Nature **431**, 541-544 (2004).

[49] S.P.D. Mangles, C.D. Murphy, Z. Najmudin, A.G.R. Thomas, J.L. Collier, A.E. Dangor, E.J. Divall, P.S. Foster, J.G.Gallager, C.J. Hooker, D.A. Jaroszinsky, A.J. Lagley, W.B. Mori, P.A. Norreys, F.S. Tsung, R.Viskup, B.R.Walton and K.Krushelnick, "Monoenergetic beams of relativistic electrons from intense laser-plasma interactions", Nature **431**, 535-538 (2004).

[50] C.G.R. Geddes, Cs. Toth, J. van Tilborg, E. Esaray, C.B. Schroeder, D. Bruhwiler, C. Nieter, J. Cary and W.P. Leemans, "High-quality electron beams from a laser wakefield accelerator using plasma-channel guiding", Nature **431**, 541 (2004).

[51] M. Geissler, J. Schreiber, and J. Meyer-ter-Vehn, ”Bubble accelaration of electrons with few-cycle laser pulses”, New J. Phys. **8**, 186-199 (2006).

[52] W. P. Leemans, B. Nagler, A.J. Gonsalves, Cs. TohT, K. Nakamura, C.G.R. Geddes, E. Esarey, C. B. Schröder and S.M. Hooker, ”GeV electron beams from a centimetre-scale accelerator”, Nature Physics **2**, 696-699 (2006).

[53] R.A. Snavely, M.H. Key, S.P. Hatchett, T.E. Cowan, M. Roth, T.W. Phillips, M.A. Stoyer, E.A. Henry, T.C. Sangster, M.S. Singh, S. C. Wilks, A. MacKinnon, A. Offenberger, D.M. Pennington, K. Yasuike, A.B. Langdon, B.F. Lasinski, J. Johnson, M.D. Perry, and E.M. Campbell, ”Intense high-energy proton beams from petawatt-laser irradiation of solids”, Phys. Rev. Lett. **85**, 2945-2948 (2000).

[54] V. Malka, S. Fritzler, F.E. Lefebvre, E. dHumieres, R. Ferrand , G. Grillon, C. Albaret, S. Meyroneinc, J.P. Chambaret, A. Antonetti and D. Hulin, ”Practicability of protontherapy using compact laser systems”, Med. Phys. **31**, 1587-1592 (2004).

[55] L. Robson, P.T. Simpson, R.J. Clarke, K.W.D. Ledingham, F. Lindau, O. Lundh, T. McCanny, P. Mora, D. Neely, C.G. Wahlström, M. Zepf AND P. McKenna, ”Scaling of proton acceleration driven by petawatt-laser plasma interactions”, Nat. Phys. **3**, 58-62 (2006).

[56] S.Nakai and K.Mima, ”Laser driven inertial fusion energy: present and prospective”, Rep. Prog. Phys. **67**, 321-349 (2004).

[57] M. Tabak, J. Hammer, M.E. Glinsky, W.L. Kruer, S.C. Wilks, J. Woodworth, E.M. Campbell, and M.D. Perry, ”Ignition and high gain with ultrapowerful lasers”, Phys. Plasmas **1**, 1626-1634 (1994).

[58] M. Hentschel, R. Kienberger, Ch. Spielmann, G. A. Reider, N. Milosevic, T. Brabec, P. Corkum, U. Heinzmann, M. Drescher and F. Krausz, ”Attosecond metrology,” Nature 414, 509-513 (2001).

[59] M. Drescher, M. Hentschel, R. Kienberger, M. Uiberacker, V. Yakovlev, A. Scrinzi, Th. Westerwalbesloh, U. Kleineberg, U. Heinzmann and F. Krausz, ”Time-resolved atomic inner-shell spectroscopy,” Nature 419, 803-807 (2002).

[60] A. Baltuska, Th. Udem, M. Uiberacker, M. Hentschel, E. Goulielmakis, Ch. Gohle, R. Holzwarth, V.S. Yakovlev, A. Scrinzi, T.W. Hänsch and F. Krausz, ”Attosecond control of electronic processes by intense light fields,” Nature 421, 611-615 (2003).

[61] R. Kienberger, E. Goulielmakis, M. Uiberacker, A. Baltuska, V. Yakovlev, F. Bammer, A. Scrinzi, Th. Westerwalbesloh, U. Kleineberg, U. Heinzmann, M. Drescher and F. Krausz, ”Atomic transient recorder,” Nature 427, 817-821 (2004).

[62] M.F. Kling, Ch. Siedschlag, A.J. Verhoef, J.I. Khan, M. Schultze, Th. Uphues, Y. Ni, M. Uiberacker, M. Drescher, F. Krausz, M.J.J. Vrakking, "Control of Electron Localization in Molecular Dissociation," Science 312, 246-248 (2006).

[63] G. Sansone, E. Benedetti, F. Calegari, C. Vozzi, L. Avaldi, R. Flammini, L. Poletto, P. Villoresi, C. Altucci, R. Velotta, S. Stagira, S. De Silvestri, M. Nisoli, "Isolated Single-Cycle Attosecond Pulses," Science 314, 443-446 (2006).

[64] G.D. Tsakiris, K. Eidmann, J. Meyer-ter-Vehn and F. Krausz, "Route to intense single attosecond pulses", New J. Phys. **8**, 19-39 (2006)

[65] P. B. Corkum, "Plasma perspective on strong field multiphoton ionization", Phys. Rev. Lett. **71**, 1994-1997 (1993).

[66] M. Lewenstein, P. Balcou, M.Y. Ivanov, A. LHuillier, and P.B. Corkum, "Theory of high-harmonic generation by low-frequency laser fields", Phys. Rev. A **49**, 2117-2132 (1994).

[67] J. Seres, E. Seres, A.J. Verhoef, G. Tempea, C. Streli, P. Wobrauschek, V. Yakovlev, A. Scrinzi, C. Spielmann and F. Krausz, "Source of coherent kiloelectronvolt X-rays", Nature **433**, 596 (2005).

[68] Ch. Spielmann, N.H. Burnett, S. Sartania, R. Koppitsch, M. Schnü rer, C. Kan, M. Lenzner, P. Wobrauschek, F. Krausz, "Generation of coherent X-rays in the water window using 5- femtosecond laser pulses", Science **278**, 661-664 (1997).

[69] J.A. Armstrong, N. Bloembergen, J. Ducuing and P.S. Perhan, "Interactions between light waves in a nonlinear dielectric", Phys. Rev. **127**, 1918-1939 (1962).

[70] Y. Shen: The principles of nonlinear optics.
Berkeley California: John Wiley and Sons (1984).

[71] I.N. Ross, P. Matousek, G.H.C. New, K. Osvay, "Analysis and optimization of optical parametric chirped pulse amplification", J. Opt. Soc. Am. B **19**, 29452956 (2002).

[72] I. Jovanovic: Optical parametric amplification for high peak and average power.
PhD-Thesis at LLNL (1984).

[73] A.L. Oien, I.T. McKinnie, P. Jain, N.A. Russell, D.M. Warrington and L.A.W. Gloster, "Efficient, low-threshold collinear and noncollinear β-barium borate optical parametric oscillators", Opt. Lett. **22**, 859861 (1997).

[74] A. Dubietis, R. Danielius, G. Tamošauskas, and A. Piskarskas, "Combining effect in a multiple-beam-pumped optical parametric amplifier", J. Opt. Soc. Am. B **15**, 11351139 (1998).

[75] P. Kumbhakar, T. Kobayashi, "Nonlinear optical properties of $Li_2B_4O_4$ (LB4) crystal for the generation of tunable ultra-fast laser radiation by optical parametric amplification", Appl. Phys. B **78**, 165-170, (2004)

[76] O.S. Kushnir, Y.V. Burak, O.A. Bevz and I.I. Polovinko, "Crystal optical studies of lithium tetraborate", J. Phys.: Condens. Matt. **11**, 83138327, (1999)

[77] J. Kroupa,D. Kasprovicz, A. Majkrowki, E. Michalski and M. Drozdowski, "Optical Properties of Bismuth Triborate (BIBO) Single Crystals", Ferroelectrics: Taylor & Francis **318**, 7782, (2005)

[78] D. Xue and S. Zhang, "Structure and non-linear optical properties of β-Barium Borate", Acta. Cryst. **54**, 652-656, (1998)

[79] H. Hellwig, J. Liebertz and L. Bohaty, "Linear optical properties of the monoclinic bismuth borate BiB_3O_3", Journ. of Appl. Phys. **88**, 240-244, (2000)

[80] N. Boeuf, D. Branning, I. Chaperot, E. Dauler, S. Guerin, G. Jaeger, A. Muller, and A. L. Migdall, "Calculating characteristics of non-collinear phase-matching in uniaxial and biaxial crystals", Opt. Eng. **39**, 10161024 (2000).

[81] V.G. Dmitriev, G.G. Gurzadyan and D.N. Nikogosyan: Handbook of nonlinear optical crystals: Springer (2006).

[82] L. Hongjun, Z. Wei, C. Guofu, W. Yishan, C. Zhao and R. Chi, "Investigation of spectral bandwidth of optical parametric amplification", Appl. Phys. B, DOI: 10.1007/s00340-004-1567-6 (2004).

[83] J.A. Fülöp, Zs. Major, B. Horvath, **F. Tavella**, A. Baltuska, F. Krausz, "Shaping of picosecond pulses for pumping optical parametric amplification" Appl. Phys. B **87**, 79-84 (2006).

[84] F. Tavella, A. Marcinkevicius and F. Krausz, "Inverstigation of the superfluorescence generation in a multiterawatt OPCPA," New J. Phys. **8**, 1-11, (2006).

[85] G. Arisholm, J. Biegert, P. Schlup, C.P. Hauri, and U. Keller, "Ultra-broadband chirped-pulse optical parametric amplifier with angularly dispersed beams", Opt. Express **12**, 518530 (2004).

[86] L. Cardoso and G. Figueira, "Bandwidth increase by controlled angular dispersion of signal beam in optical parametric amplification", Opt. Express **12**, 3108-3113 (2004).

[87] E. Zeromskis, A. Dubietis, G. Tamosauskas, and A. Piskarskas, "Gain bandwidth broadening of the continuum-seeded optical parametric amplifier by use of two pump beams", Opt. Commun. **203**, 435-440 (2002).

[88] C. Wang, Y. Leng, B. Zhao, Z. Zhang, and Z. Xu, "Extremely broad gain spectra of two-beam-pumped optical parametric chirped-pulse amplifier", Opt. Commun. **237**, 169-177 (2004).

[121] S. Witte, R.T. Zinkstok, W. Hogervorst, K.S.E. Eikema, "Numerical simulations for performance optimization of a few-cycle terawatt NOPCPA system", Appl. Phys. B **87**, 677-684 (2007).

[90] R. A. Baumgartner and R. L. Byer, Optical Parametric Amplification, IEEE J. Quantum Electron. **15**, 432444 (1979)

[91] N. Bloembergen, Nonlinear optics. New York: W.A. Benhamin Inc, 1965.

[92] R. L. Sutherland, Handbook of Nonlinear Optics. New York: Marcel Dekker, Inc., 1996.

[93] G. Reider: Photonik, eine Einführung in die Grundlagen.
Wien: Springer WienNewYork 1997.

[94] G. Arisholm, "General numerical methods for simulating second-order nonlinear interactions in birefringent media", J. Opt. Soc. Am. B **14**, 25432549 (1997).

[95] A. Kurtanaitis, A. Dementjev and F. Ivanauskas, "Modeling of Pulse Propagation Factor Changes in Type II Second-Harmonic Generation", Nonlin. Analysis: Modelling and Control **6** 51, (2001)

[96] A. Picozzi and M. Haelterman, "Influence of walk-off, dispersion, and diffraction on the coherence of parametric fluorescence", Phys. Rev. E **63**, 056611 1-11, (2001).

[97] A. Gatti, H. Wiedemann, L.A. Lugiato, I. Marzoli, G. Oppo and S.M. Barnett, "Langevin treatment of quantum fluctuations and optical patterns in optical parametric oscillators below threshold", Physical Review A **56**, 877-897, (1997)

[98] F. Tavella, K. Schmid, N. Ishii, A. Marcinkevicius, L. Veisz and F. Krausz, "High-dynamic range pulse-contrast measurements of a broadband optical parametric chirped-pulse amplifier", Appl. Phys. B DOI: 10.1007/s00340-005-1966-3, (2005)

[99] D.A. Kleinman, "Theory of optical parametric noise", Phys. Rev. **174**, 1027-1041, (1968).

[100] R.J. Glauber, "Coherent and incoherent states of radiation.pdf", Phys. Rev. **131**, 2766-2788, (1963)

[101] W.H. Louisell, A. Yariv, and A.E. Siegman, "Quantum fluctuations and noise in parametric processes. I", Phys. Rev. **124**, 1646-1654 (1961).

[102] B.R. Mollow and R.J. Glauber, "Quantum theory of parametric amplification. I", Phys. Rev. **160**, 1076-1096 (1967).

[103] T.G. Giallorenzi and C.L. Tang, "Quantum theory of spontaneous parametric scattering of intense light", Phys. Rev. **166**, 225-233 (1968).

[104] L. Carrion and J.-P. Girardeau-Montaut, "Development of a simple model for optical parametric generation", J. Opt. Soc. Am. B **17**, 78-83, (2000).

[105] G. Arisholm, "Quantum noise initiation and macroscopic fluctuations in optical parametric oscillators", J. Opt. Soc. Am. B **16**, 117-127, (1999).

[106] E.L. Bolda, R.Y. Chiao, J.C. Garrison, "Superfluorescence in a continuously pumped medium", Phys. Rev. A **52**, 3308-3315, (1995).

[107] N. Forget, A. Cotel, E. Brambrink, P. Audebert, C. Le Blanc, A. Jullien, O. Albert and G. Cheriaux "Pump-noise transfer in optical parametric chirped-pulse amplification", Opt. Lett. **30**, 2921-2923, (2005)

[108] E.J. Grace, C.L. Tsangaris, G.H.C. New, "Competing processes in optical parametric chirped pulse amplification", Opt. Comm. **261**, 255-230, (2006).

[109] R. Danielius, A. Piskarskas, A. Stabinis, G. P. Banfi, P. Di Trapani and R. Righini, "Traveling-wave parametric generation of widely tunable, highly coherent femtosecond light pulses", J. Opt. Soc. Am. B **10**, 2222-2232, (1993)

[110] L. You, J. Cooper and M. Trippenbach, "Alternative treatment for the initiation of superfluorescence", J. Opt. Soc. Am. B **8**, 1139-1148, (1991).

[111] S.E. Harris, M.K. Oshman, and R.L. Byer, "Observation of tunable optical parametric fluorescence", Phys. Rev. Lett. **18**, 732-734 (1967).

[112] R.L. Byer and S.E. Harris, "Power and bandwidth of spontaneous parametric emission", Phys. Rev. **168**, 1064-1068 (1968).

[113] A. Kasper, and K.J. Witte, "Contrast and phase of ultrashort laser pulses from Ti:sapphire ring and Fabry Perot resonators based on chirped mirrors", J. Opt. Soc. Am. B **9**, 2490-2495, (1998)

[114] A. Braun, J. V. Rudd, H. Cheng, and G. Mourou, D. Kopf, I. D. Jung, K. J. Weingarten, and U. Keller, "Characterization of short-pulse oscillators by means of a high-dynamic-range autocorrelation measurement" Opt. Lett. **18**, 1889-1891, (1995)

[115] A. Cotel, A. Jullien, N. Forget, O. Albert, G. Cheriaux, and C. Le Blanc, "Nonlinear temporal pulse cleaning of a 1-μm optical parametric chirped-pulse amplification system", Appl. Phys. B **83**, 7-10, (2006)

[116] G. Doumy, F. Quere, O. Gobert, M. Perdrix, Ph. Martin, P. Audebert, J. C. Gauthier, J.-P. Geindre, and T. Wittmann, "Complete characterization of a plasma mirror for the production of high-contrast ultraintense laser pulses", Phys. Rev. E **69**, 026402, (2004)

[117] T. S. Sosnowski, P. B. Stephens, and T. B. Norris , "Production of 30-fs pulses tunable throughout the visible spectral region by a new technique in optical parametric amplification", Opt. Lett. **21**, 140-142, (1996)

[118] K. Kondo, H. Maeda, Y. Hama, S. Morita, A. Zoubir, R. Kodama, K. A. Tanaka, Y. Kitagawa, and Y. Izawa, "Control of amplified optical parametric fluorescence for hybrid chirped-pulse amplification", J. Opt. Soc. Am. B **2**, 231-235, (2005)

[119] V. Bagnoud, J.D. Zuegel, N. Forget and C. Le Blanc, "High-dynamic-range temporal contrast measurement of short pulses amplified by OPCPA", Opt. Express **15**, 5504-5511, (2007)

[120] K. Osvay, M. Csatari, I. N. Ross, A. Persson and C.G. Wahlström , "On the temporal contrast of high intensity femtosecond laser pulses", Laser and Particle Beams **23**, 327-332, (1993)

[121] S. Witte, R.T. Zinkstok, W. Hogervorst and K.S.E. Eikema, "Numerical simulations for performance optimization of a few-cycle terawatt NOPCPA system", Appl. Phys. B **87**, 677-684 (2007)

[122] T.Fuji, A.Unterhuber, V.S.Yakovlev, G.Tempea, A.Stingl, F.Krausz and W.Drexler, "Generation of smooth, ultra-broadband spectra directly from a prism-less Ti:sapphire laser," Appl.Phys. B **77**, 125-128 (2003).

[123] L. Cardoso, I. N. Ross, J. L. Collier, O. Chekhlov, "Design and implementation of an oscillator for OPCPA", Las. Scie. and Dev. CLF Ann. Rep. (2002/2003).

[124] R. Ell, U. Morgner, F. X. Krtner, J. G. Fujimoto, E. P. Ippen, V. Scheuer, G. Angelow, T. Tschudi, M. J. Lederer, A. Boiko, and B. Luther-Davies, "Generation of 5-fs pulses and octave-spanning spectra directly from a Ti:sapphire laser", Opt. Lett. **26**, 373-375 (2001).

[125] A. Stingl, Ch. Spielmann, F. Krausz and R. Szipocs "Generation of 11-fs pulses from a Ti:sapphire laser without the use of prisms", Opt. Lett. **3**, 204-206 (1994).

[126] T. Brabec, C. Spielmann, P.F. Curley, and F. Krausz, "Kerr lens mode locking", Opt. Lett. **17**, 12921294 (1992).

[127] N. Ishii, C.Y. Teisset, T. Fuji, S. Köhler, K. Schmid, L. Veisz, A. Baltuska and F. Krausz, "Seeding of an eleven femtosecond optical parametric chirped pulse amplifier and its Nd3+ picosecond pump laser from a single broadband Ti:Sapphire oscillator," IEEE J. Sel. Top. Quantum Electron. **12**, 173-180 (2006).

[128] D.J. Jones, S.A. Diddams, J.K. Ranka, A. Stentz, R.S. Windeler, J.L. Hall, and S.T. Cundiff, "Carrier-envelope phase control of femtosecond mode-locked lasers and direct optical frequency synthesis", Science **288**, 635-639 (2000).

[129] S.T. Cundiff, "Phase stabilization of ultrashort optical pulses", J. Phys. D **35**, R43-R59 (2002).

[130] A. Apolonski, A. Poppe, G. Tempea, Ch. Spielmann, Th. Udem, R. Holzwarth, T.W. Hnsch and F. Krausz, "Controlling the phase evolution of few-cycle light pulses", Phys. Rev. Lett. **85**, 740-743 (2000).

[131] C.P. Hauri, P. Schlup, G. Arisholm, J. Biegert, and U. Keller, "Phase-preserving chirpedpulse optical parametric amplification to 17.3 fs directly from a Ti:sapphire oscillator", Opt. Lett. **29**, 13691371 (2004).

[132] T. Fuji, J. Rauschenberger, C. Gohle, A. Apolonski, T. Udem, V. Yakovlev, G. Tempea, T. Hnsch and F. Krausz, "Attosecond control of optical waveforms", N. J. Phys. **7**, 1-9 (2005).

[133] T. Fuji, J. Rauschenberger, A. Apolonski, V. S. Yakovlev, G. Tempea, T. Udem, C. Gohle, T. W. Hnsch, W. Lehnert, M. Scherer and F. Krausz, "Monolithic carrier-envelope phase-stabilization scheme", Opt. Lett. **3**, 332-334 (2005).

[134] S. T. Cundiff, W. H. Knox, E. P. Ippen and H. A. Haus, "Frequency-dependent mode size in broadband Kerr-lens mode locking", Opt. Lett. **21**, 662-664 (1996).

[135] V. L. Kalashnikov, E. Sorokin, and I. T. Sorokina, "Multipulse Operation and Limits of the Kerr-Lens Mode-Locking Stability", IEEE J. Sel. Top. Quant. Elec. **39**, 323-336 (2003).

[136] M. Nisoli, S. De Silvestri, and O. Svelto, "Generation of high energy 10 fs pulses by a new pulse compression technique", Appl. Phys. Lett. **68**, 2793-2794 (1996).

[137] E. Yablonovitch, "Self-phase modulation and short-pulse generation from laser-breakdown plasmas", Phys. Rev. A **10**, 1888-1895 (1974).

[138] W.M. Wood, C.W. Siders, and M.C. Downer, "Measurement of femtosecond ionization dynamics of atmospheric density gases by spectral blueshifting", Phys. Rev. Lett. **67**, 3523-3526 (1991).

[139] G. I. Petrov, O. Albert, J. Etchepare, S. M. Saltiel, "Cross-polarized wave generation by effective cubic nonlinear optical interaction", Opt. Lett. **26**, 355-357 (2001).

[140] V. Chvykov, P. Rousseau, S. Reed, G. Kalinchenko, and V. Yanovsky, "Generation of 10^{11} contrast 50 TW laser pulses", Opt. Lett. **31**, 1356-1358 (2006).

[141] A. Jullien, S. Kourtev, O. Albert, G. Cheriaux, J. Etchepare, N. Minkovski, S.M. Saltiel, "Highly efficient temporal cleaner for femtosecond pulses based on cross-polarized wave generation in a dual crystal scheme", Appl. Phys. B **84**, 409-414 (2006).

[142] C. Y. Teisset, N. Ishii, T. Fuji, T. Metzger, S. Köhler, R. Holzwarth, A. Baltuska, A. M. Zheltikov and F. Krausz, "Soliton-based pump seed synchronization for few-cycle OPCPA," Opt. Express **13**, 6550-6557 (2005).

[143] P. Russell, "Photonic crystal fibers", Science **299**, 358-362 (2003).

[144] G.P. Agrawal, "Nonlinear fiber optics", New York : Academic Press - 3rd ed, (2001).

[145] A.E. Siegman: Lasers.
Sausalito (CA): University science books 1986.

[146] D.M. Gaudiosi, A.L. Lytle, P. Kohl, M.M. Murnane, H.C. Kapteyn, and S. Backus, "11-W average power Ti:sapphire amplifier system using downchirped pulse amplification", Opt. Lett. **14**, 2665 (2004).

[147] S. Kane and J. Squier, "Grism-pair stretchercompressor system for simultaneous second- and third-order dispersion compensation in chirped-pulse amplification", J. Opt. Soc. Am. B **14**, 661 (1997).

[148] E.A. Gibson, D.M. Gaudiosi, H.C. Kapteyn, R. Jimenez, S. Kane, R. Huff, Ch. Durfee, and J. Squier, "Efficient reflection grisms for pulse compression and dispersion compensation of femtosecond pulses", Opt. Lett. **31**, 3363-3365 (2006).

[149] F. Verluise, V. Laude, Z. Cheng, Ch. Spielmann and P.Tournois, "Amplitude and phase control of ultrashort pulses by use of an acousto-optic programmable dispersive filter: pulse compression and shaping", Opt. Lett. **25**, 575-577 (2000).

[150] E.B. Treacy, "Optical Pulse Compression With Diffraction Gratings", IEEE J. Quantum Electr. **5**, 454-458 (1969).

[151] S. Wise, V. Quetschke, A.J. Deshpande, G. Mueller, D.H. Reitze, D.B. Tanner, B.F. Whiting, Y. Chen, A. Tunnermann, E. Kley, and T. Clausnitzer, "Phase Effects in the Diffraction of Light: Beyond the Grating Equation" Phys. Rev. Lett. **95**, 013905 (2005).

[152] H.J. Eichler, A. Haase, R. Menzel and A. Siemoneit, "Thermal lensing and depolarization in a 1 I highly pumped Nd:YAG laser amplifier", J. Phys. D Appl. Phys. **26**, 1884-1891 (1993).

[153] I. Moshe and S. Jackel, "Correction of thermally induced birefringence in doublerod laser resonators comparison of various methods", Opt. Commun. **214**, 315-325 (2002).

[154] W.A. Clarkson, N.S. Felgate, and D.C. Hanna, "Simple method for reducing the depolarization loss resulting from thermally induced birefringence in solid-state lasers", Opt. Lett. **24**, 820-822 (1999).

[155] Q.N. Kugler, H. Weber, S. Dong, N. Moller and U. Wittrock, "A novel approach for compensation of birefringence in cylindrical Nd:YAG rods", Opt. and Quant. Electr. **28**, 57-69 (1996).

[156] N. Kugler, S. Dong, Q. Lü, and H. Weber, "Investigation of the misalignment sensitivity of a birefringence-compensated two-rod Nd:YAG laser system", Appl. Opt. **36**, 9359 (1997).

[157] F. Tavella, A. Marčinkevicius and F. Krausz, "90 mJ parametric chirped pulse amplification of 10 fs pulses", Opt. Express **14**, 12822-12827 (2006).

[158] C. Dorrer, "Influence of the calibration of the detector on spectral interferometry", J. Opt. Soc. Am. B **16**, 1160-1168 (1999).

[159] C. Dorrer and I.A. Walmsley, "Accuracy criterion for ultrashort pulse characterization techniques: application to spectral phase interferometry for direct electric field reconstruction", J. Opt. Soc. Am. B **19**, 1019-1029 (2002).

[160] C. Dorrer and I.A. Walmsley, "Precision and consistency criteria in spectral phase interferometry for direct electric-field reconstruction", J. Opt. Soc. Am. B **19**, 1030-1038 (2002).

[161] C. Iaconis, V. Wong, and I. A. Walmsley, "Direct Interferometric Techniques for Characterizing Ultrashort Optical Pulses", IEEE J. Sel. Top. Quantum Electron. **4**, 285-294 (1998).

[162] C. Iaconis and I. A. Walmsley, "Spectral phase interferometry for direct electric-field reconstruction of ultrashort optical pulses", Opt. Lett. **23**, 792-794 (1998).

[163] T.M. Shuman, M.E. Anderson, J. Bromage, C. Iaconis, L. Waxer and I.A. Walmsley, "Real-time SPIDER: ultrashort pulse characterization at 20 Hz", Opt. Express **5**, 134-143 (1999).

[164] W. Kornelis, J. Biegert, and J. W. G. Tisch, M. Nisoli, G. Sansone, C. Vozzi, S. De Silvestri and U. Keller, "Single-shot kilohertz characterization of ultrashort pulses by spectral phase interferometry for direct electric-field reconstruction", Opt. Lett. **28**, 281-283 (2003).

[165] C. Dorrer, B. de Beauvoir, C. Le Blanc, S. Ranc, J.-P. Rousseau, P. Rousseau, J.-P. Chambaret and F. Salin, "Single-shot real-time characterization of chirped-pulse amplification systems by spectral phase interferometry for direct electric-field reconstruction", Opt. Lett. **24**, 1644-1646 (1999).

[166] T.A. Planchon, J.-P. Rousseau, F. Burgy, G. Cheriaux and J.-P. Chambaret, "Adaptive wavefront correction on a 100-TW/10-Hz chirped pulse amplification laser and effect of residual wavefront on beam propagation", Opt. Comm. **252**, 222228 (2005).

[167] M. Nicolle, T. Fusco, G. Rousset, and V. Michau, "Improvement of ShackHartmann wave-front sensor measurement for extreme adaptive optics", Opt. Lett. **29**, 2743-2745 (2004).

[168] T. Tajima and J.M. Dawson, "Laser electron acceleration", Phys. Rev. Lett. **43**, 267-270 (1979).

[169] C. Gahn, G.D. Tsakiris, A. Pukhov, J. Meyer-ter-Vehn, G. Pretzler, P. Thirolf, D. Habs, and K.J. Witte, "Multi-MeV Electron Beam Generation by Direct Laser Acceleration in High-Density Plasma Channels", Phys. Rev. Lett. **83**, 4772-4775 (1999).

[170] A. Ting, C.I. Moore, K. Krushelnick, C. Manka, E. Esarey, P. Sprangle, R. Hubbard, H. R. Burris, R. Fischer, and M. Bainec, "Plasma wakefield generation and electron acceleration in a self-modulated laser wakefield accelerator experiment", Phys. Plasmas **4**, 1889-1899 (1997).

[171] R. Wagner, S.Y. Chen, A. Maksimchuk, and D. Umstadter, "Electron Acceleration by a Laser Wakefield in a Relativistically Self-Guided Channel", Phys. Rev. Lett. **78**, 3125-3128 (1997).

[172] E. Esarey, P. Sprangle, J. Krall, A. Ting, "Overview of plasma-based accelerator concepts", Plasm. Sci. **24**, 252-288 (1996).

[173] A. Pukhov and J. Meyer-Ter-Vehn, "Laser wake field acceleration: the highly non-linear broken-wave regime", Appl. Phys. B **74**, 355-361 (2002).

[174] V. Malka, J. Faure, Y. Glinec, A. Pukhov and J.-P. Rousseau, "Monoenergetic electron beam optimization in the bubble regime", Phys. of Plasmas **12**, 056702:1-8 (2005).

[175] E. Miuraa, K. Koyama, S. Kato, N. Saito, M. Adachi, Y. Kawada ,T. Nakamura and M. Tanimoto, "Demonstration of quasi-monoenergetic electron-beam generation in laser-driven plasma acceleration", Appl. Phys. Lett. **86**, 251501:1-3 (2005).

[176] B. Hidding, K.U. Amthor, B. Liesfeld, H. Schwörer, S. Karsch, M. Geissler, L. Veisz, K. Schmid, J.G. Gallacher, S.P. Jamison, D. Jaroszynski, G. Pretzler, and R. Sauerbrey, "Generation of Quasimonoenergetic Electron Bunches with 80-fs Laser Pulses", Phys. Rev. Lett. **96**, 105004:1-4 (2006).

[177] S.P.D. Mangles, A.G.R. Thomas, C. Lundh, F. Lindau, M.C. Kaluza, A. Persson, C.G. Wahlstrm, K. Krushelnickd and Z. Najmudin, "On the stability of laser wakefield electron accelerators in the monoenergetic regime", Phys. of Plasmas **14**, 056702:1-7 (2007).

[178] J. Faure, C. Rechatin, A. Norlin, A. Lifschitz, Y. Glinec and V. Malka, "Controlled injection and acceleration of electrons in plasma wakefields by colliding laser pulses", Nature **14**, 737-739 (2006).

[179] S. Gordienko and A. Pukhov, "Scalings for ultrarelativistic laser plasmas and quasimonoenergetic electrons", N.J. Phys. **12**, 043109, (2005).

[180] S.P.D. Mangles, A.G.R. Thomas, M.C. Kaluza, O. Lundh, F. Lindau, A. Persson, Z. Najmudin, C.G. Wahlström, C.D. Murphy, C. Kamperidis, K.L. Lancaster, E. Divall and K. Krushelnick, "Effect of laser contrast ratio on electron beam stability in laser wakefield acceleration experiments", Plasma Phys. Control. Fusion **48**, B83B90 (2006).

[181] Schott AG, "Optischer Glaskatalog - Datenblätter", http://www.schott.com/optics_devices/german/download/datasheet_all.pdf

[182] M. Bass, "Handbook of optics", New York: McGraw Hill, (1995)

[183] N. Uchida, "Optical properties of single-crystal paratellurite (TeO_2)", Phys. Rev. B **4**, 3736-3746 (1971)

[184] K. Kato, "Second-harmonic generation to 2048 $\AA$ in beta-BaB_2O_4", IEEE J. Quantum Electron. **22**, 1013-1014 (1986).

[185] K. Kato, "Tunable UV generation to 0.2325 m in LiB_3O_5", IEEE J. Quantum Electron. **26**, 1173-1175 (1990)

[186] E.D. Filer, C.A. Morrison, G.A.Turner, and N.P. Barnes, OSA Proceedings on Advanced Solid-State Lasers **6**, 354-362 (1990).

[187] B. Edlen, "Dispersion of standard air", JOSA **43**, 339344 (1953)

Curriculum Vitae

2004 - 2007	Graduate student at **Max-Planck-Institute of Quantum Optics** Group of Prof. F. Krausz - Laboratory for Attosecond and High-Field Physics (Munich, Germany) Title: Multiterawatt few-cycle pulse OPCPA for applications in high-field physics
2004	Diploma thesis at **Technische Universität Wien** Photonic Institute (Vienna, Austria) Title: Active pump laser synchronization for parametric pulse amplification
1997 - 2004	**Technische Universität Wien** Fakultät für Elektrotechnik Studienzweig Automatisierungs- und Regelungstechnik Schwerpunktkatalog K ”Photonik, Optoelektronik, Laser” (Vienna, Austria)
1994 - 1997	**”Max Valier”** Fachrichtung Elektronik Gewerbeoberschule (Bozen, Italy)
1992 - 1994	**”J. Ph. Fallmerayer”** Technisches Biennium Gymnasium (Brixen, Italy)
14.12.1978	Date of birth

List of publications

The thesis is based on following publications

- **F. Tavella**, K. Schmid, N. Ishii, A. Marcinkevicius, L. Veisz and F. Krausz, ”High-dynamic range pulse-contrast measurements of a broadband optical parametric chirped-pulse amplifier” Appl. Phys. B **81**, 753-756 (2005).
- A. Marcinkevicius, **F. Tavella**, and F. Krausz, ”Development of a multi-terawatt ultrabroadband optical parametric chirped pulse amplifier” Proceedings of the XV Ultrafast Phenomena Conference (2006).
- **F. Tavella**, A. Marcinkevicius, and F. Krausz, ”Investigation of the superfluorescence and signal amplification in an ultrabroadband multiterawatt optical parametric chirped pulse amplifier system”, N.J. Phys. **8**, 219-230 (2006).
- J.A. Fülöp, Zs. Major, B. Horvath, **F. Tavella**, A. Baltuska, F. Krausz, ”Shaping of picosecond pulses for pumping optical parametric amplification” Appl. Phys. B **87**, 79-84 (2006).
- F. **Tavella**, A. Marcinkevicius, and F. Krausz, ”90 mJ parametric chirped pulse amplification of 10 fs pulses”, Opt. Express **14**, 12822-12827 (2006).
- **F. Tavella**, Y. Nomura, V. Pervak, L. Veisz, A. Marcinkevicius and F. Krausz, ”Dispersion management for a sub-10-fs, 10-TW optical parametric chirped-pulse amplifier”, Opt. Lett. **32**, 2227-2229 (2007).

Conference contributions

- CLEO Europe/EQEC, June 2005 - München

  A. Marcinkevicius, **F. Tavella**, N. Ishii, A. Baltuka, T. Fuji, L. Veisz, K. Schmid, K. Witte R. Danielius, J. Kolenda, A. Michailovas and F. Krausz, "Development of a broadband high-power optical parametric chirped pulse amplification system"

- CLEO-QELS, May 2006 - Long Beach CA

  F. Tavella, A. Marcinkevicius and F. Krausz, "Development of a Multi-Terawatt Few Cycle Optical Parametric Chirped Pulse Amplifier"

- Ultrafast Phenomena, August 2006 - Pacific Groove CA

  A. Marcinkevicius, **F. Tavella** and F. Krausz, "Development of a Multi-Terawatt Ultrabroadband Optical Parametric Chirped Pulse Amplifier"

- CLEO-QELS, May 2007 - Baltimore MD

  F. Tavella, L. Veisz, A. Marcinkevicius and F. Krausz, "Multiterawatt Three-Cycle Optical Parametric Chirped Pulse Amplifier"

- CLEO Europe/EQEC, July 2007 - München

  F. Tavella, T. Wittmann, K. Schmid, B. Horvath, A. Cavalieri, L.Veisz, A.Marcinkevicius, F.Krausz, "Stronger seed for a multiterawatt few-cycle pulse OPCPA" (post-deadline)

Danksagung

An dieser Stelle möchte ich mich noch bei allen herzlich bedanken, die mich in den letzten Jahren unterstützt, und zum Gelingen dieser Arbeit beigetragen haben:

Ein besonderer Dank geht an meinen Doktorvater Professor Ferenc Krausz für die außerordentlich angenehme Zusammenarbeit und für das stete Interesse im Fortgang meiner Arbeit. Außerdem möchte ich mich noch bei ihm dafür bedanken, daß er mir die nötigen Freiräume bei der Arbeit gelassen hat.

... an den zweiten Gutachter meiner Dissertation Professor Eberhard Riedle für die Geduld beim Lesen und beim Zuhören.

... an Andrius Marcinkeviĉius, meinen damaligen Betreuer, der stets für Aufregung gesorgt hat. Er hat den ersten Stein für die Entwicklung dieses erfolgreichen optischen parametrischen Breitbandpulsverstärkers gelegt. Durch seine wissenschaftliche Erfahrung und durch sein stetes Bereitsein für Diskussion sind Unmengen neuer Ideen entstanden.

Besonderer Dank gebührt den Elektronenmenschen László Veisz, Karl Schmid und Sofia Benavides, die beim letzten Akt, an der Entwicklung des Breitbandpulsverstärkers kräftig Hand angelegt haben. Dies führte zur erfolgreichen ersten Anwendung, der Laserbeschleunigung von ”monoenergetischen” Elektronen. Zudem möchte ich mich bei ihnen für die schlaflosen Nächte während der Experimentierzeit bedanken.

... George Tsakiris, Yutaka Nomura und Rainer Hörlein für die erfreuliche Zusammenarbeit während des Experimentes zur Erzeugung von Laserharmonischen in überdichten Plasmen.

Gesondert möchte ich mich noch einmal bei Karl Schmid, Yutaka Nomura und Lasźlo Veisz für die Entwicklung der Breitbandpulsdiagnostik bedanken, sowie

... bei Nobuhisa Ishii, Takao Fuji, Andrius Baltuŝka für Diskussion und Austausch von Ideen die mich zusätzlich motiviert haben,

... und bei Adrian Cavalieri, der als Labortisch-Nachbar immer laut zu hören war. Bei ihm bedanke ich mich für das Korrekturlesen dieser Arbeit.

Ein Dankeschön allen Mitglieder der Krausz-Gruppe mit denen ich zahllose LAP-meetings unverletzt durchgestanden habe. Besonders möchte ich mich bei den Extremkletterern Thomas Metzger und Jens Rauschenberger für die Stunden in der Wand bedanken.

An dem Techniker-Team Manfred Fischer, Alois Böswald, Harald Haas, Walter Fölsner, Hans-Peter Schönauer, Axel Raufer, Anton Horn, Stefan Grote und Georg Prandl, möchte ich ein herzliches Dankeschön aussprechen.

Ich danke der MPQ-Werkstatt für ihre Hilfe bei allen möglichen Problemen bei Experimentaufbauten und für sonstige raffinierte Konstruktionen.

... der MPQ-Verwaltung, Einkauf und dem Sekretariat, die Manches beschleunigt haben.

... y nia pur ultimi, en bel giulan a vos da ćiasa, sides familia co cumpagns, pur me avëi supurtè düč chisc agn. Spezialmënter a mia só, a chëra che i ti sun jü de plü söi nerf cun mi "blah-blah"-photons, "blah-blah"-eletrons.